UNIVERSITÀ DEGLI STUDI DI PADOVA

Dipartimento di Fisica e Astronomia "Galileo Galilei"

Master Degree in Physics

Final Dissertation

Improvement of SPIDER tomographic diagnostic

Thesis supervisor

Dr. Matteo Agostini

Candidate

Francesco Franco

Thesis co-supervisor

Dr. Margherita Ugoletti

Academic Year 2022/2023

Abstract

The ITER project aims at assessing the feasibility of fusion power generation, with a net 10-fold power gain, using a Tokamak configuration. The fusion fuel (deuterium and tritium) is heated up to 150×10^6 °C, triggering nuclear fusion processes. To reach such high temperatures, additional heating systems will be installed on ITER, like cyclotron heating and Neutral Beam Injection (NBI).

NBI consists in firing a high-energy beam of neutral particles inside the fusion plasma. Energy is transferred via collisions to the fuel for a total of 16.5 MW delivered power. ITER will feature two of such injectors, which work by accelerating a negative hydrogen/deuterium ion beam up to 1 MV, which is then neutralised and delivered to the fusion chamber.

For successful ITER operation, the beam must satisfy strict specifications, for example in terms of ionic current throughput (40 A at 1 MV) - for effective plasma heating - homogeneity (more than 90%) and divergence (less than 7 mrad) - to avoid thermal loads on the beam-line and vessel ports. To reach these requirements, in Padua, at Consorzio RFX, two experiments are hosted: SPIDER and MITICA. SPIDER is the full-size prototype of ITER NBI negative ion source. It is equipped with several diagnostics to study both the beam and plasma source properties. This work focuses on one of such diagnostics, namely the visible tomography of the beam. The second experiment is MITICA, the full size ITER NBI prototype, featuring the same source of SPIDER and with the aims of accelerating the beam up to the energy required by ITER (1 MeV). Tomography is part of the diagnostics tools of MITICA, which is expected to start operation in the next few years.

Visible tomography is a non-invasive diagnostic which uses two-dimensional visible cameras, deployed all around the beam and pointing towards its center from various orientations. They collect the light emitted from the ion beam-background interactions, the beam emissivity, right after the accelerator. The camera signal is an integrated measure of the two-dimensional beam emissivity along different Lines-Of-Signt (LOSs), which can be reconstructed using a suitable inversion algorithm. In the specific case of the SPIDER tomography, the tomographic pixel method is used, where the emissivity is reconstructed inside defined geometrical regions across the beam, allowing a variable degree of spatial resolution. Therefore, the reconstructed emissivity can be used to char-

ABSTRACT

acterise the beam divergence and homogeneity and, using suitable spectroscopic models, allows to estimate the beam current density.

This work aims at improving the current SPIDER tomography by introducing two-dimensional LOSs in the reconstruction algorithm, to better account for the geometry of the diagnostic, and by further developing a model for the beam emission (by introducing new reactions and accounting for the effect of secondary electrons on the beam light), to better interpret the reconstructed emissivity in terms of negative ion current density. The performance of the improved reconstruction algorithm has been tested on experimental data, with 28 out of the 1280 beamlets composing the beam, and with synthetic signals for full-beam simulation. In the latter case, different levels of spatial resolutions have been tested, together with varying amounts of light background and signal noise to simulate non-ideal scenarios.

Testing on experimental data shows good agreement between the previous reconstruction results and the improved 2D-LOS one. Further testing on full-beam simulations shows that the algorithm performance is not affected by the beam features (e.g. beamlet width and uniformity) and the reconstruction error in ideal conditions (no light background and no signal noise) remains around 10% at 5-beamlet resolution or lower for lower resolutions (i.e. 10, 20, 40 or 80-beamlet resolution), showing the possibility for successful application of such upgrades with a sufficient level of detail using two-dimensional LOSs. Light background is shown to impact the most the reconstruction accuracy of the beam, up to 30% in the worst case of 5% background intensity (compared to the nominal beamlet luminosity).

The beam emissivity as a function of the beam energy is assessed, showing a reduction as the beam energy increases. It also demonstrates that the single stripping dominates the beam emission at all energies, increasing as the beam energy does. At SPIDER's nominal acceleration of 100 keV, single stripping processes account for 87.7% of the total emissivity, followed by excitation (5.7%) and secondary electrons (4.1%), also representing a possible cause of light background.

Cameras are calibrated using a calibrated source and a H_α filter in order to obtain an equivalent H_α source whose emissivity is known. Setting the camera in front of the equivalent source allows to link the signal, collected by the completely illuminated pixels, to the emissivity, obtaining a calibration constant which is used to convert the integrated camera counts into radiant power integrals. The reconstructed emissivity allows, using the results from the beam model, to obtain, for the first time, the 2D pattern of the beam current density from its emissivity, which matches the same order of magnitude of the direct electrical measurements of the STRIKE calorimeter and the Beam Current Monitor.

Contents

1. Introduction

1.1. The role of fusion

Climate change and its recognition, now by the majority of media and the public, are pushing the development of new power production technologies with higher environmental compatibility and, most importantly, with the aim at drastically reducing the emission of CO_2 gas in the atmosphere. A future based on clean electricity will reduce greenhouse gas emissions not only from the power production sector, but also from tertiary sectors such as transportation. At the current time, transitional sources of energy are being adopted to reduce the use of fossil fuels, mainly photovoltaic panels, wind turbines, hydroelectric, geothermal, biogas and nuclear fission plants. Solar panels and wind turbines are renewable sources heavily dependent on weather conditions, light cycles, thus they cannot provide a reliable base load to the grid. Hydroelectric damns can be highly impactful on the geography of their construction site, requiring huge basins for water storage and they are dependent on water availability (a similar issued shared with geothermal power generation, which requires hot spots for steam extraction), either being a river or a large bay (in the case of tidal power production). Biogas sources are not completely clean in terms of CO_2 emissions and nuclear fission power plants, although now very safe in terms of radiation leaks and extreme events, are not renewable, produce long-lived radioactive waste and find some opposition from public adoption. The search for a definitive, clean electrical power source is still ongoing, also in the form of nuclear fusion.

Nuclear fusion exploits the high-energy bonds of nucleons of light atoms [1–3], such as hydrogen isotopes. Two atoms of deuterium and tritium are brought in close proximity by imparting them a huge amount of thermal (or kinetic) energy, to the point of overcoming their Coulombian repulsion and fusing them into helium, releasing a neutron and 17.6 MeV of kinetic energy, carried by the two products:

$$^2\text{D} + {}^3\text{T} \; \rightarrow \; {}^4\text{He} + n$$
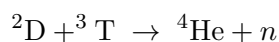
In particular, the neutron carries 14.1 MeV, while the helium nucleus the remaining 3.5 MeV [4]. The energy scale of the reaction is roughly 1 million times higher than an equivalent chemical reaction between carbon and oxygen during combustion (i.e. used in fossil fuel plants). The huge energy storage represented by nuclear bonds is what

3

made nuclear fission power generation a viable option as a stable and efficient energy source. Differently from nuclear fission, however, nuclear fusion does not produce long-lived radioactive waste and does not require sophisticated means of fuel extraction, like the uranium used for fission.

The reason for the belated development and adoption of fusion power technology is due to technical impairments (for instance, required materials and powerful computational tools for magnetohydrodynamics studies, now available) and, most importantly, to the extreme conditions necessary for fusion reactions to occur and to self-sustain. Differently from fission, which exploits the natural instability of ^{235}U, the fusion of two light nuclei requires high temperatures and pressures. These processes naturally occur at the center of the Sun, where the extreme pressure (10^{11} atm) allows the $p-p$ chain to burn hydrogen at 15 million °C [5].

On Earth, fusion power is achieved in a variety of means and this work focuses on the magnetic confinement approach, using the "tokamak" geometry. A tokamak - from the Russian acronym "toroidal chamber with magnetic coils", is a device which allows to confine a hot ionised gas using magnetic fields in a donut-shaped geometry. The working principle for power generation of such machines is the injection, heating and ionisation of a small amount of hydrogen fuel. Isolated from the chamber walls using the magnetic coils, the hot plasma undergoes fusion reactions at 150 million °C, which in turn keep the fuel hot and allow continuous operation by replenishing hydrogen and removing helium from the chamber. Energy is carried by free neutrons, which are not bound by the magnetic confinement and impact onto the vessel walls, where coolant is circulated and used for steam production. The extreme temperatures required, the low density of the gas and the delicate equilibrium at which these machines operate, make fusion a very safe technology, as any accident will result in an abrupt plasma shutdown and no extremely dangerous nuclear waste. A tokamak fusion power plant produces renewable energy, as the fuel can be extracted from sea water and small quantities of it are necessary. I must be stated that, as consequence of the production of high energy neutrons, the plasma facing and near-vessel components will produce some kind of nuclear waste [6, 7]. However, these active materials are relatively short-lived and pose a much less complex management issue compared to fission waste, potentially being available for recycling and re-use. Fusion technology is now experiencing huge developments in terms of confinement time, power production and experimental progress, thanks to the joint efforts of various experiments all around the world. If successful, the adoption of fusion as the final, clean and safe energy source will drive society in the following decades. Together with an immediate intervention to cut emission with transitional power production technologies, nuclear fusion will help a sustainable coexistence between human development and the preservation of the environment.

This work focuses on one of the many plasma heating systems necessary to reach fusion temperatures, the neutral beam injection and, in particular, its application in the biggest experimental fusion device, ITER, one of the most advanced fusion projects yet and a fundamental milestone in the path towards successful fusion control.
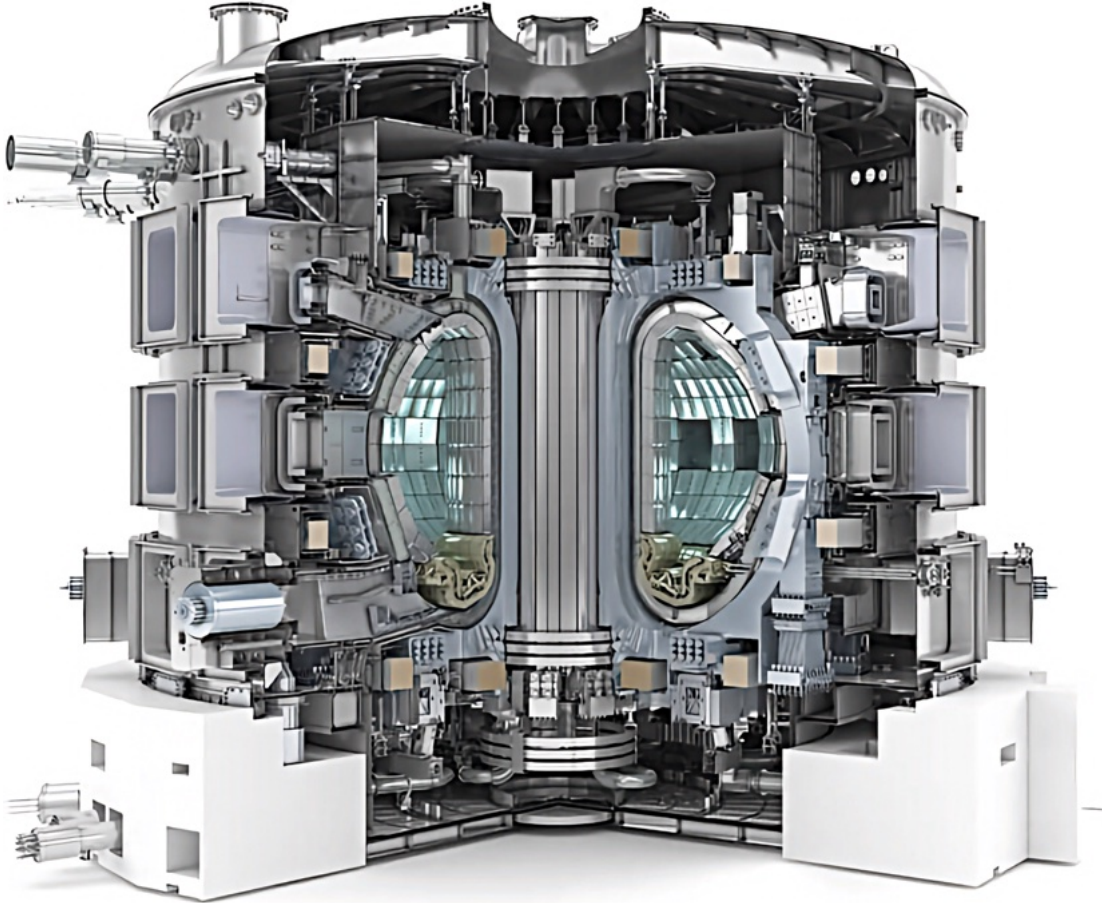
1.2. The ITER project

Figure 1.1: A render of the ITER cryostat and systems therein. The inner toroidal chamber can be seen, covered with blanket tiles. At the bottom of the vessel, the divertor cassettes can be seen. Around the camber, superconducting magnetic coils are shown, cooled with cryogenic helium. The central pillar is the main solenoid, providing the necessary electric fields to trigger ionisation and to induce plasma current. The cryostat, the outer shell, features many ports for material handling, diagnostics, cyclotronic heating systems and neutral beam heating systems. Credits: Ref.[8].

ITER, from Latin "The Way", is an experimental fusion plant using a tokamak reactor, located in Cadarache, France [9]. This project is an international collaboration between the EU, USA, Japan, China, South Korea, India and Russia, tasked with proving the feasibility of fusion power production. In particular, ITER aims at obtaining a power gain of $Q = 10$ [10], which is the ratio between the power required for plasma heating and control and the power extracted from fusion, with a nominal power output of 500 MW. ITER represents, at the moment, the largest tokamak machine under construction, with a 11-meter-tall fusion chamber, 1400 m^3 of internal volume and 16 T magnetic fields, and it aims at assessing key challenges for future industrial fusion power plants [11]:

- burning plasma: achieve conditions in which fusion temperatures are maintained by the reactions themselves, allowing to sustain fuel burning without the help of external heating systems for a prolonged period of time (1 h);

- $Q = 10$: produce 500 MW power output from fusion reactions with an initial 50 MW power usage for plasma startup and containment. ITER is not tasked to produce electrical power for the grid, but will assess the conditions which will allow future full-fledged power plants to do so;

- tritium breeding: using tritium as fuel poses some stocking and sourcing challenges. Indeed, tritium is unstable with a half-life of 12.3 yrs. This makes stocking unfeasible and it must be produced on site. Lithium-based blankets will be used to assess the possibility of tritium breeding from neutron enrichment of lithium atoms, allowing to extract, purify and re-inject the hydrogen isotope as fuel in the fusion chamber;

- size scaling: as size is a relevant factor [12] for future successful fusion power plant operation, ITER will help bridge the size gap between fusion experiments and industrial devices, assessing how different fusion technologies interact and perform as the scale of tokamak machines increases;

- safety: ITER will demonstrate the safety and environmental compatibility of plasma operations and future power plants.

ITER design features 8 main components, visible in Fig.1.1:

- a toroidal vacuum vessel, characteristic of tokamak machines, of triangularised and elongated section (11.4 m high) with a external diameter of 19.4 m;

- the blanket, composed of 440 plasma-facing modules in beryllium and high-strenght copper and stainless steel, covering the inner surface of the vacuum vessel and tasked with neutron and heat absorption and tritium breeding (in some sections);

- the divertor, the bottom region of the chamber where fusion plasma is cooled and exhausted and the where the highest heat loads are expected;

- the central solenoid, a powerful coil for electric field and plasma current generation inside the chamber. The central solenoid will kickstart the fuel ionisation process by electrical breakdown of the gas;

- superconducting toroidal magnets, encircling the section of the chamber, tasked with the production of the toroidal magnetic fields for plasma confinement;

- superconducting poloidal magnets, responsible for the production of the poloidal field for plasma control and confinement;

- heating systems, consisting in microwave injection and neutral beam injection for plasma heating to fusion temperatures;

- the cryostat, the outer vessel containing the vacuum vessel, the magnets and keep-

ing them at cryogenic temperatures by circulating liquid helium. It features ports for material handling, diagnostics and heating systems.

1.3. Heating systems

ITER features three main heating systems, tasked with bringing the fuel to 150 million °C. Operations begin with a cold, low-density fuel gas introduced in the toroidal chamber. Intense electric fields, provided by the ITER's central solenoid, cause electrical breakdown inside the gas, exploiting the residual ionisation naturally present. Electrons are stripped from their atoms and accelerated, causing a cascade effect inside the fuel - by impacting and ionising other atoms - and generating a plasma. The collective displacement of charge from the neutral fuel generates and electric current running inside the plasma, providing heating via resistance. This first method is called Ohmic heating, but its effectiveness decreases with growing plasma temperature, as the ionisation increases leading to greater conductivity. Overall, the Ohmic heating provides 10% of the total energy required to reach the fusion target temperature.

External heating systems provide the remaining energy in the form of microwaves and high-energy neutral particles. Ionic Cyclotron Resonance Heating (ICRH) delivers 10 MW of power, in the form of microwaves between 40 and 55 MHz, via a plasma-facing antenna [13]. The frequency is specifically tuned at the ions' cyclotron frequency inside the plasma for optimal power transfer to the heavy atomic species present inside the vessel, i.e. deuterium and tritium nuclei. A similar approach is adopted for the Electron Cyclotron Resonance Heating (ECRH), producing 1 MW of microwave power at 170 GHz, aiming at accelerating the electrons of the plasma [14]. The last heating method is the Neutral Beam Injection (NBI), employed on ITER with two 16-MW injectors working at 1 MeV of acceleration energy [15]. The neutral beam injection works by generating a hydrogen/deuterium plasma from which negative H^-/D^- ions are extracted and accelerated in a beam. Ions then enter a neutralisation chamber, where neutral gas strips one electron from the beam particles, resulting in a neutral beam. The neutral particles are injected inside the fusion plasma, where they thermalise transferring energy to the fuel. The injection of neutral particles is also useful for sustaining the plasma current circulating in the chamber. The reason for the use of negative ions is clearly shown in Fig.1.2 [16]: at 1 MeV, the neutralisation efficiency of deuterium negative ions is around 60%, while it dramatically drops for positive ionic species. This is due to the natural instability of negative hydrogen ions, which, on the other hand, brings technical challenges in their handling along the beam-line. Neutral particles are essential for a kinetic heating device in a tokamak: the powerful magnetic fields would deflect any charged particle directed towards the plasma.

ITER NBI is being developed in Padova at the RFX Consortium (Ref.[17, 18]) with two experiments: MITICA, the full-scale prototype of ITER's NBI, and SPIDER, the experimental negative ion source.
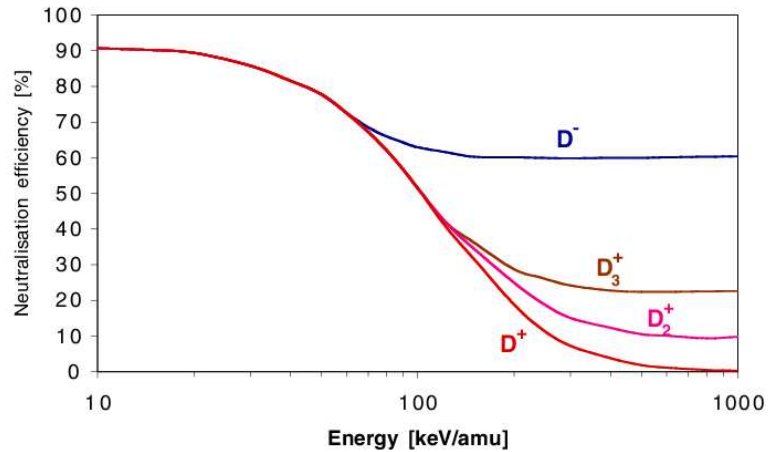
Figure 1.2: Neutralisation efficiency as a function of energy. D^- ions represent the best performing candidate for neutralisation at ITER NBI energy of 1 MeV, with a neutralisation efficiency of 60%. By comparison, positive deuterium ions are practically non-interacting with the neutral gas at this energy, rendering them non viable for such application.
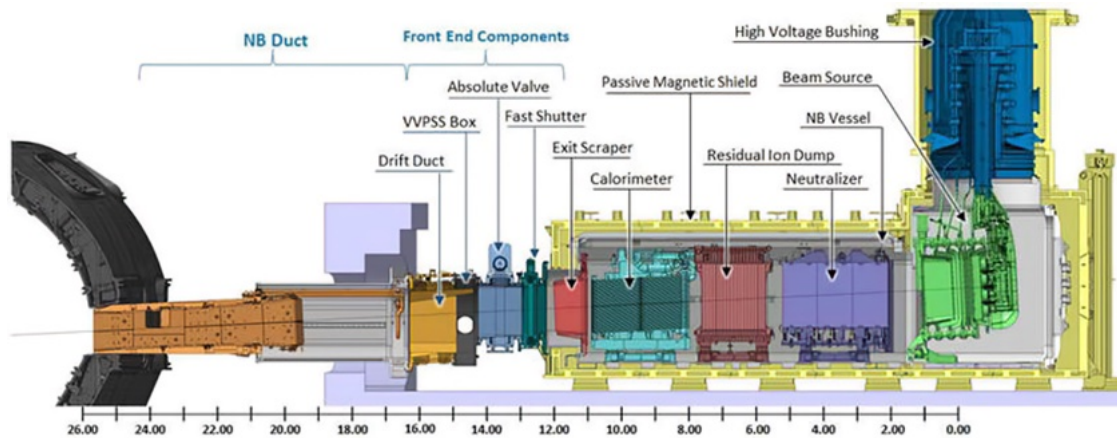
1.4. MITICA and SPIDER experiments

Figure 1.3: A render of MITICA's structure. In green, the source section: on the right part, the 4 2-driver segments can be seen, followed by the 5 acceleration grids. The neutraliser and other subsystems follow, leading to the injection duct inside the fusion chamber (on the far left).

MITICA is the full-scale prototype of ITER NBI, designed to accelerate 40 A of D^- at 1 MeV, for a total of 16 MW of power delivery to the fusion plasma [15, 19]. The structure of the NBI is articulated in a series of stages along the beam line (shown in Fig.1.3), starting with the negative ion source, currently under study in the SPIDER experiment. Next in the beam-line, MITICA features the 1-MV accelerator, the neutraliser (which converts the accelerated negative ions into neutral particles), the residual ion dump (for residual ions removal from the beam) and the calorimeter (for commissioning of the NBI

8

and to measure the total energy of the beam). SPIDER is the experimental prototype of ITER NBI negative ion source, developed to assess and characterise the beam generation and acceleration physics at reduced energy (100 keV).

The SPIDER source, shown in Fig.1.4, is composed of 4 pairs (or segments) of induction drivers arranged vertically, where hydrogen or deuterium gas is injected. Powerful RadioFrequency (RF) induction coils (4×200 kW) [20], located outside each driver, ionise the gas producing a plasma, which is allowed to expand outside the drivers into the common expansion region. Here, a perforated grid (Plasma Grid - PG) extracts the negative ions in beamlets, which are then accelerated between two following grids (the Extraction Grid - EG - and the Grounded Grid - GG) at a nominal energy of 100 keV [21]. Caesium evaporation is available, via the presence of three caesium evaporation ovens, in order to enhance the negative ions production on the PG [22]. The source-facing side of the plasma grid also features a bias plate, a copper plate divided into 5 elements, whose potential is biased with respect to the PG and the RF source in order to minimise the electron co-extraction. To this purpose, also an electric current is circulated along the Plasma Grid to produce a magnetic field, called Filter Field [23] with the aim of further reducing the fraction of co-extracted electrons, which would
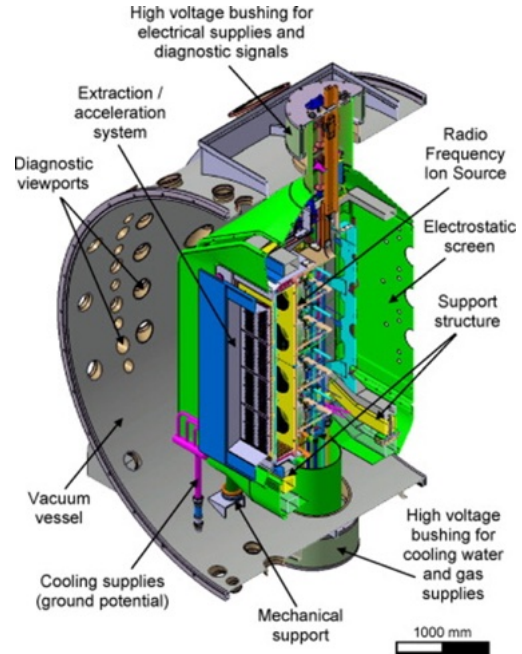

Figure 1.4: A view of the SPIDER source. In yellow, the 4 RF segments and their 8 drivers (in the figure, 4 are visible) leading to the expansion region. The blue elements highlights the acceleration section, showing the grid positioning after the source.

cause damage to the acceleration grids and worsen beamlet optics due to the increased Coulombian repulsion. Moreover, the Filter Field lowers the co-extracted electrons' energy in the extraction region, improving the H$^-$ ions lifetime, as the probability of removal of the negative charge of the H$^-$ ions from the co-extracted electrons is reduced [24].

SPIDER grids feature 1280 apertures, arranged in 16 groups of 5×16 beamlets each, as shown in Fig.1.5, with a total grid area of 1×2 m, a beam cross-section of 1.5×0.6 m and total aperture area of 0.2 m^2.

In view of the future implementation of SPIDER knowledge in MITICA, which will feature 1 MV acceleration with five grids of the same aforementioned kind, SPIDER and its beam will need to satisfy strict performance requirements [15, 17]: a beam pulse duration of 3600 s, 40 to 70 A of H$^-$/D$^-$ at 100 keV acceleration, 0.3 Pa source pressure and, regarding the main focus of this work, 90% beam homogeneity and 7 mrad of beamlet divergence, δ. These two parameters are particularly relevant for successful

beam operation in MITICA and ITER in order to achieve the required power delivery to the fusion plasma and avoid damaging thermal loads on the acceleration grids and beam line components.

Differently from MITICA, SPIDER has been designed to host many diagnostics for source and beam characterisation, including source spectroscopy [25] and Langmuir probes [26] (in the source), Beam Emission Spectroscopy (BES) [27], the STRIKE calorimeter [28] and camera tomography (on the beam-line). At the current time, the SPIDER grid is operating at a reduced amount of open beamlets - 28, due to vacuum pumping issues [29], as shown in Fig.1.6 from Ref.[30] - and full-beam operation is expected to begin in the upcoming years, with increased vacuum capabilities and new RF power systems. However, the current beam features do not yet meet the ITER NBI requirements [31, 32], obtaining a 80% homogeneity and 12 mrad minimum divergence during the first experimental campaign with caesium [33, 34].

Enhancements on the hardware (e.g. vacuum pumping and RF power feed) are sided with improvements on the diagnostics. In particular, this work focuses on the improvement of the beam tomography. In fact, up to now, this diagnostic has been used for the measurement of the divergence of single beamlets and for the characterisation of the 2D emission uniformity. The improvements here carried out, both on the algorithm algorithm side and on the hardware, have the aim of measuring also the 2D map of the current density of the beam. In fact, when operating at full power and pulse length, tomography will be one of the few diagnostic capable of doing such characterisation. In the following chapters, first the tomographic diagnostic of SPIDER is introduced in its current state-of-the art. Then, improvements on the tomographic algorithm are discussed and tested, consisting in a new and more realistic geometrical interpretation of the data produced by the cameras. Lastly, an atomic model of the beam is developed and paired with the camera calibration to obtain a first estimate of the beam current using visible tomography.
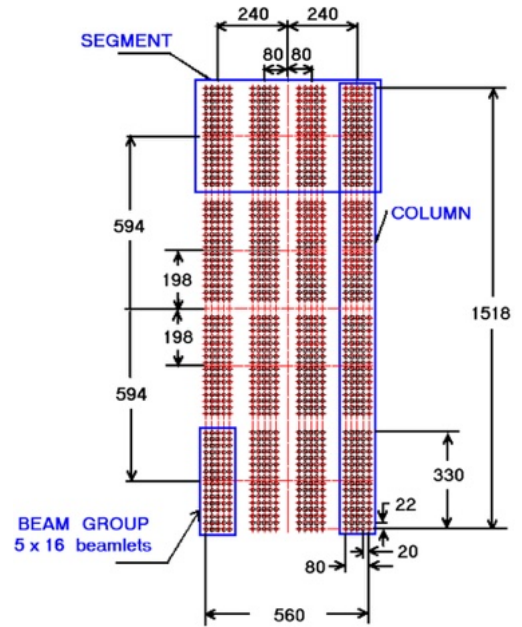

Figure 1.5: A scheme of the SPIDER grids' aperture pattern. 1280 circular openings are arranged in 16 groups of 80 apertures each, 5 in width and 16 in height.
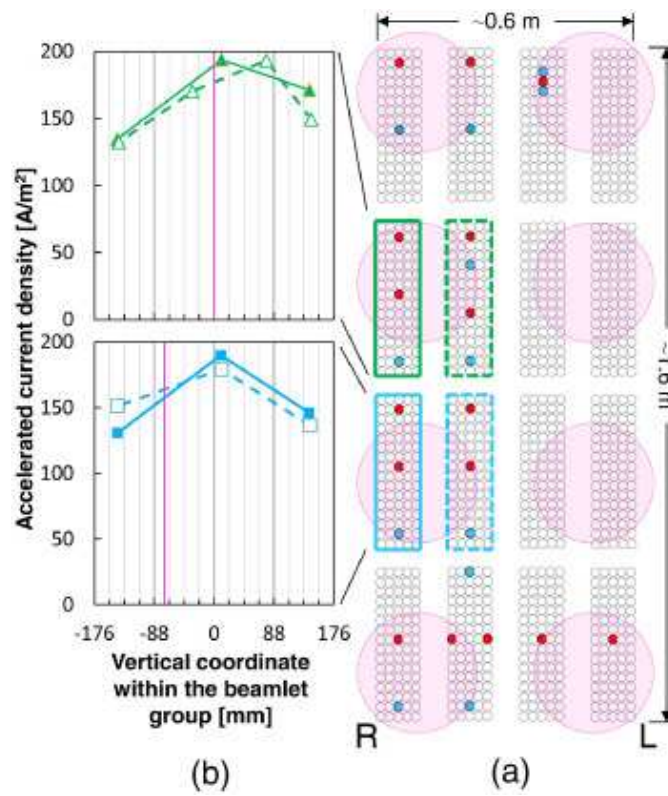
Figure 1.6: On the right, scheme of open apertures' location in the 28-beamlet regime. On the left, the current density measured by the STRIKE calorimeter for each beamlet inside the designated beamlet groups.

2. Tomography

As the main focus of the work, in this chapter the tomographic diagnostic is introduced, first in its general working principle and scope, then its application and use on SPIDER is presented. Tomography (from Greek τομοζ, meaning "part", and γραφω, equivalent to "describing") is a imaging technique, widely employed in medicine, but also in archeology [35] and physics, which allows reconstructing the two-dimensional composition (or, density, or absorption/emission pattern) of an object in a non-destructive way, starting from a set of one-dimensional experimental data. In tomography, the radiation emission - or absorption - proprieties of materials are exploited to obtain a series of images from different points of view, i.e. the emission - or absorption - line integral measurements of the object to be reconstructed. Data are integrated via appropriate algorithms in order to obtain a cross-sectional reconstruction of the object, including the different material proprieties which make up the object slice. Indeed, in the case of medical devices as Computed Tomography (CT scanners, see Ref.[36]), X-rays are shined through the patient onto a detector while the whole apparatus rotates around the subject. As radiation crosses the body, different tissues with different compositions attenuate the radiation to various degrees, resulting in darker or lighter areas on the images. Combining the geometrical information (i.e.: X-ray source-detector position with respect to the patient) with the images obtained by the scanner (absorption maps of the X-rays from different points of view), the internal composition of the body can be obtained along its cross-section. Usually, CT scanners move the body along its axis in order to reconstruct the cross-sectional composition not only of one single slice, but of multiple slices so that a full 3D reconstruction of the patient section of interest can be diagnosed.

Tomography is based on the fundamental notion of Radon transform, from Johann Radon, its proponent [37]. Considering a function $f(x, y)$, which may be a 2D map of absorption or emission coefficients of the object, its Radon transform is defined as

$$\mathcal{R}_\phi(p)[f] = \int f(x, y)\, \delta(x \cos \phi + y \sin \phi - p)\, \mathrm{d}x\, \mathrm{d}y$$

where variables are defined in Fig.2.1. The picture on the right, the full Radon transform at each angle, is called sinogram, as each off-center value of f with respect to the origin traces a sinusoidal curve in the transform.
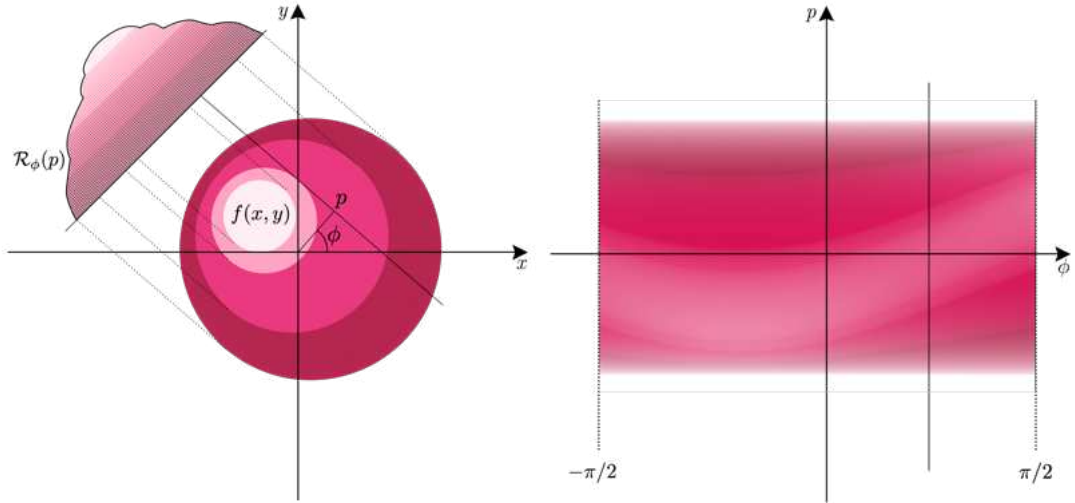
Figure 2.1: On the left, the construction principle of the Radon transform at a fixed angle ϕ. On the right, the resulting full transform, a sinogram, with the vertical line indicating the slice depicted on the left.

The Central Slice Theorem allows to link the the two-dimensional Fourier transform of $f(x,y)$ - $\mathcal{F}(k_x, k_y)[f]$ - to the one-dimensional Fourier transform of the Radon transform

$$\mathcal{F}(k,\phi)\left[\mathcal{R}_\phi(p)\right] = \mathcal{F}(k\cos\phi, k\sin\phi)$$

This means that the value of the two-dimensional Fourier transform of f along a line of inclination angle ϕ is the one-dimensional Fourier transform of $\mathcal{R}_\phi(p)[f]$. If the number of projections $\mathcal{F}(k,\phi)\left[\mathcal{R}_\phi(p)\right]$ is large enough, the two-dimensional Fourier transform can be reconstructed, as enough of the (k_x, k_y) space is covered. This allows a class of tomographic reconstruction algorithms to obtain $f(x,y)$ from the Radon transform. However, their application depends on the number and distribution of the Lines-Of-Sight (LOSs) along which the Radon transform is obtained. In the medical field is often used the back-projection algorithm [38], together with image filtering. This solution works with a large amount of data available (e.g.: in Computed Tomography scanners or Positron Emission Tomography with big detectors with many available LOSs [39]). However, in the next section will be shown that the hardware restrictions imposed by the structural requirements of SPIDER allow few cameras to be installed, with a consequent reduced number of camera Fields-Of-View (FOVs). Since the number of LOSs is limited and they are non-uniformly distributed around the beam, the algebraic reconstruction algorithms are proved to give the best performance [40].

Tomography finds application, in the context of negative ion beams, for the reconstruction of the beam current density. The unique design of SPIDER and MITICA multi-beamlet beams requires the characterisation of each beamlet's current in order to assess the global beam homogeneity and divergence. Moreover, the intrinsic non-invasive

nature of tomography allows to estimate the beam current density without perturbing it. In particular, the reduced number of diagnostics equipping MITICA - compared to SPIDER - will put further relevance on the tomographic diagnostic for beam characterisation in terms of homogeneity, divergence and current throughput. MITICA will feature a completely new set of one-dimensional cameras (equipped with a single-pixel-wide sensor) which will be able to operate in the neutron-rich environment of ITER. The intermediate step of SPIDER, adopting commercial visible cameras, allows to obtain important insights for visibile tomography before future upgrade on ITER NBI.

2.1. Visible tomography in SPIDER
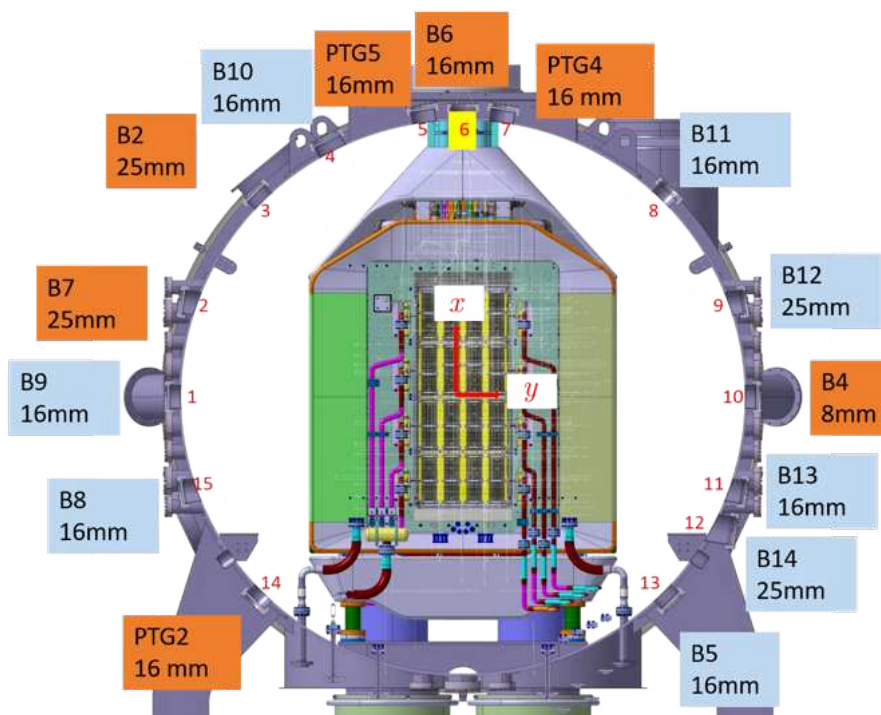
Figure 2.2: A schematic front view of camera location in SPIDER.

In SPIDER, tomography is realised with a set of 15 visible cameras located around the beam vessel on suitable viewing ports, assigned as shown in Tab.2.1 and Fig.2.2. Cameras are equipped with three focal lengths f of 8, 16 and 25 mm lenses, with 1.5, 0.75 and 0.48 mm pixel^{-1} resolutions respectively (at the center of the beam). In particular, Basler (B) cameras' model is acA1920-40 gm, featuring a Sony IMX249 CMOS sensor, composed of 1920×1200 square pixels (5.86 μm side), with 12-bit resolution and maximum acquisition rate 45 frames per second. PointGrey (PTG) cameras' model is BFS-PGE-27S5M-C, which uses Sony IMX429 CMOS sensor, composed of 1936×1460 square pixels (4.5 μm side), with 16-bit resolution and maximum acquisition rate 43 frames per second [41–43]. Each camera points towards the beam axis and their orientation has been optimised in

15

Port n.	Label	Model	Obj. lens
01	B9	Basler	16 mm
02	B7	Basler	25 mm
03	B2	Basler	25 mm
04	B10	Basler	16 mm
05	PTG5	PointGrey	16 mm
06	B6	Basler	16 mm
07	PTG14	PointGrey	16 mm
08	B11	Basler	16 mm
08	B12	Basler	25 mm
10	B4	Basler	8 mm
11	B13	Basler	16 mm
12	B14	Basler	25 mm
13	B5	Basler	16 mm
14	PTG2	PointGrey	16 mm
15	B8	Basler	16 mm

Table 2.1: List of all cameras use for tomography, their assigned viewport and focal lens information.

order to avoid redundant information. All cameras observe the beam light at $z = 0.35$ m after the GG and their FOV direction and amplitude are known. As each camera sensor is made of many CMOS pixels, each of them defines a Line-Of-Sight (LOS) inside the camera's FOV. For better contrast and minimise stray light, the FOV section of the vessel is lined with an opaque blackened strip of aluminum (Metal Velvet coated foil by Acktar).

As the beam travels onwards along the $\hat{z}$ axis from the GG, it interacts with a low-pressure H_2 background at roughly 0.03 Pa (depending on source pressure). Different reactions produce various ionic species, which interact with the negative ions, among themselves and with the background. The main contribution to the visible light measured by the camera is due to the excited atomic hydrogen H^{0*}, which decays mostly from the level $n = 3$ to $n = 2$. The result is a light emission (at the specific 656.46 nm wavelength, called the H_α line of the Balmer series) from each beamlet, visible in Fig.2.3, and the surrounding region, which is expected to decay with the distance from the beamlets axis. In Fig.2.3 it is possible to see the light traces of the beamlets exiting the GG impacting, on the left of the picture, on the STRIKE calorimeter. The collection of the beamlets exiting the GG represents the SPIDER beam. Here, only the 28 beamlets are present, but the future ITER NBI will feature a much higher number of beamlets (and light traces). The radiant power emission rate of the beamlets is called beam emissivity ϵ and is identified as a cross-sectional emission map which can be reconstructed using tomography. Therefore, the signal used in the reconstruction is not an attenuation measurement of a given light source through a volume, but the emission rate within the volume itself. Although the underlying physics is different, formally speaking, the two descriptions are equivalent. The signal I_j obtained by each camera sensor is an integral
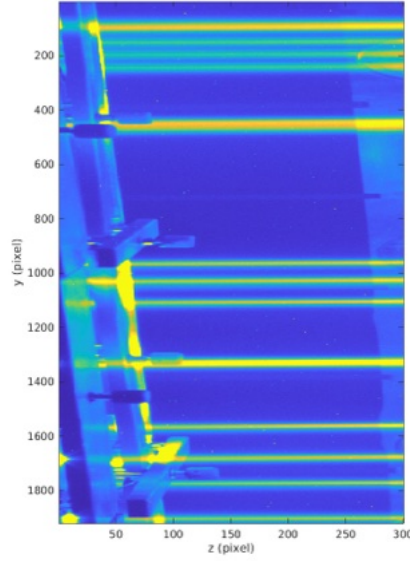
Figure 2.3: Image captured by cameras inside the beam vessel during operation (in false colours). The light traces of some of the 28 beamlets of the beam can be seen.

in space along the region designed by the LOSs:

$$I_j = \int_{\text{LOS}_j} \epsilon(x,y) \, \mathrm{d}x \, \mathrm{d}y \tag{2.1}$$

The task of reconstructing the 2D structure, or properties, of an object starting from one-dimensional line measurements (i.e. the inversion of Eq.2.1, obtaining $\epsilon(x,y)$ from the experimental line integrals I_j) is an ill-posed problem, which shall be referred to as the reconstruction problem. Indeed, an exact solution for the reconstructed pattern is virtually non-obtainable and the choice of the best inversion algorithm depends on the a-priori knowledge of the system, the underdetermination or overdetermination of the mathematical system or the presence of noise. It must be noted that although all camera pixels, or image pixels, can be used for the reconstruction along beam propagation direction, for the purpose of SPIDER diagnostic only the average value of the beam emission over the 5 pixel centred on the blackened aluminum foil is used as signal for the tomographic reconstruction, in order to maximise the signal-to-noise ratio. For the sake of brevity, from now on, any reference to camera pixels and sensors will be referred to such pixel strip. Since the beam is stationary, once the space charge compensation occurs, the variation of beam emissivity along z in the section observed by the cameras - inside the pixel strip - can be assumed negligible and the thickness of LOSs along z is considered non-influential for the results. As Fig.2.4 shows, in the three-camera example the light from the three beamlets is integrated along the LOSs of each camera's FOV, resulting in different images. Once the pixel strip is selected, the signals are given

17

as input to the reconstruction algorithm, which reconstructs the 2D emissivity map $\epsilon(x, y)$ of the overall 3-beamlet beam inverting Eq.2.1. As it is shown in the following section, the limited amount of viewports sets strong limits to the overall reconstruction capabilities in terms of resolution. This is the challenge posed by the reconstruction problem in SPIDER: obtaining $\epsilon(x, y)$ from the collection of the integrals, or signal, I_j taking into account the availability of viewing ports, geometry and number of the LOSs and features of the SPIDER beam, presence of noise and light background in the data. To ensure signal consistency among all cameras, relative calibration has been carried out and it is detailed in Ref.[41].
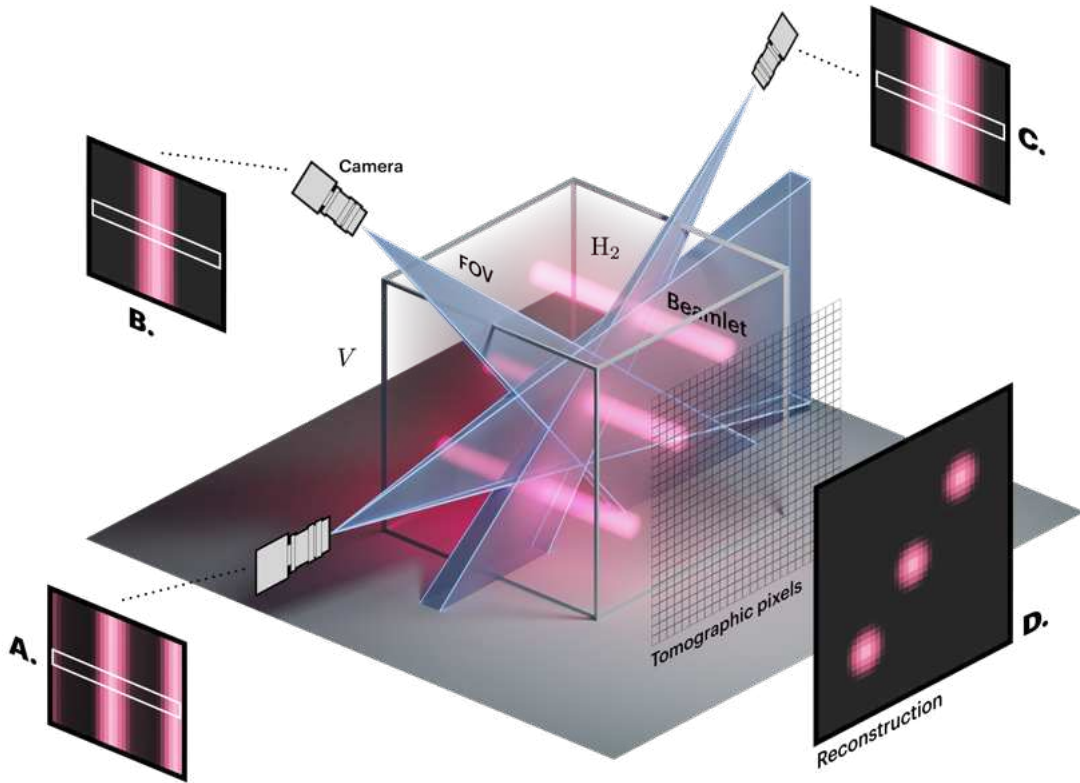
Figure 2.4: In principle, tomography in SPIDER works by observing the beam (here made of 3 beamlets) from different points of view, producing different images of each camera's FOV (**A.**, **B.** and **C.**). The tomographic algorithm combines images (in the case of SPIDER, a pixel strip of each image - shown here in white) to obtain a 2D reconstruction of the beam, shown in **D.**, assigning an emissivity value to each tomographic pixel, defined in Sec.2.2.

2.2. The tomographic inversion algorithm: Simultaneous Algebraic Reconstruction Technique

The structural constraints imposed by SPIDER (and, in the future, MITICA) see the employment of the algebraic reconstruction method. The adopted solution for the spe-

cific case of SPIDER is the Simultaneous Algebraic Reconstruction Technique (SART) [44], employing the tomographic pixel method. This method is based on dividing the target image in a set of finite elements, pixels, in which the emissivity is defined positive and it is equal to an unknown quantity ϵ_i. A collection of such tomographic pixels shall be called pattern.
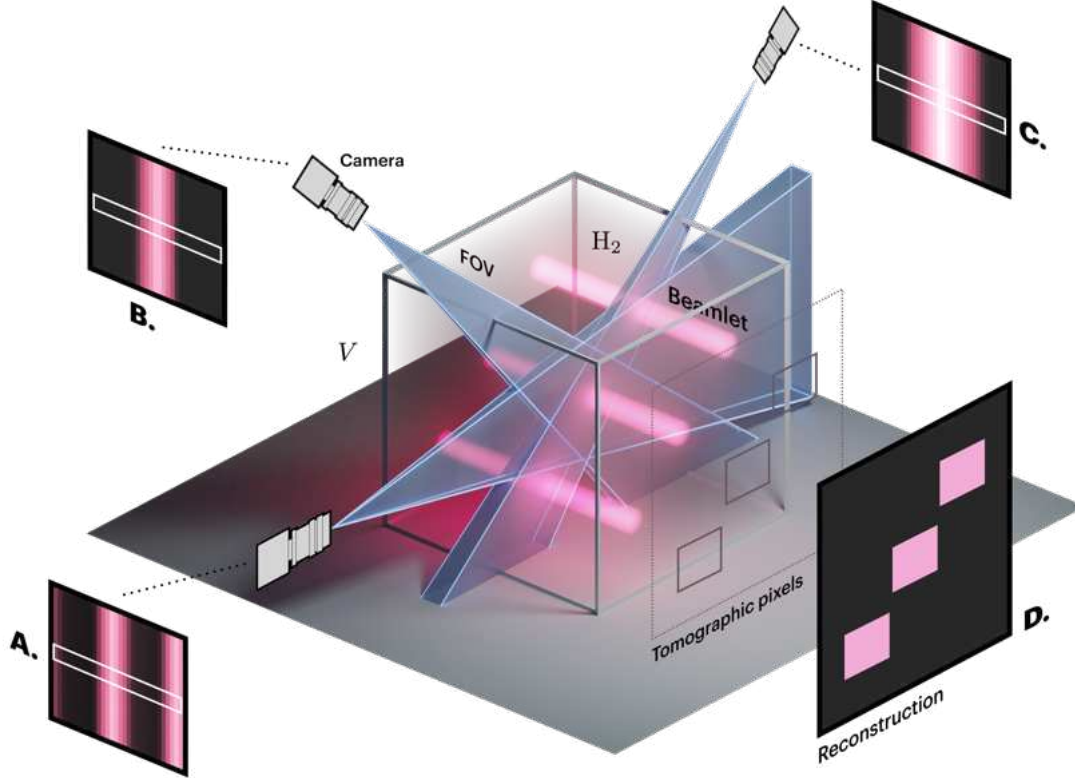

Figure 2.5: The same example presented in Fig.2.4, but here the tomographic pixels are assigned to one beamlet to reconstruct its overall emissivity.

For each camera, a fan of one-dimensional LOSs is defined, one assigned to each camera sensor pixel (from now referred as "camera pixel"). The jth LOS collects a line integral of the beam emissivity along its length, namely a light integral or signal, denoted with the symbol I_j. In the tomographic pixel approach, the amount of light collected along the LOS is proportional to the emissivity of each tomographic pixel, but also to the magnitude of the intersection of the LOS with the pixel. Furthermore, one LOS can intersect many tomographic pixels, only one or none, depending on the specific pattern and the parameters of the LOS. Starting from these considerations, one shall express the jth signal I_j as

$$I_j = \sum_i a_{ji} \, \epsilon_i \tag{2.2}$$

where a_{ij} represents the contribution of the emissivity of the ith tomographic pixels ϵ_i

19

weighted by the value of the intersection between the jth LOS and the ith tomographic pixel. One-dimensional LOSs are employed in the first version of the reconstruction algorithm used on SPIDER. The collection of these elements a_{ij} defines the **a** matrix

The solution of mathematically ill-posed tomographic problem is the emissivity of each pixel ϵ_i obtained by inverting Eq.2.2 using the SART.
SART is an iterative algorithm: at each step k the reconstructed emissivity is computed starting from the previous iteration, and consists in the following recursive expression:

$$\epsilon_i^{(k+1)} = \epsilon_i^{(k)} + \frac{\sum_j \left[a_{ij} \frac{\vec{I}_j - \vec{a}_j \cdot \epsilon^{(k)}}{\sum_i a_{ij}} \right]}{\sum_j a_{ij}} \tag{2.3}$$

where $\epsilon_i^{(k)}$ is the reconstructed emissivity for the ith tomographic pixel at the kth iteration and $\vec{a}_j$ is the jth column of the **a** matrix. The last term of the recursive relation Eq.2.3 is a correction term (averaged over all LOSs $\sum_j a_{ij}$) [44].

Since the number of LOSs is fixed and their orientation is limited by the geometrical constraints of SPIDER vessel, the only variable is the design of the tomographic pixel pattern, i.e. location, number, size and shape of the tomographic pixels. Increasing the number of tomographic pixels, however, not only improves the resolution of the tomographic reconstruction, but it also increases the number of unknowns, resulting in a larger number of artefacts. Moreover, it affects the computational time to reconstruct the beam image. For the purpose of this work and the full-beam tomography, tomographic pixels must be sized and placed in such a way that enough beamlet area is included, in order to be sure not to lose any part of the beam emissivity, and so of the beam current. This naturally leads to the definition of beamlet resolution of the reconstruction, which is quantified with the number of beamlets included in the tomographic pixels, ranging from 80 (one beamlet group) to 1 (one single beamlet), as shown in Fig.2.5, as higher resolutions are not possible due to the lack of data and the lengthening of the reconstruction process in time. Rectangular pixels were chosen, as they are simple to tile and code and represent and effective solution for the tomographic pixel method. As will be shown in the following Chapter 3, tomographic pixels in the inner regions of each beamlet group - if the pixel does not cover the whole group altogether - are designed in close contact to cover the entirety of each beamlet. For example, in the case of 1-beamlet resolution, inner tomographic pixels will be sized as the aperture spacing of 20×22 mm and centred on the beamlets nominal position. For beamlets on the edge of each group, at 1-beamlet resolution, the pixel is extended outwards twice the width or height of inner pixels, thus producing 3 possible combinations: 20×44 mm, 40×22 mm and 40×22 mm. A similar approach is taken for reduced resolutions. In the case of the 28-beamlet experimental configuration adopted for SPIDER so far, all pixels are centred on the beamlet nominal configuration with a size $3\sigma \times 3\sigma$, where σ is the average width of the beamlets (estimated as shown in Ref.[32]), which depends on beam optics.

3. Improvements on the reconstruction algorithm

In this chapter, improvements to the tomographic inversion algorithm are presented. The focus is on the modification of the **a** matrix, which plays a key role in determining the resolution and the goodness-of-fit of the reconstruction, together with the number of pixel (see Eq.2.2). In the previous version of the algorithm, the tomographic reconstructions of the emissivity of SPIDER beam are performed using one-dimensional LOSs [31] defined by two parameters: m, the angular coefficient, and q, the intercept with the $\hat{y}$ axis. The goal is to extend the geometry of the **a** matrix by defining and implementing two-dimensional LOSs in the computation of a_{ij}, which is expected to improve the reliability of the reconstruction algorithm and represent a more realistic interpretation of the LOSs of the cameras. In particular, some optimisation steps are presented in order to reliably and efficiently compute the matrix.

In the following section, the approach for the development of the new algorithm for the computation of the **a** matrix - using the two-dimensional LOSs - is presented. First, the 2D LOS is defined in terms of adjacent 1D LOSs. Then, the preliminary optimisation steps for the matrix computation are explained, namely the definition of the pixel transform and its employment (all details in Sec.3.1.1), which allow for a fast calculation of the elements a_{ij}. Lastly, the test of the algorithm is presented, using synthetic signals, in order to model key experimental features of the beam and assess the algorithm performance when background luminosity, beam optics, beam homogeneity and pixel resolution are varied. A dedicated section shows the formal steps to obtain the synthetic signals along each 2D LOS, assuming each beamlet emissivity to have a two-dimensional Gaussian profile. It must be noted that, for the scope of this chapter, the emissivity is expressed in arbitrary units and a physical interpretation of the emissivity reconstructed from experimental data will be obtained in Chapter 4.

3.1. Two-dimensional Lines-Of-Sight

One-dimensional LOSs of all cameras are provided as a set of N pairs of parameters $(m_i, q_i)_{i=1,\dots,N}$, one for each pixel composing the sensor of the camera. A two-dimensional

LOS is the region enclosed between two one-dimensional LOSs, as shown in Fig.3.1:

$$\text{LOS}_i^{(2D)} = \left\{ (x,y) \in \mathbb{R}^2 \mid y \geq m_i x + q_i \wedge y < m_{i+1} x + q_{i+1} \right\} \qquad i = 1, \ldots, N$$

All one-dimensional Lines-Of-Sight of one camera have the same origin, which is the position of the camera (which is assumed to be point-like) $P_c = (x_c, y_c)$. In the case of SPIDER, the tomographic pixels are chosen to be rectangular, as it represents the simplest shape and offers good tessellation of the SPIDER grid. Given N LOSs and
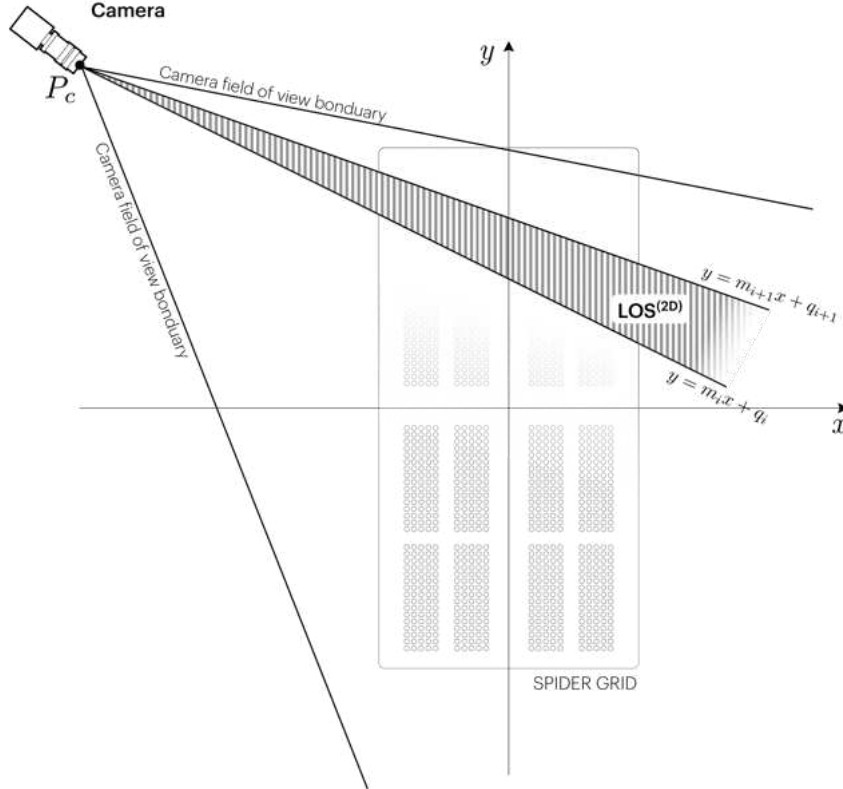

Figure 3.1: Each camera field of view is divided into strips by many one-dimensional LOSs (in the order of 10^3) and points roughly towards the beam. A two-dimensional LOS is the region between two adjacent one-dimensional LOSs, defined in terms of their respective angular coefficient and intercept. The width of the LOS is exaggerated for easier display and the representation is not to scale. Some apertures of SPIDER are masked as well for the sake of clarity.

M tomographic pixels into which the beam emissivity pattern in subdivided, $\mathbf{a}$ is the $M \times N$ matrix which encodes the geometry of the reconstruction problem. Using 2D LOSs implies that each element of $\mathbf{a}$, a_{ij}, is the fraction of the pixels area of the ith tomographic pixel of the pattern intersected by the jth two-dimensional LOS. The easier way to calculate each element could be scanning across each tomographic pixel and each LOS and compute the area of the resulting intersection polygons. This is, however, very inefficient, as the number of intersections to compute can be very large and, in the specific case of SPIDER, many of them are null, since one LOS intercepts only an limited

number of tomographic pixels. From the point of view of the tomographic pixel, most of the LOS lays outside its boundaries. Indeed, the total number of LOSs provided in SPIDER is 28991 and the number of tomographic pixels, in this particular work, ranges from 16 (80 beamlets per pixel) up to 1280 (1 beamlet per pixel), presenting a extremal case of $28991 \times 1280 > 37$ million elements, the majority of them being 0. Therefore, a fast and efficient way to compute the elements of the matrix $\mathbf{a}$ is needed as fundamental step for all following developments.

The first step is to reduce the amount of intersections (between the LOSs and the sides of each pixel) to compute, considering only LOSs which end up crossing a given tomographic pixel. Since each 1D Line-Of-Sight is given in cartesian form $y = mx + q$, one can consider in the parameter space (m, q) a region - defined by the tomographic pixel. Each point (m, q) inside this region identifies a unique line which is guaranteed to intersect the tomographic pixel in the (x, y) space. Such mapping between the tomographic pixel and its representation in terms of intersecting lines is named pixel transform.

3.1.1. The pixel transform

Assuming the tomographic pixel to be rectangular, one shall label its corners in clockwise order starting from the bottom-left one as L, M, N and O (see Fig.3.2), with

$$y_L = y_O \qquad\qquad x_L = x_M$$
$$y_M = y_N \qquad\qquad x_N = x_O$$
$$y_L < y_M \qquad\qquad x_L < x_O$$

To obtain the pixel transform for all lines a test camera, located in $P_c = (x_c, y_c)$, is
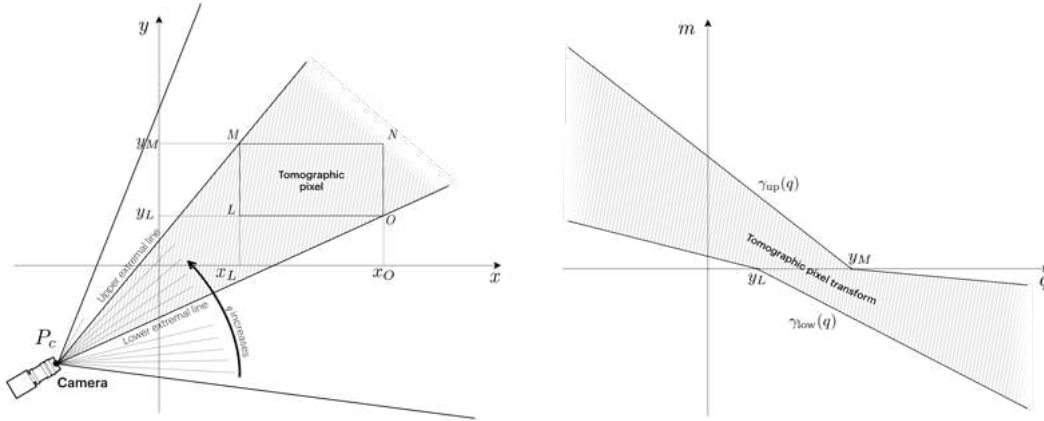

Figure 3.2: The pixel transform identifies a region in the (m, q) space (on the right) where all lines with varying m and q intersect the pixel in the (x, y) space (on the left).

considered, where $x_c < x_L$, casting a fan of lines enveloping the pixel. Three cases must be considered:

- the camera is below the bottom edge of the pixel: $y_c \leq y_L$;

- the camera is aligned with the pixel: $y_L < y_c < y_M$;

- the camera is above the pixel: $y_c \geq y_M$.

As shown in Fig.3.2, the fan contains two extremal lines, respectively the lower line, such that all lines below will not intersect the pixel, and the upper line, such that all lines above will not intersect the pixel. The pixel transform is the region of the (m, q) plane included between the two curves $\gamma_{\mathrm{up}}(q)$ and $\gamma_{\mathrm{low}}(q)$ which are the image of the upper and lower extremal lines. All points (m, q) in between define a line intersecting the pixel.

$$\gamma_{\mathrm{up}}(q) : \ q \to \gamma_{\mathrm{up}}(q) = (q, m_{\mathrm{up}}(q))$$
$$\gamma_{\mathrm{low}}(q) : \ q \to \gamma_{\mathrm{low}}(q) = (q, m_{\mathrm{low}}(q))$$

Notice that, for each case, the upper and lower lines are touching different corners of the pixel, therefore the following calculations will be presented for all three cases shown before (Fig.3.2), considering the proper extremal line starting from the camera position. Respectively, for the three cases:

- $y_c \leq y_L$: the lower extremal line is defined by the segment $\overline{P_c O}$, the upper extremal line by $\overline{P_c M}$;

- $y_L < y_c < y_M$: the lower extremal line is defined by the segment $\overline{P_c L}$, the upper extremal line by $\overline{P_c M}$;

- $y_c \geq y_M$: the lower extremal line is defined by the segment $\overline{P_c L}$, the upper extremal line by $\overline{P_c N}$.

The computation of the pixel transform is now carried out for all lines with (m, q) parameters, setting the test camera at a given value of q and scanning along all its LOSs. The process it iterated moving the test camera along the $\hat{y}$ direction to a new value of q. Starting from the first case, the region will be bound in $q \in [y_L, -\infty)$. Considering the lower line, one can express its angular coefficient as a function of its intercept as:
$$m_{\mathrm{low}} = \frac{y_O - q}{x_O}$$
while for the upper line
$$m_{\mathrm{up}} = \frac{y_M - q}{x_M}$$
For the second case $q \in (y_L, y_M)$ and

$$m_{\mathrm{low}} = \frac{y_L - q}{x_L}$$
$$m_{\mathrm{up}} = \frac{y_M - q}{x_M}$$

while for the third case $q \in [y_M, +\infty)$ and

$$m_{\text{low}} = \frac{y_L - q}{x_L}$$
$$m_{\text{up}} = \frac{y_N - q}{x_N}$$

An analogous system can be applied to the $x_c > x_O$ case, only the edges touched by the extremal lines change, as it corresponds to a reflection along the $\hat{y}$ axis:

$$L \leftrightarrow O \qquad\qquad\qquad M \leftrightarrow N$$

In this way, LOSs which are intersecting the pixel are guaranteed to lay inside the pixel transform in the (m, q) space. This preliminary step saves a huge amount of time in the following operation which are much more time and resource intensive such as the intersection computation.

Since two-dimensional LOS are used, in reality, an extra line beyond each extremal one is considered as its surface would still intersect the pixel. The resulting intersection between the 2D LOS and the tomographic pixel can have a variety of shapes, from trianglular to hexagonal, and are mostly irregular. For this reason, the intersection and area computation of each element is carried using the `Polyshape` method of `MATLAB` [45].

3.2. a matrix computation

The algorithm for the computation of the **a** matrix starts by defining a polygon describing the two-dimensional LOS, using the `MATLAB Polyshape` method, and the set of polygons describing the tomographic pixel. Now, iterating over the pixels, the pixel transform is computed and the intersecting 1D LOSs are selected with the associated 2D LOSs. In particular, the LOS polygon is constructed by considering a rectangular safety outline all around the tomographic pixel pattern with limits $[x_1, x_2]$ and $[y_1, y_2]$, as shown in Fig.3.3. The outline may be intended as the PG edge and it is defined to make sure that the LOS polygons are regular in the region of interest where tomographic pixels lie, as will be soon explained. Note that the outline does not carry any real experimental meaning, and can be set around the tomographic pixel pattern quite arbitrarily, provided that it lays sufficiently far from the pixels and the cameras (and between the two). For this work, the profile of the SPIDER grid is considered a good choice given the relative distance of the tomographic pixels from its edge and the width of the 2D LOSs. The x coordinate of the LOS polygon's vertices coincide with the ones of the outline, while the y coordinates of the LOS polygon vertices are computed using the two one-dimensional Lines-Of-Sight equations (here setting $j = 1$ without losing generality):

$$y_{1,1} = m_1 x_1 + q_1 \qquad\qquad y_{1,2} = m_2 x_1 + q_2$$
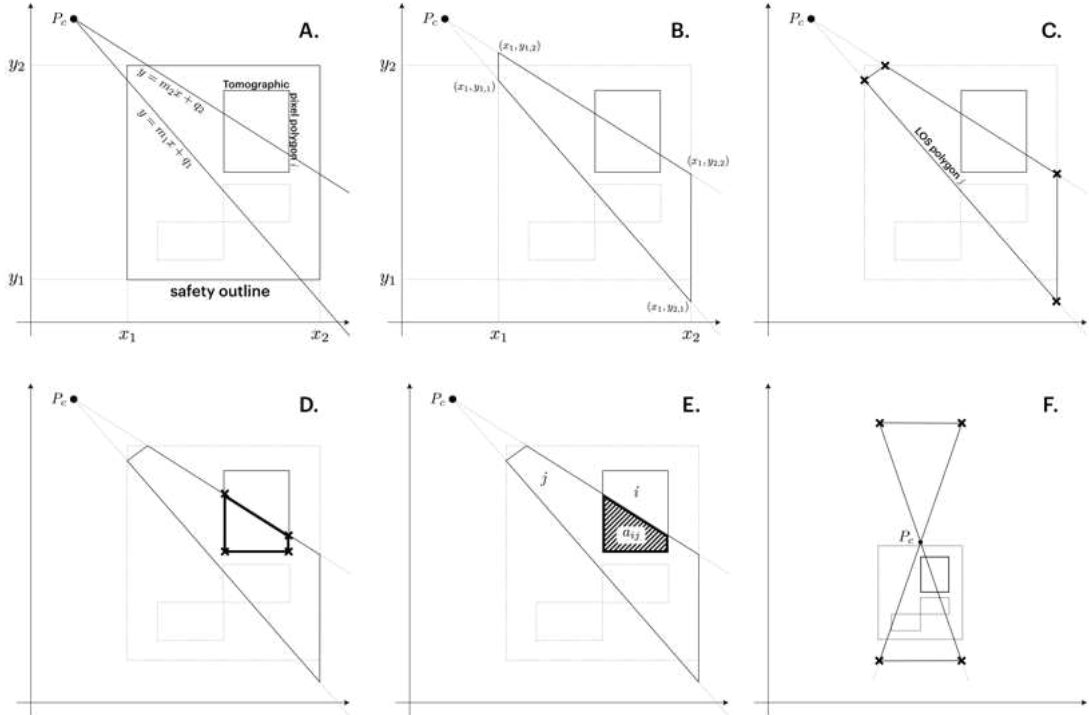$$y_{2,1} = m_1 x_2 + q_1 \qquad\qquad y_{2,2} = m_2 x_2 + q_2$$

Figure 3.3: A schematic representation of the steps for the computation of the **a** matrix. In **A.** the tomographic pixel is selected and defined as a polygon. The 1D LOSs are selected using the pixel transform and a safety outline is set. In **B.** the vertices of the 2D LOS polygon are computed using the line equation and the safety outline boundaries. In **C.** the outlying vertices of the LOS polygon are regularised. In **D.** the intersection between the two polygon is computed and in **E.** the area is calculated and stored in the a_{ij} element of the matrix. In **F.**, an example of irregular polygon case which requires the safety outline for regularisation.

The `Polyshape` method offers good flexibility. Indeed, the tomographic pixel can have an arbitrary amount of vertices and be irregular in shape. Therefore, the possibility of designing (roughly) circular or hexagonal tomographic pixels (e.g. in the case of beamlet apertures placed on a triangular lattice instead of rectangular, like SPIDER's, where hexagonal tomographic pixel would offer a better tessellation) is available. This allows this algorithm to be more easily adapted to a variety of geometries, not only in the framework of negative ion beams. A limitation of the `Polyshape` method is the production of self-intersecting LOSs polygons, which may arise from very steep LOSs whose vertices lay above the camera position, producing a hourglass shape, whose behaviour is not well defined and must be avoided for complete control over the algorithm[1](see Fig.3.3 **F.**). In particular, these artefacts are produced when $x_c \in [x_1, x_2]$, and they are a direct consequence of the geometrical construction of the algorithm and do not carry any physical meaning. However, they may result in inaccurate intersection calculation

---

[1]MATLAB `Polyshape` self-corrects the design of the irregular tomographic pixel, but the process is not under the direct control of the user. Testing shows that the correction is usually faulty and does not correspond to the correct LOSs shape.

a matrix element evaluation. As the calculation for the y component of the edges of the LOS polygon is carried out using the LOS equation, up to two edges may result with $y > y_c$, producing a self-intersecting shape. For this reason, if the vertex of the LOS polygon is above the outline, the x coordinate of the vertex is recalculated such that the corresponding y coordinates lays on the outline while still being a solution of the LOS equation. Therefore, the possible application of this algorithm in other scenarios must ensure that sufficient spacing, between the outline and the tomographic pixel pattern and between the outline and the camera position, is provided. The production of irregular polygons is paired with warnings from `MATLAB Polyshape` and troubleshooting should first investigate this spacing requirement. Notice that for the bottom side of the outline this operation is not performed as there are no cameras on the bottom of the experiment and there is no risk of irregular polygon generation. After this regularisation step, the intersection of the LOS polygon and the tomographic pixel polygon is computed and its area is calculated:

$$a_{ij} = \texttt{area(intersect(LOSPolygon}_j\texttt{,TomographicPixelPolygon}_i\texttt{))}$$

These are the most time-consuming steps and are the reason for all the optimisations shown in the previous sections.

3.3. Synthetic signals

To test the behaviour and performance of the reconstruction algorithm in a variety of scenarios, which will be discussed later, a model of the full beam is developed. For this purpose, each beamlet emissivity is assumed to be a 2D Gaussian in amplitude (centred on the nominal position of the beamlet) and the resulting beam model is integrated inside each 2D LOS, producing synthetic signals. These are used as input for the SART algorithm, in order to compare the tomographic reconstruction results with the beam simulation. The discussion is first presented in terms of signal generation from one beamlet, since the extension to a full beamlet array is linear.

Figure 3.4: Each beamlet emissivity is modelled with a gaussian centred on its nominal position.

The emissivity of each beamlet is modelled with a gaussian centred in its nominal position $P = (x_g, y_g)$ and with width σ_g (see Fig. 3.4):

$$G(x, y) = A\, e^{-\frac{1}{2\sigma^2}\left((x-x_g)^2 + (y-y_g)^2\right)}$$

The signal measured along one 2D LOS is evaluated by integrating the emissivity function in the region $S = \text{LOS}_{j=1}^{(2D)}$ between two lines $r_1 = m_1 x + q_1$ and $r_2 = m_2 x + q_2$, as
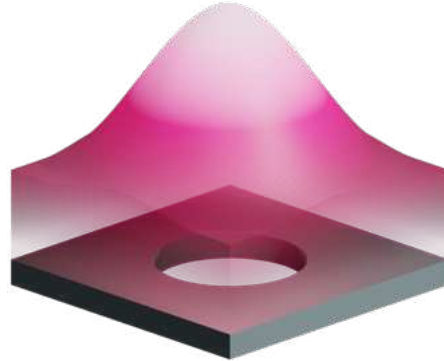
shown in Fig.3.5. These two adjacent lines are selected from the set of LOSs belonging to one camera, corresponding to the ith line and the $(i+1)^{\text{th}}$ line. The integral in these
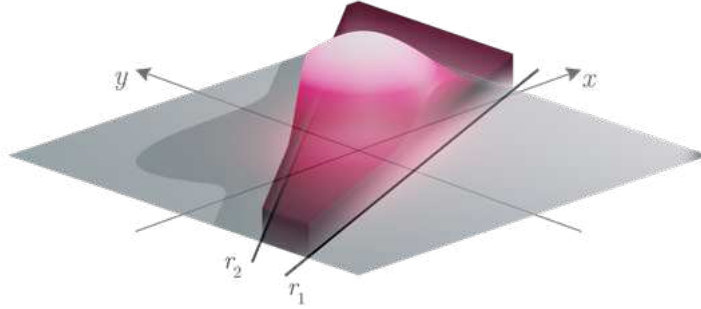

Figure 3.5: The emissivity is integrated over the two-dimensional region delimited by two one-dimensional LOSs r_1 and r_2.

coordinates is:

$$I = \int_S G(x, y) \, \mathrm{d}S = \int_{-\infty}^{+\infty} \int_{y=r_1}^{y=r_2} G(x, y) \, \mathrm{d}y \, \mathrm{d}x$$

This can be simplified by splitting it into two integrals spanning an infinite region. Integrated areas outside the region S would cancel each other out

$$I = \int_{-\infty}^{+\infty} \int_{y=r_1}^{+\infty} G(x, y) \, \mathrm{d}y \, \mathrm{d}x - \int_{-\infty}^{+\infty} \int_{y=r_2}^{+\infty} G(x, y) \, \mathrm{d}y \, \mathrm{d}x = I_1 - I_2$$

Given the geometry of the LOSs and the simulated emissivity profile $G(x, y)$, the integral I gives the simulated integrated signals collected (or synthetic signal), which will be inverted in the tomography. The integral evaluation is shown in the next subsections. The simulated emissivity for synthetic signals, at this stage, does not hold any particular physical meaning and represents a tool for testing the algorithm. The Gaussian profile of the beamlet emissivity is chosen as best guess in terms of similarity to the real case and for the presence of analytical solutions for the 2D LOS integrals. A physical characterisation of the beam emissivity in terms of atomic processes and radiant power emitted by the beam-background interaction is presented in Chapter 4.

3.3.1. Parameterisations, first transformation and integration

To simplify the geometry of the integration of $G(x, y)$ inside the 2D LOS between the lines r_1 and r_2, the two LOSs can be parametrised in terms of their origin - which, by construction, corresponds to the camera location (where the camera is assumed to be point-like) $P_c = (x_c, y_c)$ - and their angle with respect to the horizontal axis ($\hat{x}$ axis), ϕ:

$$y = \tan \phi_i \, (x - x_c) + y_c$$

since $m_i = \tan\phi$ and

$$q_i = y_c - \tan\phi_i\, x_c$$

This will allow to operate a translation and rotation of the plane so that the integrals I_1 and I_2 can be evaluated in $[0,\infty]$ (instead of $[r_1,\infty]$ or $[r_2,\infty]$), whose exact solution is known. One can bind the two lines to have a fixed angular span $\Delta\phi$ so $\phi_2 = \phi_1 + \Delta\phi$. From now on, we shall relabel $\phi_1 \to \phi$.

It is now possible to define a coordinate transformation, which combines a rigid translation and a rotation of the plane. The goal is to shift the coordinate origin to P_c and rotate the reference frame so that the new axis $\hat{x}'$ is aligned to the line r_1. The rotation angle is thus ϕ and the translation is represented by the vector $\vec{t_c} = (x_c, y_c)^T$.
The translation operation can be encoded into a 3×3 translation matrix t

$$t = \begin{bmatrix} 1 & 0 & t_{c,x} \\ 0 & 1 & t_{c,y} \\ 0 & 0 & 1 \end{bmatrix}$$

while the rotation operation can be expressed as the usual $3{\times}3$ rotation matrix $R(\phi)$

$$R(\phi) = \begin{bmatrix} \cos\phi & -\sin\phi & 0 \\ \sin\phi & \cos\phi & 0 \\ 0 & 0 & 1 \end{bmatrix}$$

so both operations expressed by the $R(\phi)$ and t matrices are incorporated in a transformation matrix $T\left(\phi, \vec{t_c}\right)$

$$T\left(\phi, \vec{t_c}\right) = R(\phi)t = \begin{bmatrix} R(\phi) & \vec{t_c} \\ \mathbf{0} & 1 \end{bmatrix} = \begin{bmatrix} \cos\phi & -\sin\phi & x_c \\ \sin\phi & \cos\phi & y_c \\ 0 & 0 & 1 \end{bmatrix}$$

Therefore one can transform the coordinates as

$$\begin{pmatrix} x' \\ y' \\ 1 \end{pmatrix} = T\left(\phi, \vec{t_c}\right)\begin{pmatrix} x \\ y \\ 1 \end{pmatrix} = \begin{bmatrix} \cos\phi & -\sin\phi & x_c \\ \sin\phi & \cos\phi & y_c \\ 0 & 0 & 1 \end{bmatrix}\begin{pmatrix} x \\ y \\ 1 \end{pmatrix} = \begin{pmatrix} x\cos\phi - y\sin\phi + x_c \\ x\sin\phi + y\cos\phi + y_c \\ 1 \end{pmatrix}$$

One can see that r_1 is transformed to the new $\hat{x}$ axis

$$y' = x\sin\phi + y\cos\phi + y_c = \tan\phi(x\cos\phi - y\sin\phi + x_c - x_c) + y_c$$

$$y\cos\phi = -y\tan\phi\sin\phi$$

$$y = 0$$

29

and for r_2

$$y' = x\sin\phi + y\cos\phi + y_c = \tan(\phi + \Delta\phi)(x\cos\phi - y\sin\phi + x_c - x_c) + y_c$$
$$x\sin\phi + y\cos\phi = x\tan(\phi + \Delta\phi)\cos\phi - y\tan(\phi + \Delta\phi)\sin\phi$$
$$y\left(\cos\phi + \tan(\phi + \Delta\phi)\sin\phi\right) = x\left(\tan(\phi + \Delta\phi)\cos\phi - \sin\phi\right)$$
$$y\frac{\cos\Delta\phi}{\cos(\phi + \Delta\phi)} = x\frac{\sin\Delta\phi}{\cos(\phi + \Delta\phi)}$$
$$y = \tan(\Delta\phi)\,x$$

Which defines a line passing through the origin of the new axes with angular coefficient corresponding to the span of the region. Therefore the Gaussian function in the new coordinates becomes

$$G\left(T\left(\phi, \vec{t_c}\right)(x, y)\right) = A\,e^{-\frac{1}{2\sigma^2}\left((x\cos\phi - y\sin\phi + x_c - x_g)^2 + (x\sin\phi + y\cos\phi + y_c - y_g)^2\right)}$$

The exponent can be expanded as

$$(x\cos\phi - y\sin\phi + x_c - x_g)^2 + (x\sin\phi + y\cos\phi + y_c - y_g)^2 =$$
$$= x^2 + y^2 +$$
$$+ 2x\left((x_c - x_g)\cos\phi + (y_c - y_g)\sin\phi\right) +$$
$$+ 2y\left((y_c - y_g)\cos\phi - (x_c - x_g)\sin\phi\right) +$$
$$+ (x_c - x_g)^2 + (y_c - y_g)^2$$
$$= x^2 + y^2 + b_{1,x}x + b_{1,y}y + c_{1,x} + c_{1,y}$$

Where $b_{1,x} = 2\left((x_c - x_g)\cos\phi + (y_c - y_g)\sin\phi\right)$, $b_{1,y} = \left((y_c - y_g)\cos\phi - (x_c - x_g)\sin\phi\right)$, $c_{1,x} = (x_c - x_g)^2$ and $c_{1,y} = (y_c - y_g)^2$.

It is now possibile to complete the squares by using $t^2 + bt + c = (t - h)^2 + k$ where $h = b/2$ and $k = c - (b/2)^2$. Thus for both x and y this applies straightforwardly

$$= \left(x + \frac{b_{1,x}}{2}\right)^2 + c_{1,x} - \frac{b_{1,x}^2}{4} + \left(y + \frac{b_{1,y}}{2}\right)^2 + c_{1,y} - \frac{b_{1,y}^2}{4}$$
$$= (x - h_{1,x})^2 + (y - h_{1,y})^2 + k_{1,x} + k_{1,y}$$
$$= (x - h_{1,x})^2 + (y - h_{1,y})^2 + k_1$$

This produces a new Gaussian, where the effects of coordinates' rotation is shifted from the variables to the parameters $h_{1,x}$ and $h_{2,x}$. This does't hold for differing eigenvectors of the Gaussian, which would result in a rotation of the overall elliptical contours of the function.

$$G(x', y') := G_1(x, y) = A\,e^{-\frac{1}{2\sigma^2}\left((x - h_{1,x})^2 + (y - h_{1,y})^2\right)}$$

Indeed, a Gaussian function can be expressed in terms of a quadratic form matrix: $G(\vec{x}) = A\exp\left[-\frac{1}{2}(\vec{x} - \vec{x}_g)^T\Sigma^{-1}(\vec{x} - \vec{x}_g)\right]$, where $\Sigma \geq 0$ and $\Sigma_{ij} = \Sigma_{ji}$ is the invertible

quadratic form matrix. In the case where the Gaussian function has two different widths along the $\hat{x}$ and $\hat{y}$ direction, then

$$\Sigma = \begin{bmatrix} \sigma_x^2 & 0 \\ 0 & \sigma_y^2 \end{bmatrix}$$

where σ_x^2 and σ_y^2 are the two eigenvalues of Σ. The contours of the function setting $G(\vec{x}) = c$ are defined in terms of two radii R_1 and R_2:

$$R_1 = \sqrt{2\sigma_x^2 \ln\left(\frac{1}{2\pi\, c\, \sigma_x \sigma_y}\right)} \qquad R_2 = \sqrt{2\sigma_y^2 \ln\left(\frac{1}{2\pi\, c\, \sigma_x \sigma_y}\right)}$$

so that $1 = \left(\frac{x-x_0}{R_1}\right)^2 + \left(\frac{y-y_0}{R_2}\right)^2$ is an ellipse. Transformations operating on the coordinates modify the orientation of the associated eigenvectors of Σ and relative eigenvalues, modifying the contours of the Gaussian function. For more details, see Ref.[46].
Since $\Delta\phi > 0$, we shall proceed to integrate this Gaussian to obtain I_1 in the $y > 0$:

$$\begin{aligned}
I_1 &= \int_{-\infty}^{+\infty} \int_{0}^{+\infty} G_1(x,y)\, \mathrm{d}y\, \mathrm{d}x \\
&= A \int_{-\infty}^{+\infty} e^{-\frac{1}{2\sigma^2}(x-h_{1,x})^2}\, \mathrm{d}x \int_{0}^{+\infty} e^{-\frac{1}{2\sigma^2}(y-h_{1,y})^2}\, \mathrm{d}y \\
&= A\, \sigma\sqrt{2\pi}\, \sigma\sqrt{\frac{\pi}{2}}\left(1 + \mathrm{erf}\left(\frac{h_{y,1}}{\sigma\sqrt{2}}\right)\right) \\
&= A\, \pi\sigma^2\left(1 + \mathrm{erf}\left(\frac{h_{y,1}}{\sigma\sqrt{2}}\right)\right)
\end{aligned}$$

3.3.2. Second transformation and integration

It is possible to repeat the same process by rotating the latter coordinates of angle $\Delta\phi$, to align the second line to the $\hat{x}$ axis. Thus one can use a rotation matrix $R(\Delta\phi)$

$$\begin{pmatrix} x'' \\ y'' \end{pmatrix} = \begin{bmatrix} \cos(\Delta\phi) & -\sin(\Delta\phi) \\ \sin(\Delta\phi) & \cos(\Delta\phi) \end{bmatrix} \begin{pmatrix} x' \\ y' \end{pmatrix} = \begin{pmatrix} x'\cos(\Delta\phi) - y'\sin(\Delta\phi) \\ x'\sin(\Delta\phi) + y'\cos(\Delta\phi) \end{pmatrix}$$

One can see that the two lines now switch roles. Relabelling $(x'', y'') \leftrightarrow (x', y') \leftrightarrow (x, y)$, the second line now becomes the new $\hat{x}$ axis:

$$\begin{aligned}
x\sin(\Delta\phi) + y\cos(\Delta\phi) &= \tan(\Delta\phi)(x\cos(\Delta\phi) - y\sin(\Delta\phi)) \\
y(\cos(\Delta\phi) + \tan(\Delta\phi)\sin(\Delta\phi)) &= 0 \\
y &= 0
\end{aligned}$$

While for the first line it is tilted down of the same angle:

$$x\sin(\Delta\phi) + y\cos(\Delta\phi) = 0$$
$$y = -x\tan(\Delta\phi)$$
$$y = x\tan(-\Delta\phi)$$

For the new gaussian function one obtains

$$G\left(R(\Delta\phi)(x,y)\right) := G_2(x,y) = A\,e^{-\frac{1}{2\sigma}\left((x\cos(\Delta\phi)-y\sin(\Delta\phi)-h_{1,x})^2+(x\sin(\Delta\phi)+y\cos(\Delta\phi)-h_{1,y})^2\right)}$$

For the exponent one can repeat the same steps of the first transformation except now the translation term (x_c, y_c) is absent:

$$(x\cos(\Delta\phi) - y\sin(\Delta\phi) - h_{1,x})^2 + (x\sin(\Delta\phi) + y\cos(\Delta\phi) - h_{1,y})^2 =$$
$$= x^2 + y^2 +$$
$$- 2x(h_{1,x}\cos(\Delta\phi) + h_{1,y}\sin(\Delta\phi)) +$$
$$+ 2y(h_{1,x}\sin(\Delta\phi) - h_{1,y}\cos(\Delta\phi)) +$$
$$+ h_{1,x} + h_{1,y}$$
$$= x^2 + y^2 + b_{2,x}x + b_{2,y}y + c_{2,x} + c_{2,y}$$
$$\vdots$$
$$= (x - h_{2,x})^2 + (y - h_{2,y})^2 + k_2$$

where $h_{2,x} = b_{2,x}/2$, $h_{2,y} = b_{2,y}/2$ and $k_2 = k_{2,x} + k_{2,y} = c_{2,x} - (b_{2,x}/2)^2 + c_{2,y} - (b_{2,y}/2)^2 = 0$. Therefore the gaussian function can be simplified to

$$G_2(x,y) = A\,e^{-\frac{1}{2\sigma^2}\left((x-h_{2,x})^2+(y-h_{2,y})^2\right)}$$

Now one can simply integrate the gaussian in the plane $y > 0$ to obtain I_2

$$I_2 = \int_{-\infty}^{+\infty}\int_0^{+\infty} G_2(x,y)\,\mathrm{d}y\,\mathrm{d}x$$
$$= A\int_{-\infty}^{+\infty} e^{-\frac{1}{2\sigma^2}(x-h_{2,x})^2}\,\mathrm{d}x\int_0^{+\infty} e^{-\frac{1}{2\sigma^2}(y-h_{2,y})^2}\,\mathrm{d}y$$
$$= A\sigma\sqrt{2\pi}\sigma\sqrt{\frac{\pi}{2}}\left(1 + \mathrm{erf}\left(\frac{h_{2,y}}{\sigma\sqrt{2}}\right)\right)$$
$$= A\pi\sigma^2\left(1 + \mathrm{erf}\left(\frac{h_{2,y}}{\sigma\sqrt{2}}\right)\right)$$

3.3.3. Merging

The complete integral becomes

$$I = I_1 - I_2 = A\pi\sigma^2 \left[\mathrm{erf}\left(\frac{h_{y,1}}{\sigma\sqrt{2}} \right) - \mathrm{erf}\left(\frac{h_{2,y}}{\sigma\sqrt{2}} \right) \right]$$

$$= A\pi\sigma^2 \left[\mathrm{erf}\left(\frac{(y_g - y_c)\cos\phi - (x_g - x_c)\sin\phi}{\sigma\sqrt{2}} \right) + \right.$$

$$\left. - \mathrm{erf}\left(\frac{(y_g - y_c)\cos(\Delta\phi + \phi) - (x_g - x_c)\sin(\Delta\phi + \phi)}{\sigma\sqrt{2}} \right) \right]$$

In the case of G Gaussian beamlets:

$$F_G(x,y) = \sum_{g=1}^{G} A_g \, e^{-\frac{1}{2\sigma_g^2}\left((x-x_g)^2 + (y-y_g)^2\right)}$$

one can simply sum over all gaussians to obtain the total LOS integral

$$I_G = \sum_{g=1}^{G} A_g \pi\sigma_g^2 \left[\mathrm{erf}\left(\frac{(y_g - y_c)\cos\phi - (x_g - x_c)\sin\phi}{\sigma_g\sqrt{2}} \right) + \right.$$

$$\left. - \mathrm{erf}\left(\frac{(y_g - y_c)\cos(\Delta\phi + \phi) - (x_g - x_c)\sin(\Delta\phi + \phi)}{\sigma_g\sqrt{2}} \right) \right]$$

Notice that the integral is carried along $\hat{x}$ in $\mathbb{R}$, when, more rigorously, should be carried from the camera abscissa x_c to infinity. However, this would introduce computational complexity without bringing additional precision, as the cameras are assumed to be sufficiently far from the beamlets so that the emissivity values are negligible away from the beam. The integral can thus be extended to $x \in \mathbb{R}$.

3.3.4. Inverse parametrisation

For more practical purposes, LOSs are provided in the m_i, q_i parametrisation. Therefore, one may obtain P_c and ϕ, $\Delta\phi$ as a function of the latter. For P_c one can set

$$m_1 x_c + q_1 = m_2 x_c + q_2 \implies x_c = \frac{q_2 - q_1}{m_1 - m_2}$$

hence one can take either r_1 or r_2

$$y_c = m_1 x_c + q_1 = \frac{m_1(q_2 - q_1)}{m_1 - m_2} + q_1 = \frac{m_1(q_2 - q_1) + q_1(m_1 - m_2)}{m_1 - m_2}$$

For the angular term things are not as straightforward. While one can determine the angular coefficient of the LOS from a pointing angle of the camera using $m_i = \tan\phi_i$, the inverse problem to retrieve the angle from the angular coefficient cannot be solved by just using the inverse function $\phi = \arctan m_i$ as the $\arctan(\cdot)$ function is the inverse

33

of just one branch of the $\tan(\cdot)$ function. This means that each couple of angles ϕ_a, ϕ_b in $[0, \pi]/\{\pi/2\}$ or $[0, -\pi]/\{-\pi/2\}$ such that $\phi_{a,b} = \pm(\pi/2) \pm \Delta\varphi$ (for some $\varphi \in [0, \pi/2]$) are mapped by $\tan\phi$ to the same range, loosing information on the angle. This intuitively is due to the fact that a line is a linear variety (parametrised by one angular coefficient) which can be generated by two vectors with pointing angles π radians apart. Then, the inversion using $\arctan(\cdot)$ maps everything to $\phi_i \in [-\pi/2, \pi/2]$. This may cause computational issues in `MATLAB`.

In the specific case of SPIDER, all cameras point to the origin and are roughly placed on a circle centred on it. We can use this information to reconstruct the original angle. One shall first convert the position of the camera in polar coordinates

$$P_c = (r_c, \theta_c)$$

Then, one may compute the camera pointing direction

$$\theta_{\mathrm{dir}} = \theta_c - \mathrm{sign}(\theta_c)\pi$$

where

$$\mathrm{sign}(x) = \begin{cases} 1 & \text{if} \quad x \geq 0 \\ -1 & \text{if} \quad x < 0 \end{cases}$$

Then, one can compute for two LOSs belonging to one camera

$$\phi = \phi_1 = g(m_1, \theta_{\mathrm{dir}}) \qquad \phi_2 = g(m_2, \theta_{\mathrm{dir}})$$

where the function $g(m, \theta)$ is defined as follows:

$$g\left(m, \theta_{\mathrm{dir}}\right) = \begin{cases} \mathrm{atan}(m) + \pi & \text{if} \quad \theta_{\mathrm{dir}} \in \left[\pi, \frac{3}{4}\pi\right) \\ -\mathrm{acot}(m) + \frac{\pi}{2} & \text{if} \quad \theta_{\mathrm{dir}} \in \left[\frac{3}{4}\pi, \frac{1}{4}\pi\right) \\ \mathrm{atan}(m) & \text{if} \quad \theta_{\mathrm{dir}} \in \left[\frac{1}{4}\pi, -\frac{1}{4}\pi\right) \\ -\mathrm{acot}(m) - \frac{\pi}{2} & \text{if} \quad \theta_{\mathrm{dir}} \in \left[-\frac{1}{4}\pi, \frac{3}{4}\pi\right) \\ \mathrm{atan}(m) - \pi & \text{if} \quad \theta_{\mathrm{dir}} \in \left[-\frac{3}{4}\pi, -\pi\right] \end{cases}$$

And finally

$$\Delta\phi = \phi_1 - \phi_2$$

3.4. Performance testing of the reconstruction algorithm on the simulated beam

Synthetic signals allow to quantify the quality of the reconstruction in various experimental conditions, studying a variety of features of SPIDER beam. In particular, some key aspects of both the beam and the tomographic domain and geometry are investigated:

- beamlet resolution: the beamlet resolution is defined as the number of beamlets contained in a tomographic pixel. Since the SPIDER beam is divided into 16 groups of 80 beamlets, the study of the tomographic reconstruction resolution starts by covering each group with a single tomographic pixel, resulting in a resolution of 80 beamlets, followed by 40, 20, 10, 5 and 1 beamlet, as shown in Fig.3.6. As the beamlet resolution increases (respectively, the number of beamlets per tomographic pixel decreases), an increase in spatial resolution is obtained. The cost is a loss of accuracy in the reconstruction since the number of unknowns increases too;
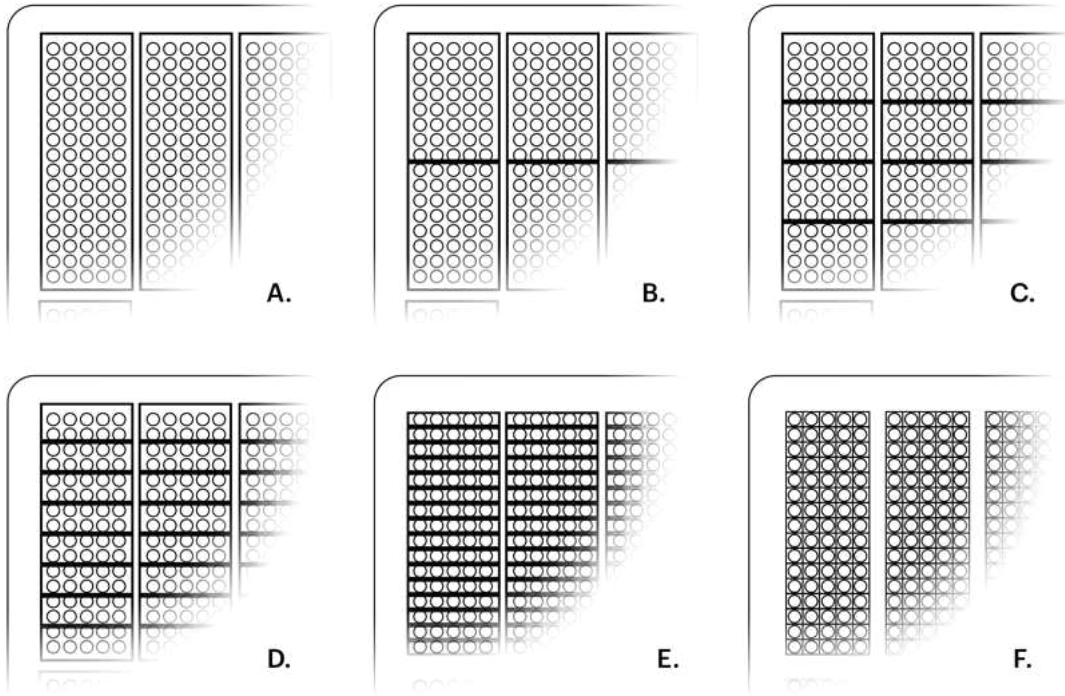

Figure 3.6: The different beamlet resolutions of this work. The six pictures show a zoomed portion of the SPIDER grid. In **A.** each tomographic pixel covers each beamlet group of 80 beamlets, for a total of 16 tomographic pixels. In **B.** each group is covered by two tomographic pixels, with a resolution of 40 beamlets. In **C.** a further subdivision is carried out with a resolution of 20 beamlets per tomographic pixel. In **D.** the resolution is increased to 10 beamlets, in **E.** to 5 and in **F.** the resolution is raised to one beamlet per tomographic pixel.

- beamlet width: the beam optics is one of the most important parameters for NBIs. When source and accelerator parameters vary, the beamlet optics change too, as it is found during the previous experimental campaigns. This results in a modification of the beamlet width σ, according to the relation which links beam divergence δ and width:

$$\sigma = \sigma_0 + \delta \times z$$

where z is the position observed by cameras and σ_0 the width of the beamlet at the

end of the accelerator. The beam width may cause a significant amount of overlap between beamlets, rendering the reconstruction more challenging. One shall thus distinguish two cases: good beam optics, where beamlets are well separated and comply to the ITER requirement of 7 mrad divergence resulting in $\sigma_g = 6.5$ mm, and bad beam optics, with $\sigma_g = 11$ mm - which corresponds to an experimentally measured divergence of 20 mrad;

- background intensity: background light is an inevitable component of beam environment. Even though cameras point against a darkened strip for contrast, stray light can still affect the measurement, coming from different sources: the beam plasma (the inter-beamlet region where a diffuse ionised gas emits light), beam reflections against the vessel walls and source light (coming from the SPIDER drivers and acceleration section). To simulate this component, an additional wide ($\sigma = 600$ mm) 2D Gaussian emissivity is added to the simulated beam with intensity ranging from 1% to 5% (for realistic experimental scenarios), up to 20%;

- Poissonian noise: camera signals are subjected to electronic noise. A random Poissonian noise is added to the synthetic signals to simulate sensor noise and its maximum amplitude is a percentage of the signal itself. A low noise case considers a 1% noise amplitude, while a high noise case is estimated with a 5% intensity. The performance will be studied with noise levels up to 20%;

- beam homogeneity: beam non-homogeneity lower than 10% is required for ITER NBIs. During the last experimental campaign, SPIDER beam homogeneity is deeply studied (Ref.[31]), finding a minimum around 82/80%, in the explored experimental conditions. To simulate this, the beamlet amplitude can be varied across its section. Two cases have been studied: a uniform distribution and an emissivity gradient along the $\hat{y}$ axis across each group, which is a non-homogeneity experimentally observed.

In order to quantify the capabilities and the limits of the tomographic algorithm developed, different simulations of the beam emissivity are performed. For each simulation, the integrated signals have been evaluated and then inverted to be compared with the simulation. To make a direct comparison between simulation and inversion, also the simulated beamlet emissivity is discretised in the tomographic pixels to obtain the effective emissivity $\hat{\epsilon}_i$

$$\hat{\epsilon}_i = \int_{\text{Tom. pixel}_i} \sum_g A_g\, e^{-\frac{1}{2\sigma_g^2}\left((x-x_g)^2+(y-y_g)^2\right)}\ \mathrm{d}x\, \mathrm{d}y$$

where the beamlet index g runs over all beamlets contained in the tomographic pixel. Notice that $\hat{\epsilon}_i$ is an alternative way of computing the total beamlet emissivity (only) contained inside a given tomographic pixel, which is independent of LOS integration and SART reconstruction. This represents the desired output of the algorithm: the evaluation of $\hat{\epsilon}_i$ is unaffected by background and noise, since only the Gaussian emissivity of the beamlets is integrated inside the tomographic pixel, and errors derived by the SART iterative process. It must be stressed that, instead, the simulated signals I_j

are affected by light background and noise and these factors are carried into the reconstruction of ϵ_i. Therefore, $\hat{\epsilon}_i$ represents only the emissivity provided by the beamlets inside the tomographic pixel i or, equivalently, the ideal output of the SART algorithm in the ideal experimental scenario (with no background affecting the measurement and no noise due to the use of camera sensors).

To quantify the goodness of the reconstruction, the reconstruction Root Mean Square is used, $\mathrm{RMS_{rec.}}$, defined as the Root Mean Square of the normalised residuals

$$R_{\epsilon_i} = \left(\frac{\hat{\epsilon}_i - \epsilon_i}{\hat{\epsilon}_i} \right)$$

between the tomographic reconstruction and the real emissivity value of the tomographic pixels:

$$\mathrm{RMS_{rec.}} = \mathrm{rms}\,(R_{\epsilon_i})_{i=1,...,M} = \frac{1}{\sqrt{M}} \sqrt{\sum_i^M R_{\epsilon_i}^2} \tag{3.1}$$

The $\mathrm{RMS_{rec.}}$ is expressed in percentage and the lower its value, the closer the emissivity reconstruction is to the ideal result.

A second quantifier is defined to assess the beam homogeneity from the reconstruction, $\Delta_{\mathrm{rec.}}$:

$$\Delta_{\mathrm{rec.}} = \frac{\mathrm{rms}\,(\epsilon_i \times \Sigma_i - \langle \epsilon_i \times \Sigma_i \rangle)}{\langle \epsilon_i \times \Sigma_i \rangle} \tag{3.2}$$

where Σ_i is the area of the tomographic pixel i and $\langle \epsilon_i \times \Sigma_i \rangle$ is the average value of the total reconstructed light inside the tomographic pixels (this compensates for the different sizes of the pixels inside the pattern). Expressed as a percentage, $\Delta_{\mathrm{rec.}}$ quantifies the inhomogeneity of the beam or, equivalently, the deviation of the homogeneity from 100% (perfectly homogenous, i.e. all reconstructed beamlets have the same emissivity). This allows to assess the capability of the algorithm to assess the beam uniformity and can be tested by setting a known homogeneity in the simulated beam.

3.4.1. Summary of performance assessment of the algorithm

In this section the results of the analysis of the reconstruction algorithm performance are presented for two full-beam homogeneity cases: the homogenous beam, with Gaussian amplitudes all set to $A_g = 1$, and the inhomogeneous beam, with an emissivity amplitude modulation via a function defined as

$$A_g(y_g) = 1 + \frac{1}{4}\left(\frac{y_g}{400} - \left\lfloor \frac{y_g}{400} \right\rfloor \right) \tag{3.3}$$

which modulates the beamlet amplitudes, along the $\hat{y}$ direction with a linear ramp inside each beamlet group, with an excursion of 20%. Both simulated beams are shown in Figs3.7a/3.7b, with beamlet width set to $\sigma = 6.5$ mm. This allows to simulate the the beam inhomogeneities observed in experimental campaigns (see Ref.[41]), which result to be up to 20% (in the 28 open-beamlet setup). The capability of the algorithm

of recognising and characterising the beam homogeneity accurately is of fundamental importance, as ITER NBI sets strict requirement of 90% minimum uniformity.
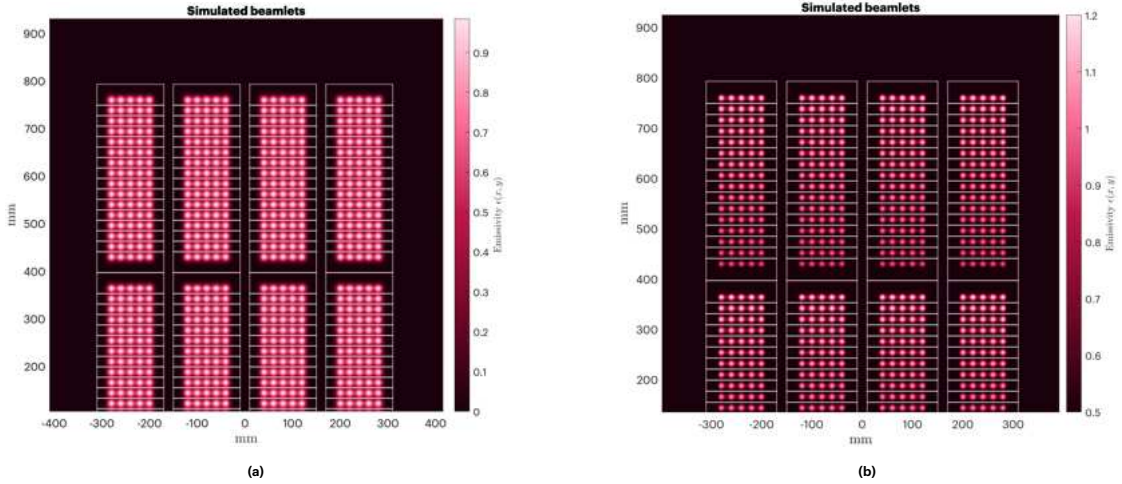

Figure 3.7: On the left **a**: a zoomed portion of the SPIDER beam shows the beamlet emissivity and the white outlines of the tomographic pixels, here with a resolution of 5 beamlets. In **b**, on the right, the same setup but with the non-homogenous simulated emissivity, with an emissivity gradient along $\hat{y}$ along each group (here in enhanced colours for clarity).

In all following assessments, the SART algorithm iterates until convergence is reached, i.e. the difference of correction terms between iterations approaches zero, usually between 15/20 iterations.

For each homogeneity case, parameter scans follow, first by scanning in beamlet resolution for optimal beam optics ($\sigma = 6.5$ mm - $\delta = 7$ mrad divergence) and non-optimal beam optics ($\sigma = 11$ mm - $\delta = 20$ mrad divergence) with no background and signal noise. This allows to assess the algorithm accuracy (with $\mathrm{RMS_{rec.}}$) as the resolution becomes more demanding and the number of variables (i.e. the number of tomographic pixels to reconstruct) increases. Then, the beamlet resolution is set the highest resolution compatible with low $\mathrm{RMS_{rec.}}$ (about 10%, representing an acceptable reconstruction error) for parameter scanning of Poissonian noise and background light intensity. It will be shown that a 5-beamlet resolution (one in-group beamlet line) will satisfy this requirement and represents a suitable compromise between tomography resolution and computational time. Indeed, a single-beamlet reconstruction is highly time-consuming, while a 5-beamlet resolution allows for a much faster process without loosing homogeneity characterisation along the $\hat{y}$ direction (as a 5-beamlet tomographic pixel is designed to include one line of 5 beamlets across the width of a beamlet group. See Fig.3.6 **E.**) - along which non-uniformity has been observed. In the following observations, parameters are assumed to be independently affecting the reconstruction accuracy, which allows to selectively scan the algorithm behaviour. Finally, SPIDER data are used to discuss the algorithm performance on experimental scenarios in the 28 beamlet configuration.
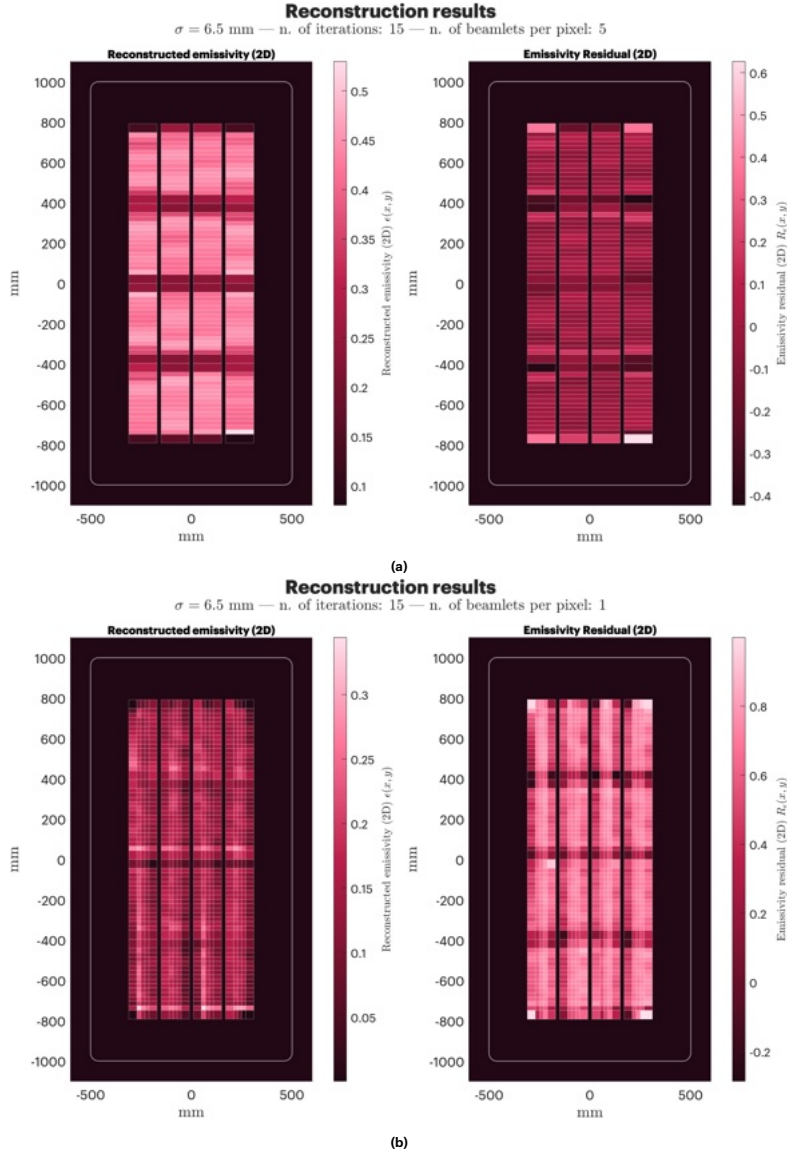
Figure 3.8: Examples of reconstruction of the uniform beam. On the top panel **a**: on the left, the reconstructed emissivity at 5-beamlet resolution. On right, the normalised residuals R_{ϵ_i}. On the bottom panel **b**: on the left, the reconstructed emissivity at 1-beamlet resolution and, on the right, the normalised residuals. The increased inaccuracy in the construction can be best observed in the residuals, where a clear difference in magnitude between the two resolutions cases can be seem in the colours. The 1-beamlet resolution reconstruction presents higher residuals, indicating the reduced accuracy due to the increased number of tomographic pixels.

3.4.2. Performance assessment varying resolution

First of all, the resolution of the tomographic reconstruction when the number of pixels changes is studied, i.e. 80, 40, 20, 10, 5 and 1-beamlet resolutions. The two reconstructions with 5 and 1-beamlet resolutions are shown in Figs.3.8a/3.8b (top panel and bottom panel respectively): on the left, the reconstruction result is shown. On the right, the residuals R_{ϵ_i} are shown. The values in the latter show a clear distinction between the

reconstruction accuracy in the two cases: the 1-beamlet resolution case features much higher residuals in magnitude, due to the higher inaccuracy caused by the increased number of tomographic pixels, as the differences in colour scale limits show. It can be seen how tomographic pixels placed at the corners of the pattern present higher residuals, in both cases, due to the reduced number of LOSs in those region. The $\mathrm{RMS_{rec.}}$ (Eq.3.1), as a function of the number of beamlets per pixel, in the 6 cases considered, is shown in Fig.3.9, where the beamlet width σ_g is set to 6.5 mm (optimal beamlet optics with $\delta = 7$ mrad) and 11 mm (non-ideal beamlet optics with $\delta = 20$ mrad). It is evident how the increase in resolution to 1 beamlet per pixel causes a huge spike in inaccuracy, resulting in $\mathrm{RMS_{rec.}} \sim 65\%$. For reduced resolutions of 5 beamlets or more, the reconstruction accuracy is around 90% (equivalently, $\mathrm{RMS_{rec.}} \sim 10\%$), which is an acceptable value and proves the possibility of studying the beam at 5-beamlet resolution with a 10% error. The error further decreases to reach 4% at 80-beamlet resolution. This behaviour is expected, as with an increasing number of tomographic pixels the number of variables increases as well, reducing the accuracy of the reconstruction. It can be noted that a difference in beamlet width does not affect the reconstruction accuracy, neither does the beam uniformity. Indeed, in Fig.3.9, on the left panel, no relevant distinction between the four cases studied (i.e. uniform and non-uniform beam with two different beam optics) can be noted, and it becomes distinguishable only on small scales, as shown in Fig.3.9 on the right panel. This is expected, since the performance of the algorithm should depend only on the reconstruction parameters (i.e. the tomographic pixel number) and not on the beam features. The reason for such increase in inaccuracy of the reconstruction from 5-beamlet resolution to 1-beamlet is due to the great increase in the number of variables, i.e. the number of tomographic pixels to reconstruct being 256 and 1280 respectively.
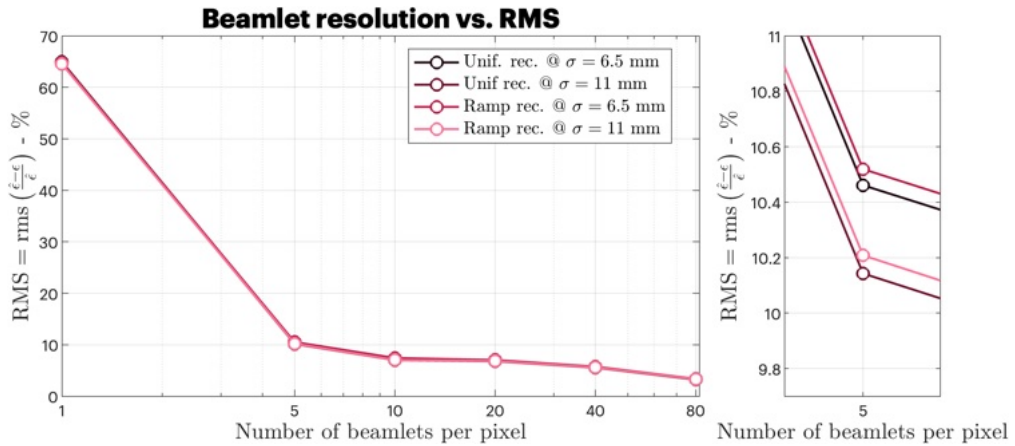

Figure 3.9: The effects of resolution on the reconstruction accuracy. Lighter colours show data relative to the non-uniform beam, while darker colours show data for the uniform beam. The error in the reconstruction lays around 10% with 5 to 80-beamlet resolution to then increase at 1 beamlet per tomographic pixel. This is expected: the number of variables increases with the number of tomographic pixels while the number of LOSs is fixed, thus worsening the reconstruction accuracy. No relevant effect due to beamlet optics or homogeneity can be noted and the curves can be distinguished only by closer inspection (right panel).

As the homogeneity of the beam is predetermined in the simulation, it is possible to assess the capability of the algorithm of capturing the uniformity of the beam, a fundamental parameter which must be assessed in order to comply to the 10% in-homogeneity requirement of ITER NBI. To this purpose, the $\Delta_{\text{rec.}}$ parameter is presented for the two resolution cases in Figs.3.8a/3.8b: the 5-beamlet resolution and the 1-beamlet resolution in the homogenous beam. These two cases are chosen since the former represents the highest resolution achievable maintaining a 10% error on the reconstruction, the latter offering the highest resolution, but with high inaccuracy. The $\Delta_{\text{rec.}}$ is also compared between the previous one-dimensional reconstruction algorithm (which represents a tested reference point) and the 2D LOS method in this work.

Since the beam is uniform, the expected value of the homogeneity is $\Delta_{\text{rec.}} \sim 0$. The results are shown in the following Tab.3.1:

Table 3.1: The uniformity quantifier $\Delta_{\text{rec.}}$ in the uniform beam case, whose expected value is 0. The comparison is carried between resolution (20, 10, 5 and 1 beamlet per pixel) and algorithm used (1D LOSs - prior version of the algorithm- and 2D LOSs - in this work).

		Resolution			
		20 beamlet/pix	10 beamlet/pix	5 beamlet/pix	1 beamlet/pix
LOS dim.	1D	$\Delta_{\text{rec.}} = 7.64\%$	$\Delta_{\text{rec.}} = 7.98\%$	$\Delta_{\text{rec.}} = 11.16\%$	$\Delta_{\text{rec.}} = 49.21\%$
	2D	$\Delta_{\text{rec.}} = 6.95\%$	$\Delta_{\text{rec.}} = 7.36\%$	$\Delta_{\text{rec.}} = 10.83\%$	$\Delta_{\text{rec.}} = 50.37\%$

It is evident how the two homogeneity estimates are similar between the 1D LOSs approach and the two-dimensional LOSs method. The reconstructions at higher resolution shows a worse estimate of the uniformity, changing from 10% in the 5-beamlet resolution case to 50% at 1-beamlet resolution. It is worth-noting that the 10% uniformity of the reconstruction at 5-beamlet per pixel resolution indicates that lower resolutions must be used: while the simulated beam is completely uniform (an optimal scenario during ITER NBI operation), this level of resolution indicates a reconstructed beam uniformity not compatible with the 10% in-homogeneity standard of ITER. In order to obtain a more reliable uniformity characterisation and better reconstruction accuracy, a 10-beamlet resolution may be employed. As pointed out, a compromise between spatial resolution and reconstruction reliability must be found. Different choices for the parameters, as shown, are available in order to find the optimal solution for different beam assessment needs.

3.4.3. Performance assessment varying background luminosity

Since a 5-beamlet resolution is the highest achievable while remaining around the 10% accuracy mark, it is chosen for the following scans. The second parameter scan involves the presence of light background inside the experiment. Here, the beamlets width is set to 6.5 mm (optimal beamlet optics), no Poissonian noise on the signals and the

background luminosity is increased from 0% (no background light) up to 20% of the maximum beamlet emissivity (extreme case, shown in Fig.3.12) for both homogeneity cases. The background is simulated by adding the to set of simulated beamlet Gaussians an additional one of equation

$$\text{Back.}(x, y) = A_{\text{Back.}} \times e^{-\frac{1}{2\sigma_{\text{Back.}}^2}(x^2+y^2)}$$

where $A_{\text{Back.}}$ is the background maximum amplitude (as percentage of the beamlet emissivity nominal amplitude), $\sigma_{\text{Back.},x} = \sigma_{\text{Back.},y} = \sigma_{\text{Back.}} = 600$ mm is the width of the background luminosity and is centred on the axis origin, i.e. the center of the SPIDER GG. The addition of background light can be seen in Fig.3.10, here modelled with 0.5% amplitude (similar to what observed in experimental data).
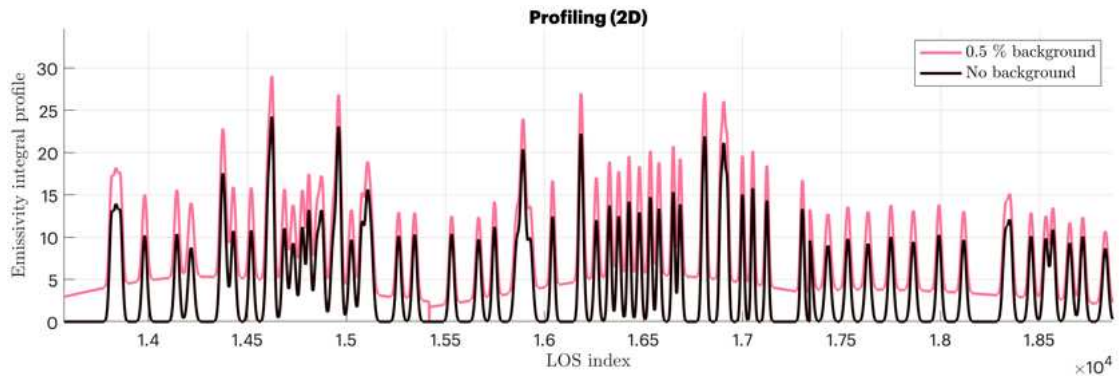

Figure 3.10: The effect of background addition to the integrals. In dark colour, the signal integrated without background, in pink, the signals integrated adding a 0.5% background, resulting similar to experimental data.
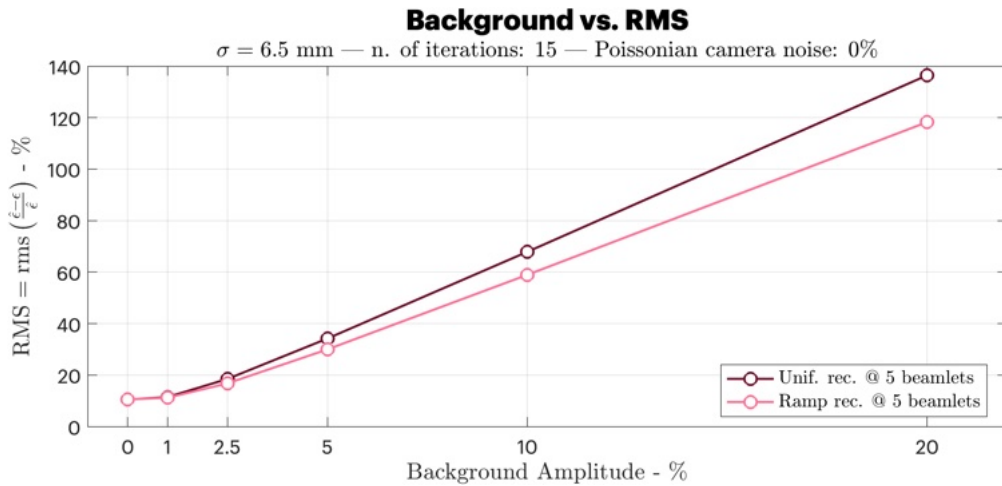

Figure 3.11: The effect of the background intensity (percentage of of the nominal beamlet intensity) over the RMS$_{\text{rec.}}$ of the reconstruction. The relation is roughly linear for both uniformities.

42

The RMS$_{\text{rec.}}$ scan results are shown in Fig.3.11. The graph shows a roughly linear dependence of the reconstruction accuracy on the light background amplitude, settling around 10% if the luminosity does not rise above 1% of the nominal emissivity of the beamlets. Already at 2.5% background the error rises to 20%, following the linear trend up to 20% background intensity where the error reaches 140% (in the homogenous case) and 120% (in the ramped emission case), representing an extreme scenario. This effect is expected and is partially due to the evaluation of the RMS$_{\text{rec.}}$, which heavily penalises the presence of a light background since it is not included in $\hat{\epsilon}$. However, the presence of stray light, which may have a different profile form the large gaussian emissivity introduced here, hazes the beamlet emissivity resulting in a less accurate reconstruction. This effect must be take into account as background luminosity is always present in the vessel, either due to beam plasma formation or simply the beam emissivity being reflected from the walls. To obtain the best performances of the reconstruction algorithm it is important to keep the background light to a minimum, as it represents one of the most impactful parameters, either by better blocking the light coming from the source, limiting the beam plasma formation and reducing vessel reflections. If, during full-beam operations (with all 1280 beamlets), the background light becomes too large due to the plasma between the beamlets, this shows that it must be taken into account. A possibility is to change the tomographic pixel geometry, adding pixels also in the region between the beamlets. Another solution could be the use of a H$_\alpha$ filter to select only the wanted line emission.
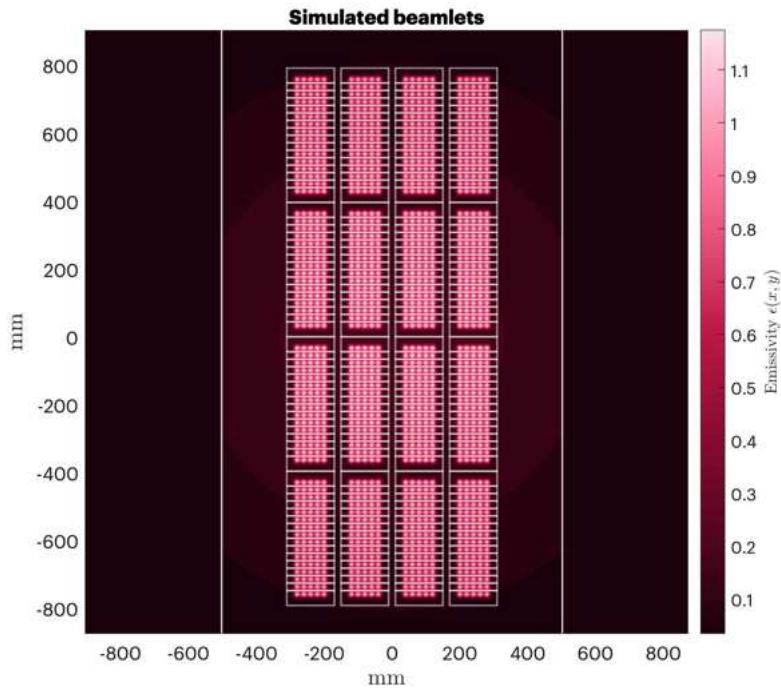

Figure 3.12: The simulated beam with 20% background luminosity added and shown as wide contours under the beamlets in the uniform case.

3.4.4. Performance assessment varying signal noise

The third scan involves the noise amplitude on the camera signals, with 5-beamlet resolution, $\sigma = 6.5$ mm and 0% background for both homogeneity cases. Each camera signal I is modified into I' by applying a random gaussian-distributed variable ξ with $\sigma = 1$ and mean $\mu = 0$:

$$I' = I(1 + A_{\mathrm{noise}} \times \xi)$$

where A_{noise} is the noise amplitude (in this work, ranging from 1% to 20%). In this way, the effect of the noise in the tomographic inversion is characterised. An example of profile of one camera at full beam with no background noise and $\sigma = 6.5$ mm is shown in Fig.3.13, where in dark is shown the profile without noise, in lighter colour the same profile but with noise added.
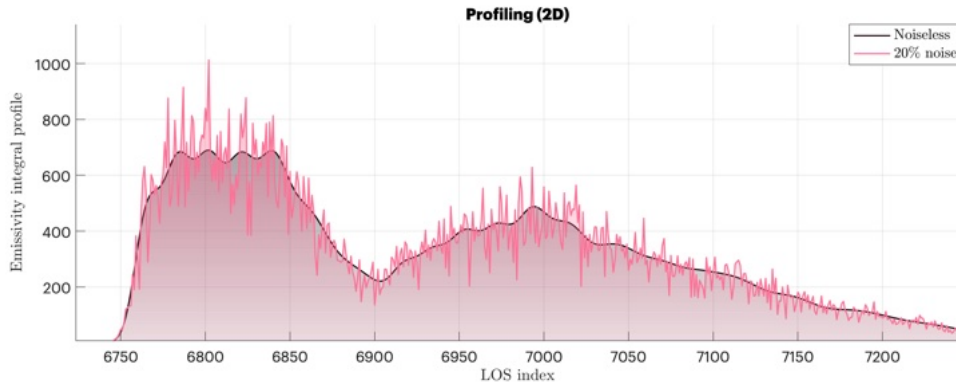

Figure 3.13: A zoom of the integrated signal with no background luminosity, $\sigma = 6.5$ mm and no noise (in dark colour) and 20% noise (in lighter colour).

The introduction of camera noise simulates the electronic noise of the sensor, but also the effect radiation affecting the cameras. From Fig.3.14, it is evident how the $\mathrm{RMS_{rec.}}$ increases roughly quadratically as the intensity of the noise increases, with similar values in the homogenous and ramped beamlet emissivity amplitudes, resulting consistently slightly higher in the latter case. This can be explained by noticing that, by construction, the ramping function Eq.3.3 reaches values 20% higher than the uniform beam with $A_g = 1$. As the noise added is proportional to the signal, the ramped emissivity case suffers an enhanced impact on the integrals. However, in the explored range, the camera noise has a less relevant impact on the reconstruction accuracy compared to the light background, ranging from 10.5% inaccuracy in the case of no noise up to 12% in the case of 20% noise. This suggests that the SART algorithm is quite stable in terms of errors on the source data, proving its reliability.
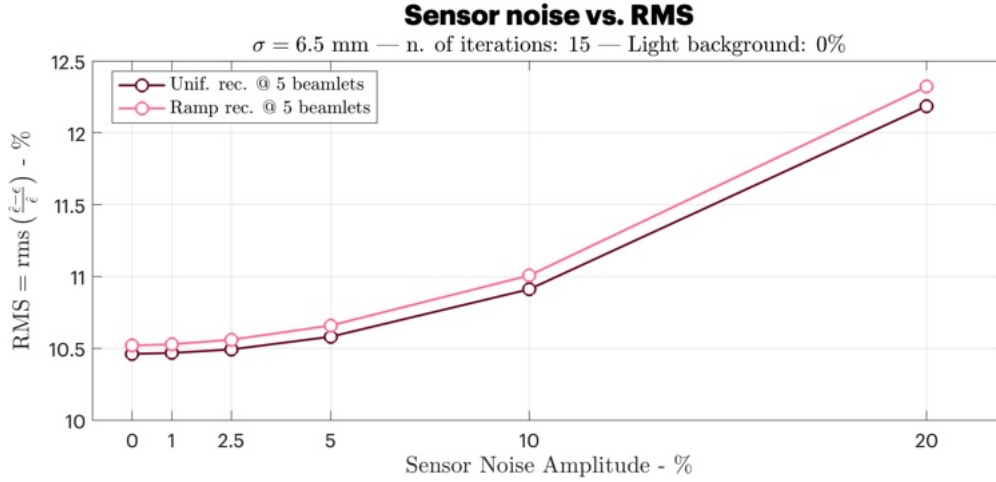
44

Figure 3.14: The effect of the signal noise, expressed as a percentage of the nominal value of the signal, on the reconstruction error. The relation is approximately quadratic for both homogeneity cases, being consistently slightly higher in the non-homogenous beam. This can be explained by the construction of the non-uniform case, which presents higher signals which are affected more heavily by the noise.

3.4.5. Real data performance

An application of the 2D LOS reconstruction on real experimental data is now presented and compared with the previous one-dimensional LOS approach. The shot considered is n. 9227, with caesium injection and 28 beamlets active (with tomography pixel size of 40×37.5 mm), with acceleration energy of 26 keV and 45 kW of RF power. Operating cameras are B2, B4 up to B14. The first data presented are the integral profiles of the beam emissivity, shown Fig.3.15: on the $\hat{x}$ axis the LOS index is reported following the camera order, while on the $\hat{y}$ axis the corresponding emissivity integral along the LOSs is reported. It represents the camera pixel count: several peaks can be observed corresponding to the beamlets, viewed from the different cameras as the LOS number scans across them. The integral values rarely drop to 0 and clearly display a light background between peaks. This is due to reflections inside the experiment. The same profiles reconstructed by the SART algorithm are plotted in red, respectively using the **a** matrix constructed using two-dimensional LOSs and one-dimensional LOSs. From the image, the capability of the algorithm of capturing the correct location of the peaks can be seen. However, the assignment of the correct value of the emissivity to each tomographic pixels can vary. In Fig.3.15, two camera integral sets can be seen side-to side: on the left, a high-magnification camera objective is used (visible by the increased width of the beamlet peak), on the right, a lower magnification is used (as the beamlets are narrower). At higher magnifications, the angle between two LOSs is wider, therefore, the impact of the LOS width introduced by the 2D LOSs is more severe and the estimated emissivity of the peaks is lower, as shown in the left part of the image where the 2D LOSs method underestimated the reconstructed signals with respect to the 1D LOS algorithm. However, when the magnification is lower, the 2D LOS method better captures the beamlet emissivity, while the previous version of the algorithm underestimates the emissivity more
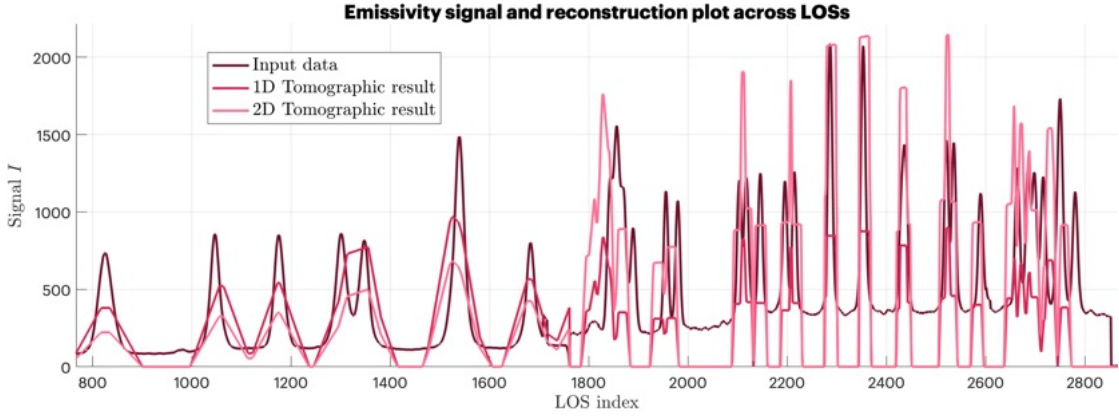
45

Figure 3.15: Integrated signals of the shot 9227 (a zoomed portion), in dark colour. 1D LOS reconstruction is shown in red, 2D LOS reconstruction in pink.

severely. This proves that, overall, the introduction of two-dimensional Lines-Of-Sight has brought improvements in the reconstruction capabilities of the algorithm, also with the experimental data.

In Fig.3.16 the final reconstruction of the shot 9227 is displayed in the 28-beamlet configuration using the one-dimensional LOS approach on the left and the 2D-LOS method on the right. The colour of each tomographic pixel is proportional to ϵ_i, the beamlets' emissivity. The two reconstructions are proportional, displaying a similar emissivity pattern across the 28 beamlets: the central region of the beam appears to be brighter compared to its top and bottom sections, in particular in the second beamlet column from the left. However, the emissivity scale is different, assigning higher emissivity values in the 2D case. Some beamlets in the central section appear to be relatively dimmed in the two-dimensional approach compared to the 1D method. The uniformity quantifier in this 2D LOSs reconstruction is

$$\Delta_{\text{rec.}} = 22.06\%$$

while, the case of the 1D reconstruction,

$$\Delta_{\text{rec.}} = 23.38\%$$

This proves that the 2D LOSs reconstruction algorithm is compatible with the previous 1D version in estimating the homogeneity of the beam in experimental scenarios. Notice how the 3 top-right pixels are reduced in size to avoid overlap due to their proximity.
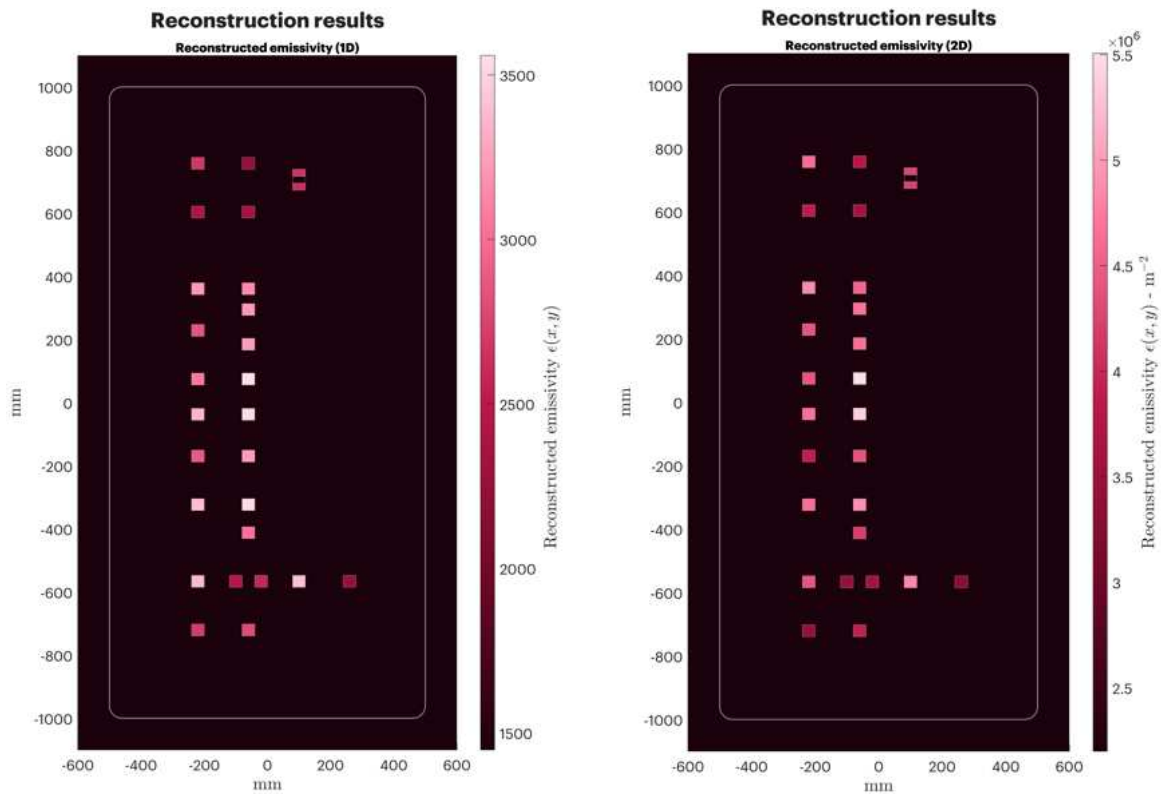
Figure 3.16: Reconstructions of the shot 9227 (blip 1), on the left using the 1D-LOS approach, on the right the 2D-LOS one. The emissivity reconstructed inside the tomographic pixels is roughly proportional between the two, but varies in magnitude, resulting in two estimates of beam uniformity, being 72% and 78% respectively.

47

4. *Beam current density*

In this chapter the study of the physics behind the emissivity is conducted in order to retrieve the beam current density from the tomographic reconstruction. This offers the advantage of characterising the beam current in a non-invasive way, which is a key feature for the future application of visible tomography to the ITER NBI prototype MITICA - and also when SPIDER will operate at full power. The model developed to interpret the beam emissivity is composed by two main parts: the first is the study of the beam composition and H_α light emission mechanism, which involves the interaction of the energetic H^- beam with the background molecular hydrogen gas as a function of the beam energy and background gas density. Due to multiple atomic processes, which will be discussed in Sec.4.1, the beam changes composition and a model for the beam ionic population fluxes is required. Moreover, the cross-sections responsible for the emission of the H_α light are considered, allowing to estimate the beam emissivity taking into account the contribution of all the species composing the beam, in the region observed by cameras. In the second part, an absolute calibration constant for the tomographic diagnostic is also estimated, allowing to relate the counts on the CMOS sensors to an absolute emissivity. With the help of the model, the reconstructed emissivity can be directly related to the negative ions density, and compared with the other experimental measurements of the beam current. To this purpose, an experimental setup is presented in Sec.4.2 in which the calibration constant is calculated using a calibrated source.

4.1. Reactions and modelling

In this section the beam particle composition along the beam path is modelled. The goal is to obtain the density of hydrogen atoms in the $n = 3$ excited state in the beam, which give rise to the H_α emission (resulting from the relaxation from $n = 3$ to $n = 2$ states) detected by the cameras, in order to estimate the beam current density from the emissivity obtained from the tomographic reconstruction. The approach is analogous to what already proposed in Ref.[41], including now more reactions which are deemed relevant according to Ref.[47], most importantly with the inclusion of secondary electrons - produced along the beam via interactions between beam particles and the background gas - to assess their contribution to the beam emissivity. The assumption made in this model is that all the light measured by visible cameras consists in H_α wavelength, since

49

it is the most intense line of the beam emission. The charge state of a negative ion beam evolves during the propagation due to the interaction with the background particles. The particle fluxes of different charges are described through a system of differential equations along the beam propagation direction - starting from the last accelerator grid in $z = 0$ - allowing exchange of particles between the species via reactions. The number of hydrogen atoms in $n = 3$ is estimated considering the main processes which excite the various species of the beam to the $n = 3$ levels, using as population the one obtained by the differential system at the position observed by cameras. Knowing the excited hydrogen population, one can estimate the H_α power emission rate - emissivity - and estimate the beam current. Indeed, assuming that the emissivity of the beam does not change relevantly along the beam axis z in the volume observed by each camera pixel, it is possible to relate the reconstructed emissivity to the beam current via:

$$\epsilon = (h\nu_{H_\alpha}) \cdot n_b n_{H_2} \sigma_{\text{eff}} v_b \frac{A_{32}}{A_{32} + A_{31}} \tag{4.1}$$

$$= (h\nu_{H_\alpha}) \cdot \Gamma_b n_{H_2} \sigma_{\text{eff}} \frac{A_{32}}{A_{32} + A_{31}} \tag{4.2}$$

$$= (h\nu_{H_\alpha}) \cdot \frac{j_b}{q} n_{H_2} \sigma_{\text{eff}} \frac{A_{32}}{A_{32} + A_{31}} \tag{4.3}$$

where $h\nu_{H_\alpha}$ is the photon energy of the H_α emission, j_b is the beam current, q is the electron charge and σ_{eff} is the effective cross-section, describing the probability of beam particles to become neutral hydrogen in the $n = 3$ state. n_b and n_{H_2} are the beam and the background molecular hydrogen density, the latter assumed to be at 300 K, thus effectively at rest with respect to the beam particles. In particular, for this work the background molecular hydrogen pressure is fixed at 20 mPa, resulting in $n_{H_2} = 4.83 \times 10^{18}$ m^{-3}. A_{31} and A_{32} are the Einstein coefficients and quantify the probability of the H_α transition of excited hydrogen atoms to de-excite in $n = 2$ form $n = 3$, while v_b is the beam speed, which is assumed to be non-relativistic since the energy range for SPIDER is below 100 kV. Notice that the beam density can be related to the beam total flux Γ_b via

$$\Gamma_b = \frac{n_b}{v_b}$$

The beam population includes neutral and ionised hydrogen - H^-, H^0, H^+ - and secondary electrons e^-, whose energy is assumed to be proportional to the beam energy $\mathscr{E}_b$ according to the relative mass

$$\mathscr{E}_e = \frac{m_e}{m_H} \mathscr{E}_b$$

Therefore, the electron speed is equal to the beam speed v_b. Since the number density of the beam n_b is

$$n_b = n_{H^-} + n_{H^0} + n_{H^+} + n_{e^-}$$

as all species travel to the same speed, this can be related to the total beam flux Γ_b

$$\Gamma_b = \Gamma_{H^-} + \Gamma_{H^0} + \Gamma_{H^+} + \Gamma_{e^-}$$

where Γ_{H^-}, Γ_{H^0}, Γ_{H^+} and Γ_{e^-} are the fluxes of each beam species considered in the model. σ_{eff}, the effective cross-section, is defined as:

$$\sigma_{\text{eff}} = \frac{1}{\Gamma_b} \left(\Gamma_{H^-} \sigma_{SS}^{(3)} + \Gamma_{H^0} \sigma_{CE}^{(3)} + \Gamma_{H^+} \left(\sigma_{SS}^{(3)} + \sigma_{E}^{(3)} + \sigma_{HDE}^{(3)} \right) + \Gamma_{e^-} \sigma_{eDE}^{(3)} + \right)$$

where the apex (nl) specifies that the cross-section of the process produces hydrogen in the nl excited state, while the subscript refers to the different processes involved, as described in Tab.4.1. Since we are interested in the Balmer series, the apex notation (3) indicates the cross section to the $n = 3$ state, which is obtained as a combination of cross-sections to the $(3l)$ excited substates as shown in Tab.4.2. The effective cross-section quantifies the amount of neutral hydrogen atoms which are in the $n = 3$ state. In Tab.4.1 all underlined reagents and products are fast particles belonging to the beam. In particular, fast products are assumed to have the same beam velocity and continue to propagate and interact with the beam particles and the background. Not underlined particles are, instead, no longer fast particles of the beam. In particular, Excitation, electron Dissociative Excitation and Hydrogen Dissociative Excitation reactions result in slow excited atoms and, in fact, are not included in the evolution of the beam species. It shall be noted that data for cross-sections, if available, are rarely complete in terms of energy range or final state. Therefore, in many processes the cross-section is either extended by extrapolation or, for total cross-sections, computed by summing partial cross sections of the process relative to single substates (e.g.: $n = 1, 2, 3, \dots$ and $l = 0, \dots, n-1$). More information on the data origin is available in table Tab.4.2, where data was taken from ALADDIN [48], an online database for atomic processes with relative source references. In this work, cross-section data are interpolated using polynomials in the range of interest for the SPIDER and MITICA beams, as shown in Fig.4.1. Note that for secondary electrons cross-sections - respectively, σ_{MT} and σ_{eDE} - they must be evaluated at the electron energy $\mathscr{E}_e$. In the particular case of Fig.4.1, the energy at which cross-sections are evaluated (indicated with a black line) is the nominal SPIDER beam energy of 100 keV, with relative electron energy resulting in 54 eV. The differential system of the evolution of each population along the beam can be written as:

$$\begin{cases} \dfrac{\partial \Gamma_{H^-}}{\partial z} = -\Gamma_{H^-} \left(\sigma_{SS} + \sigma_{DS} \right) \cdot n_{H_2} \\[2mm] \dfrac{\partial \Gamma_{H^0}}{\partial z} = \left[\Gamma_{H^-} \sigma_{SS} - \Gamma_{H^0} \sigma_I + \Gamma_{H^+} \sigma_{CE} \right] \cdot n_{H_2} \\[2mm] \dfrac{\partial \Gamma_{H^+}}{\partial z} = \left[\Gamma_{H^-} \sigma_{DS} + \Gamma_{H^0} \sigma_I - \Gamma_{H^+} \sigma_{CE} \right] \cdot n_{H_2} \\[2mm] \dfrac{\partial \Gamma_{e^-}}{\partial z} = \left[\Gamma_{H^-} \left(\sigma_{SS} + 2\sigma_{DS} \right) + \Gamma_{H^0} \sigma_I - \Gamma_{e^-} \sigma_{MT} \right] \cdot n_{H_2} \end{cases} \tag{4.4}$$

Assuming that only negative ions are exiting the accelerator, the initial conditions can be set as $\Gamma_{H^0}(0) = \Gamma_{H^+}(0) = \Gamma_{e^-}(0) = 0$. The output flux of negative ions from the accelerator is set to $\Gamma_{H^-}(0) = 1$. By definition, the effective cross section σ_{eff} is normalised to the total flux, hence its estimate is independent from the absolute value of the beam current, as expected since the beam current estimate from the emissivity in
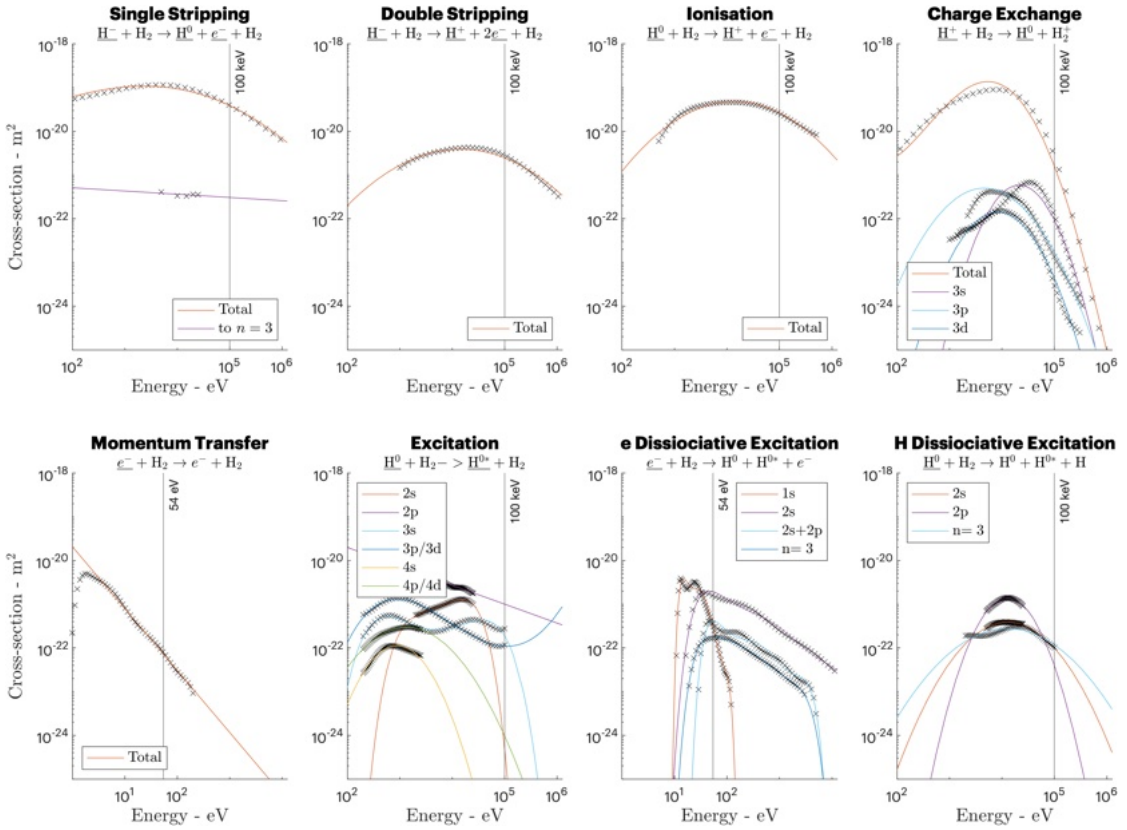
Figure 4.1: Cross-section data obtained from ALADDIN. Black crosses show experimental data, while the coloured lines are the polynomial interpolations. For reaction involving heavy beam particles - SS, DS, I, CE, E, HDE - the vertical line shows the beam energy where the cross-section is computed (at nominal SPIDER energy), while for reactions involving secondary electrons - MT and eDE - the vertical line shows the electron energy obtained as $\mathscr{E}_e = \frac{m_e}{m_H}\mathscr{E}_b$.

Eq.4.1 should not require an a-priori knowledge on the beam flux.

The solution of Eq.4.4 with a 100 keV of acceleration is reported in Fig.4.2 in the top panels. The fluxes of the different species are shown as a function of z, the distance from the grounded grid along the beam propagation direction. The negative ion flux swiftly decays exponentially, while the population of neutral hydrogen stabilises. Indeed, the first equation in the system 4.4 leads to a decaying exponential with characteristic length $\lambda_{H^-} = ((\sigma_{SS} + \sigma_{DS}) \cdot n_{H_2})^{-1}$. The population of secondary electrons, instead, quickly increases as σ_{MT} - which describes elastic scattering where electrons loose momentum, thus they do not partecipate in beam reactions anymore - is comparatively small with respect to other processes which generate electrons, as single stripping. The population of positive ions instead slowly increases. In the bottom panels of Fig.4.2 the same study is carried out in the case of MITICA 1 MeV acceleration energy. Here, the reduction of H^- ions is much slower, while the other species increase in number much more slowly. This is due to the decrease of the Single Stripping and Double Stripping cross-sections

Table 4.1: Reactions included in the model. Some reactions are included in the differential equations for the populations - SS, DS, CE, I, MT - others are involved in the computation of the H_α population via the effective cross section σ_{eff} - SS, CE, E, eDE, HDE. The underlined terms in the reaction highlight the fast beam species. Once the projectile particle reacts, it is still included in the model if its speed does not change relevantly, thus producing an underlined term in the right-hand side of the reaction. If the particle after the reaction is slower than the beam, it is considered lost.

Process name	Symbol	Process
Single stripping	σ_{SS}	$\underline{\text{H}^-} + \text{H}_2 \rightarrow \text{H}^0 + \underline{e^-} + \text{H}_2$
Double stripping	σ_{DS}	$\underline{\text{H}^-} + \text{H}_2 \rightarrow \text{H}^+ + 2\underline{e^-} + \text{H}_2$
Ionisation	σ_{I}	$\underline{\text{H}^0} + \text{H}_2 \rightarrow \underline{\text{H}^+} + \underline{e^-} + \text{H}_2$
Charge exchange	σ_{CE}	$\underline{\text{H}^+} + \text{H}_2 \rightarrow \underline{\text{H}^0} + \text{H}_2^+$
Momentum transfer	σ_{MT}	$\underline{e^-} + \text{H}_2 \rightarrow e^- + \text{H}_2$
Excitation	σ_{E}	$\underline{\text{H}^0} + \text{H}_2 \rightarrow \text{H}^{0*} + \text{H}_2$
Electron dissociative excitation	σ_{eDE}	$\underline{e^-} + \text{H}_2 \rightarrow e^- + \text{H}^0 + \text{H}^{0*}$
Hydrogen dissociative excitation	σ_{HDE}	$\underline{\text{H}^0} + \text{H}_2 \rightarrow \text{H}^0 + \text{H}^0 + \text{H}^{0*}$

at this energy (see Fig.4.1), the two depletion terms in the beam model for the negative ions. Once estimated the beam composition along the beam propagation direction, it is possible to estimate the H_α emission at the position observed by cameras, considering all the assumptions made. To do so, the fluxes of the various species composing the beam at $z = 0.35$ m are considered to estimate the probability they excite at the level $n = 3$, using the reactions described in Tab.4.1, involving as a final state an excited neutral atoms. The assumption that all the atoms excited at this position will also de-excite at the same location is made. This is a well posed assumption since, at the energy at which SPIDER operated until now, the path traveled by the ions is of few centimetres, and it can be assumed that the beam is stationary within that distance (see Fig.4.2). Therefore, it is possible to separate each ionic species' contribution to the $n = 3$ excited hydrogen population by defining partial effective sigma contributions:

$$\sigma_{\text{H}^-,\text{eff}} = \frac{\Gamma_{\text{H}^-}(z)\sigma_{\text{SS}}^{(3)}(\mathscr{E}_b)}{\Gamma_b(z)} \qquad \sigma_{\text{H}^+,\text{eff}} = \frac{\Gamma_{\text{H}^+}(z)\sigma_{\text{CE}}^{(3)}(\mathscr{E}_b)}{\Gamma_b(z)}$$

$$\sigma_{\text{H}^0,\text{eff}} = \frac{\Gamma_{\text{H}^0}(z)\left((\sigma_{\text{CE}}^{(3)}(\mathscr{E}_b) + \sigma_{\text{HDE}}^{(3)}(\mathscr{E}_b))\right)}{\Gamma_b(z)} \qquad \sigma_{e^-,\text{eff}} = \frac{\Gamma_{e^-}(z)\sigma_{\text{eDE}}^{(3)}(\mathscr{E}_{e^-})}{\Gamma_b(z)}$$

The relative contribution with respect to the total effective sigma, defined as

$$\sigma_{\text{eff}} = \sum_i \sigma_{i,\text{eff}}$$

of each partial effective sigma reported in Fig.4.3 as a function of the beam energy at $z = 0.35$ m along the beam axis. The main contribution to the effective cross-section

Table 4.2: Cross-section data. It can be seen that the available cross sections vary in end state. For some of them, data for each substate (nl) are available while, for others, cumulative cross sections are available, either involving the whole $n = 3$ excited state or substates, as the notation $(np + nd)$ indicates. Cross-sections with no apex are intended as the total cross-section of the process. The (all) notation indicates the same data source for all available cross section of the reaction.

Process	Available cross-sections	Derived cross-sections	Source
SS	$\sigma_{\mathrm{SS}}, \sigma_{\mathrm{SS}}^{(3)}$		[49][50]
DS	σ_{DS}		[49]
I	σ_{I}		[49]
CE	$\sigma_{\mathrm{CE}}, \sigma_{\mathrm{CE}}^{(3s)}, \sigma_{\mathrm{CE}}^{(3p)}, \sigma_{\mathrm{CE}}^{(3d)}$	$\sigma_{\mathrm{CE}}^{(3)} = \sigma_{\mathrm{CE}}^{(3s)} + \sigma_{\mathrm{CE}}^{(3p)} + \sigma_{\mathrm{CE}}^{(3s)}$	[49] (all)
MT	σ_{MT}		[51]
E	$\sigma_{\mathrm{E}}^{(2s)}, \sigma_{\mathrm{E}}^{(2p)}, \sigma_{\mathrm{E}}^{(3s)},$ $\sigma_{\mathrm{E}}^{(3p+3d)}, \sigma_{\mathrm{E}}^{(4s)}, \sigma_{\mathrm{E}}^{(4p+4d)}$	$\sigma_{\mathrm{E}} = \sum_i \sigma_{\mathrm{E}}^{(i)}$ $\sigma_{\mathrm{E}}^{(3)} = \sigma_{\mathrm{E}}^{(3s)} + \sigma_{\mathrm{E}}^{(3p+3d)}$	[49] (all)
eDE	$\sigma_{\mathrm{eDE}}^{(1s)}, \sigma_{\mathrm{eDE}}^{(2s)}, \sigma_{\mathrm{eDE}}^{(2p)}, \sigma_{\mathrm{eDE}}^{(3)}$	$\sigma_{\mathrm{eDE}} = \sum_i \sigma_{\mathrm{eDE}}^{(i)}$	[51] (all)
HDE	$\sigma_{\mathrm{HDE}}^{(2s)}, \sigma_{\mathrm{HDE}}^{(2p)}, \sigma_{\mathrm{HDE}}^{(3)}$	$\sigma_{\mathrm{HDE}} = \sum_i \sigma_{\mathrm{HDE}}^{(i)}$	[49] (all)

from the H_α emission comes from the single stripping, which is expected as its cross-section represents the dominant process. At nominal acceleration power in SPIDER (100 keV), the single stripping process accounts for the 87.7% of the emissivity, followed by excitation (5.7%), electron dissociative excitation (4.1%) and hydrogen dissociative excitation (2.2%). Since σ_{eff} is evaluated at the beam energy, cross-sections for electrons, as MT or eDE, are evaluated at the electron energy according to the mass proportionality with respect to the beam.

Having an estimate for the total effective cross-section, the emissivity of the beam at different energies can be evaluated. The result of this energy scan at the position of the cameras is shown in Fig.4.4. It is evident that the beam emissivity decreases as beam energy is raised. This can be directly linked to the reduction of the cross-sections, responsible of the production of ions in the level $n = 3$ included in the model, as energy increases. The choice of the initial flux value $\Gamma_{\mathrm{H}^-}(0) = 1$ as a normalised quantity allows to interpret the emissivity as the amount of radiant energy present at the camera location per unit of flux. Therefore, the emissivity is expressed in terms of energy (J) instead of power (W) as the rate of production is proportional to the absolute value of the flux at this location.

It is worth noting that secondary electrons contribute to the beam emissivity at the nominal beam energy (around 4%). Although they have a much lower impact than Single Stripping processes, involving H^- ions, their presence cannot be neglected, most relevantly because of their mobility compared to other heavier ionic species. As discussed in Ref.[47], secondary electrons represent a contribution to the beam plasma and, conse-
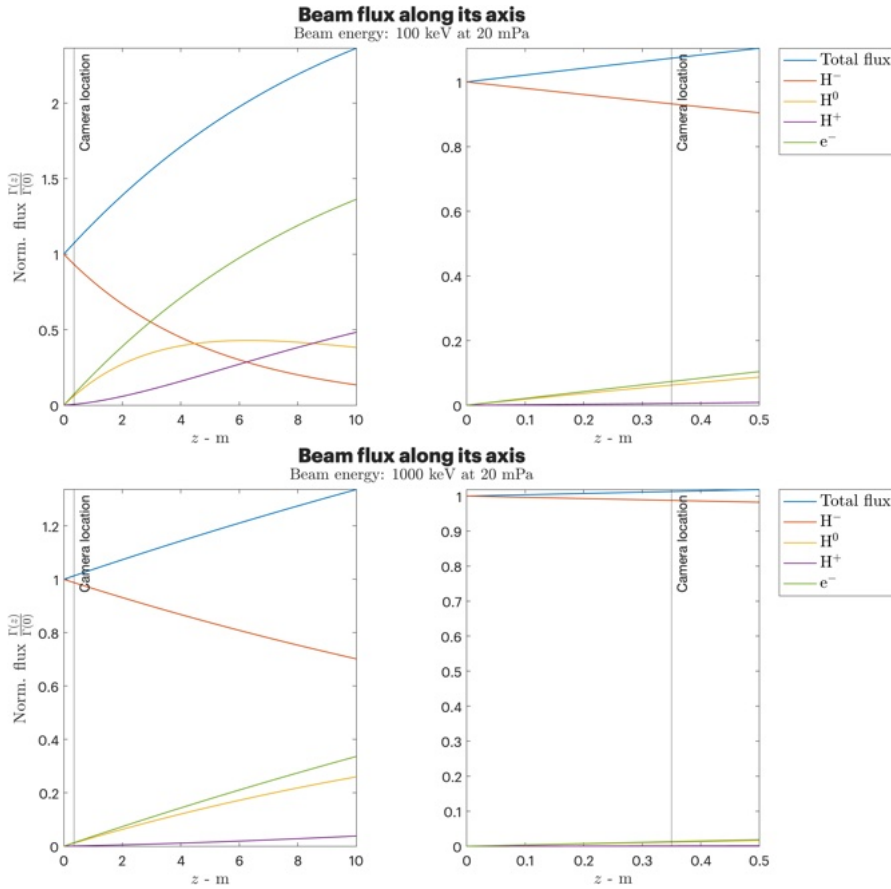
Figure 4.2: Different population fluxes in the beam as a function of distance with beam energy at 100 keV (top panel) and 1 MeV (bottom panel). In the top-left graph, it is possible to notice the quick decay of negative ions (orange) and a predominant increase in secondary electrons (green). Populations of positive (violet) and neutral (yellow) hydrogen instead tend to change slowly. On the top-right, the same plot but zoomed in the region of the tomographic diagnostic. The analogous case at 1 MeV is shown in the bottom-left graph. It is clear that the the negative ions' population decreases much more slowly.

quently, they may play a role in the light background observed between the beamlets. In this model, all the secondary electrons produced at the position observed by the cameras interact with the background gas. This is an overestimate of the contribution of the e^- to the beam current density since, due to their negative charge and lower mass, they diffuse all around the beam itself. However, this model shows that they contribute in a minimal part to the beam light, thus allowing to estimate, in first approximation, the beamlet current density without the need of more complex modelling of their dynamics. More complex models will be developed to study their contribute to the background light in between the beamlets, also considering other processes responsible of the generation of secondary electrons.
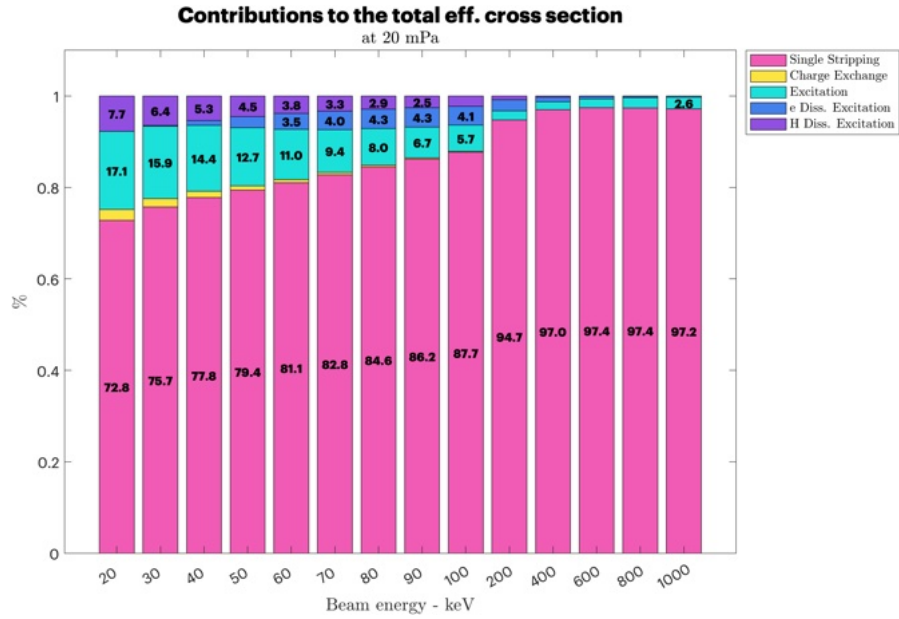
Contributions to the total eff. cross section
at 20 mPa

Figure 4.3: Relative contributions to the effective cross-section σ_{eff} for the H_α emission as a function of the beam energy. At the nominal SPIDER energy (100 keV), the majority of the emissivity is due to the single stripping (87.7%), followed by excitation (5.7%), electron dissociative excitation (4.1%) and hydrogen dissociative excitation (2.2%). The charge exchange contribution is negligible.
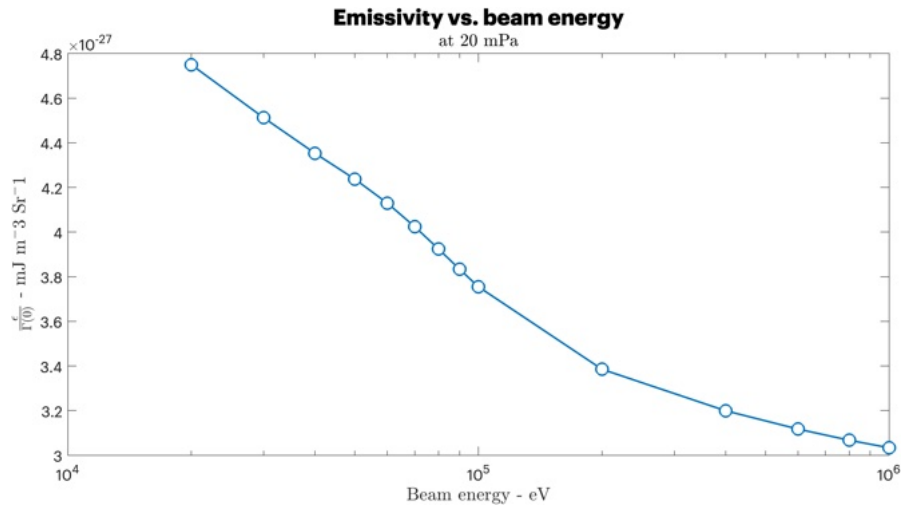
Emissivity vs. beam energy
at 20 mPa

Figure 4.4: Emissivity of the beam as a function of the beam energy at the camera location $z = 0.35$ m. The emissivity decreases as the beam energy increases.

4.2. Camera calibration: overview

In this section the procedure carried out to absolutely calibrate the cameras is described. To quantitatively estimate the radiant power deposited on one camera by the H_α emission

(or, equivalently, the number of H_α photons collected) an absolute calibration is necessary. Indeed, experimental data are a digital signal, i.e. counts encoded in an image. Although this provides comparative information, a calibration constant must be found, which allows to switch from counts to the physical H_α emissivity. For this reason, experimental setup (see Figs.4.5/4.7) has been prepared using a calibrated sphere, a light source whose spectral emissivity is known, of which a brief overview is provided and more details can be found in the following section.

Since the SPIDER emissivity is dominated by the H_α emission, the first goal is to isolate the H_α portion of the source light. To this purpose, an interferential filter for the H_α emission line is used. Since absolute measurements are needed, it has been calibrated to characterise its transmission coefficient. In the first experimental setup, the filter calibration is obtained by comparing the source spectrum H_α portion, with and without the filter, using a spectrometer. Since the transmission curve of the filter depends on the incidence angle of the light, it is not possible to simply put the filter in front of the calibrated lamp and measure the emission. Thus, an optical fiber in front of the calibrated sphere is used to carry the light to a lens. Adjusting the distance between the fiber and the lens, after the former the light is parallel and the filter can be placed after it. A second lens focuses the filtered light into a second optical fiber, which carries the light into a spectrometer. The count ratio between the filtered and unfiltered H_α portion of the source spectrum allows to estimate the transmission factor of the filter, F. With this calibration, a calibrated source of H_α light has been obtained, and can be used to calibrate the camera which, instead, measures the entire visible spectrum. The second experimental setup is prepared and the camera is set in parallel light after the filter and used to acquire some images at known exposure. Knowing the transmission factor of the filter and the light absorption by the surfaces of the lens, it is possible to relate the count of the most illuminated camera pixels to the source emissivity via direct proportionality using a calibration constant. The detailed list of tools (see Fig.4.6) used for the experimental setup is reported below and its execution is detailed in the following sections:

- two optic fibers with $\varnothing = 2$ mm, one for bringing the source light to the apparatus and one to transmit the light to the spectrometer;

- one aspheric lens with $\varnothing = 25$ mm and $f = 32$ mm (focal length), used to set the parallel light;

- one interferential filter with $\varnothing = 50$ mm and nominal wavelength $\lambda_0 = 657.55$ nm (H_α wavelength) (Medway optics), used to simulate an H_α source using the calibrated sphere light;

- one doublet with $\varnothing = 50$ mm and $f = 60$ mm ($f = 120$ on each lens), used to focus the filtered light onto the spectrometer's optic fiber;

- a mini spectrometer (Hamamatsu);

- a Basler camera (n.14) from the SPIDER tomography diagnostic;

57

- an absolute sphere with $\varnothing = 50$ mm opening;

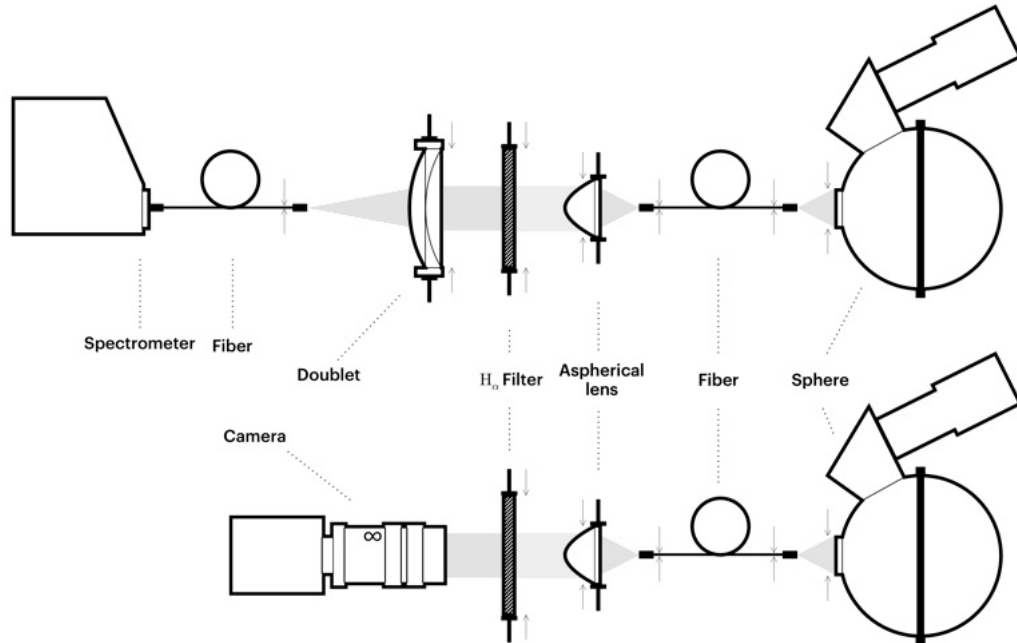- control software for sphere operation, camera and spectrometer data acquisition.

Figure 4.5: The two steps of the experiment. The top figure shows the setup with the spectrometer, the bottom figure shows the setup with the camera. In both figures, the filter is shown.
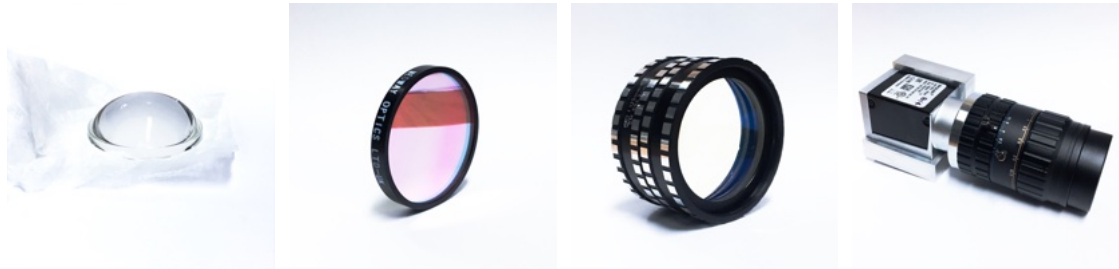

Figure 4.6: Four components of the experiment. From the left: the aspherical lens, the filter, the doublet and the Basler camera n.14.

4.2.1. Filter calibration

The filter is used to produce an equivalent H_α calibrated source, which represents the dominant emission recorded by tomography cameras.

As a first step, the filter transmission factor F is obtained. One extremity of the optical fiber is placed in front of the sphere aperture. The other end is placed in front of the
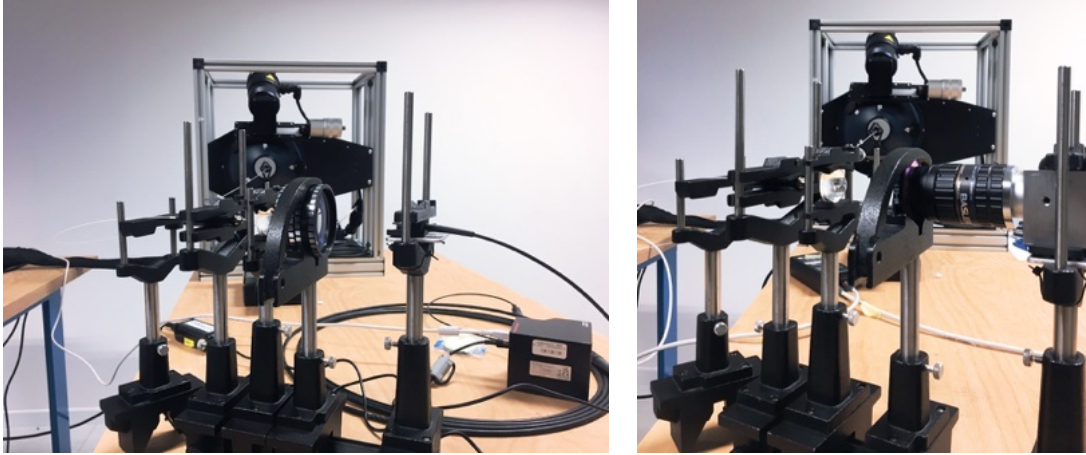
Figure 4.7: Two photos of the experimental setup. On the right, with the use of the spectroscope, on the left, with the use of the camera. On the background, one can see the sphere aperture with the fiber extremity in front of it. On the foreground, on the left, the other extremity of the fiber can be seen, followed by the aspherical lens with supports, the filter and the doublet with the fiber leading to the spectrometer (left) or the camera (right).

aspherical lens, which sets the light in parallel light condition. Then, light is collected by another fiber using the combined lenses, which is connected to the spectrometer. A full-light spectrum is acquired for 30 ms. The filter is placed between the aspherical lens and the doublet in the parallel light and a second spectrum is acquired for 60 ms (see the top panel of Fig.4.5). The background is removed from each spectrum (matching the acquisition time) and the resulting data are normalised to the acquisition time. As one can see in Fig.4.8 the full-light spectrum presents a black body tail towards higher wavelengths.

The peak of the filtered spectrum is integrated to obtain the H_α counts, $N_{H_\alpha, \text{filt.}}$, that are allowed to pass through the filter. Then, the peak is normalised to its maximum and multiplied with the full-light spectrum, in order to obtain its H_α component. This new spectrum peaked around λ_0 is integrated to obtain the H_α counts coming from the unfiltered source, $N_{H_\alpha, \text{full light}}$. One can thus define the filter transmission factor F as

$$F = \frac{N_{H_\alpha, \text{filt.}}}{N_{H_\alpha, \text{full light}}} = 0.69$$

F quantifies the percentage of H_α photons which are able to pass the filter. Note that also the lenses present an attenuation factor and are assumed to allow 98% of the light to pass. In this way a calibrated source of H_α has been obtained, and this source is used for the absolute calibration of the camera.

4.2.2. Camera calibration

The calibration is operated on the Basler camera n.14, as relative calibration constants among all SPIDER cameras are already available. The spectrometer is removed together with the combined lenses and the camera is aligned to the parallel light. The focal length
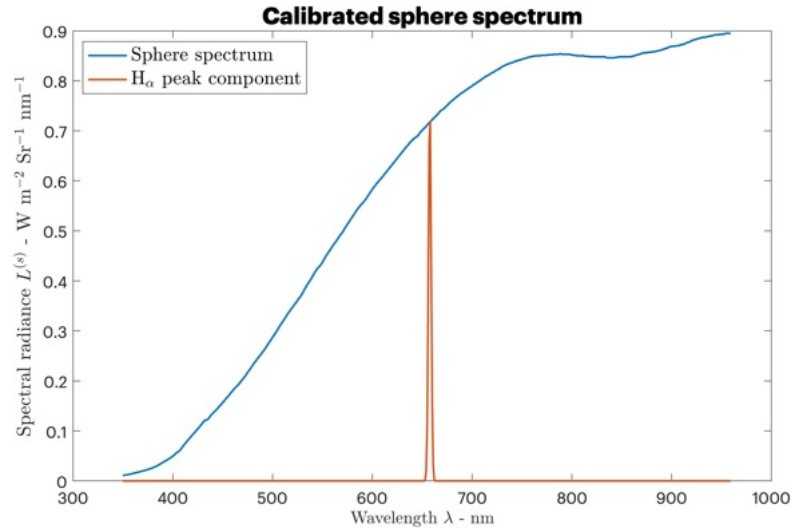
Figure 4.8: The calibrated sphere spectral radiance (in blue) and its H_α component (red) isolated multiplying the spectrum by the normalised peak of the filter spectrum, measured by the spectrometer.

of the lenses of the camera is set to infinity. In this way, the light entering the camera is focused on the sensor with the same image as the fiber exit. The filter is set between the camera lenses and the aspherical lens in order to obtain only the H_α portion of the spectrum (see bottom panel of Fig.4.5). The camera is used to acquire some pictures at exposure times short enough so the maximum counts in the images is much lower than the saturation value. Lastly, the source is switched off and the camera is allowed to
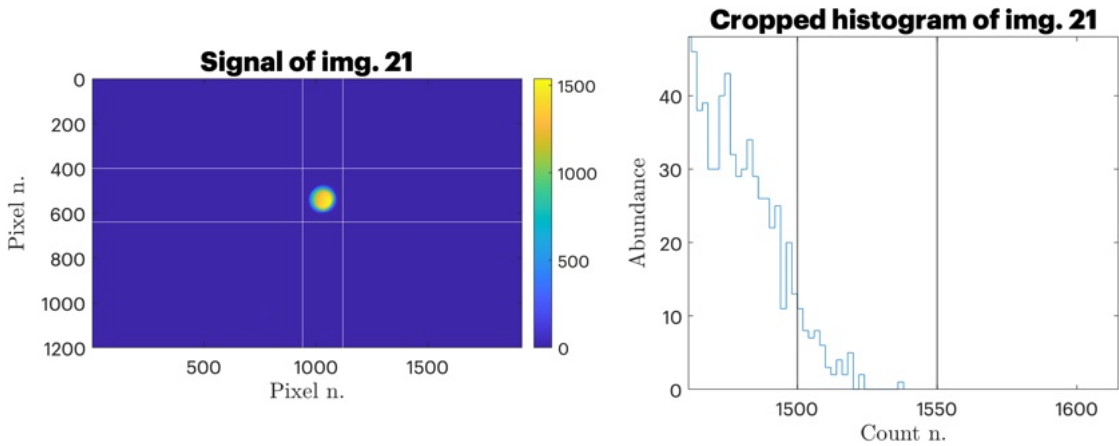

Figure 4.9: On the right, an example of camera image displaying the luminosity values (counts) in colour scale. On the right, the same image's histogram, focused on its high-count portion. The vertical black lines on the histogram define the count windows of the selected pixels for the evaluation of μ_c.

sample the background for the same acquisition times for consistency. The background is removed from the pictures, which are then normalised in exposure time, shown in

Fig.4.9. Each picture can be intended as a matrix of camera pixel counts which are linearly proportional to the emissivity illuminating the CMOS sensor.

The source spectral radiance $L^{(s)}(\lambda)$ is known and is measured in mW m^{-2} Sr^{-1} nm^{-1}. It quantifies the power flux per surface unit, per solid angle, per wavelength. One can multiply the source spectrum by the normalised filter light peak $f(\lambda, \lambda_0)$ (obtained with the spectrometer) to select the H$_\alpha$ component of the source spectrum: this is defined as the source H$_\alpha$ radiance

$$L(\lambda_0) = \int_0^\infty L^{(s)}(\lambda) f(\lambda, \lambda_0) \, d\lambda \qquad \text{mW m}^{-2} \text{ Sr}^{-1}$$

This quantity is carried by the fiber to the experimental apparatus, where it is reduced by the two surfaces of the aspherical lens and by the suppression factor of the filter, which reduces the intensity of the radiation under the filter peak and rejects all other wavelengths. Therefore, after the filter, the radiance entering the camera and reaching the detectors is:

$$L_d(\lambda_0) = (0.98)^2 F \, L(\lambda_0)$$

The counts C_d recorded by each camera pixel in the image are proportional to $L_d(\lambda_0)$ and to the exposure time τ, therefore the calibration factor of the camera μ_c is defined as:

$$\mu_c = \frac{C_d}{\tau L_d(\lambda_0)} = 1.4601 \times 10^5 \qquad \text{W}^{-1} \text{ s}^{-1}$$

Note that this parameter accounts for reduction by the lenses of the camera. As the sensors cover a fixed angle of view, the dependence on the direction and surface can be neglected.
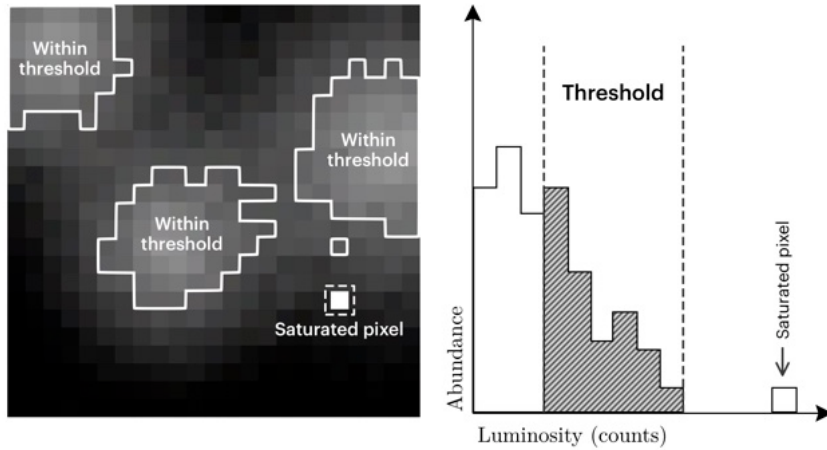

Figure 4.10: The principle of thresholding for pixel selection. Low luminosity pixels, at lower values in the histogram, are discarded. Also saturated pixels are not counted as they lie above the threshold.

To obtain the calibration constant, a value histogram (shown in Fig.4.9) is analysed, showing the number of pixel for any given count number in the image. This allows to select only image pixels with high values of luminosity (i.e. with high counts, thus appearing at the upper limit of the histogram, see Fig.4.10), setting a threshold between 1500 and 1550 counts (indicated with the two black lines) and obtaining several values for C_d. Notice that in this way no saturated pixels are counted (which may be present due to sensor noise) as they would appear at much higher counts. A value of μ_c is computed for each selected pixel and averaged over all of them. The final value is the average obtained from four pictures.

4.3. Experimental beam current estimate

Obtaining the calibration constant allows to convert the counts of camera integrals I_j to a radiant power measurement. For the sake of clarity, now the camera integral expressed in counts (or arbitrary units) will be labelled $I_j \rightarrow I_j^{\text{counts}}$, while the symbol I_j is used for calibrated camera integrals, expressed in W s:

$$I_j = \frac{I_j^{\text{counts}}}{\mu_c}$$

The now calibrated integrals can be used for the tomographic reconstruction, which now results in a physically meaningful reconstructed emissivity ϵ_i, shown in Fig.4.11 as example in shot n. 9227. These data were taken with 4×45 kW of radio-frequency power, 0.36 Pa of source pressure, hydrogen operation with caesium evaporation; the extraction and acceleration voltages are increased together by keeping constant their ratio $R = 9.5$. Calibrated emissivity values are in the order of few mW s m^{-2}. The emissivity is used to estimate each beamlet current density j_i using equation 4.3 at know beam energy $\mathscr{E}$ and background gas density n_{H_2}:

$$j_i = \frac{\epsilon_i}{h\nu_{\text{H}_\alpha}} \frac{q}{n_{\text{H}_2}\sigma_{\text{eff}}(\mathscr{E})} \frac{A_{32} + A_{31}}{A_{32}} \qquad (4.5)$$

The beamlets of apertures 8, 9 and 10 (highlighted in Fig.4.11) are chosen for beamlet current density estimation as their averaged beam current density measurements are available from the STRIKE calorimeter (electrical readings). Moreover, the value of the beam current density of beamlet 10 is available for shot n. 9227 from the Beam Current Monitor (BCM) [52]. In particular, electrical measurements of the total current of the beamlets impinging in each tile composing STRIKE are available, and can be used to compare the averaged current density estimated by the visible tomography for the same beamlets. Results for shot n. 9227 are shown in Fig.4.12 as a function of the beam energy: on the left, the reconstructed emissivity of beamlets 8, 9 and 10 is shown in terms of the number of H$_\alpha$ photons per squared meter (in orange colour). In blue, the reconstructed current density is plotted considering the background gas nominal pressure reading of 25 mPa. For beamlet 10, the individual current density value is known from BCM and plotted using the $\times$ symbol. On the right, the average current density of the
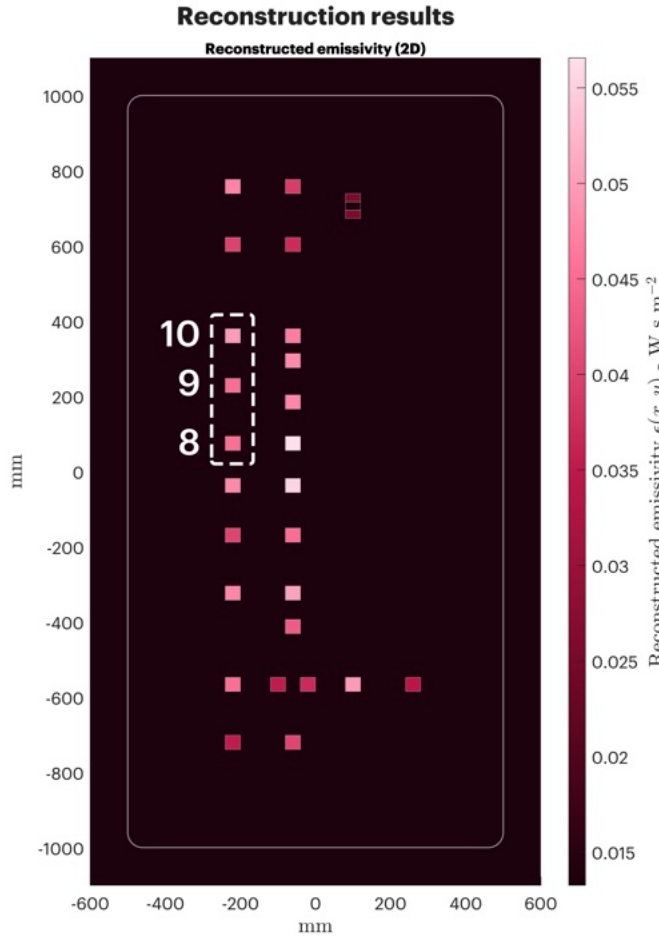
Figure 4.11: Reconstruction of shot n. 9227 using calibrated signals. The highlighted beamlets 8,9 and 10 are used for the beam current density estimate as their values are available from the STRIKE calorimeter and the BCM. In this pulse, the extraction and acceleration voltage are increased together, by keeping constant their ratio $R = \frac{U_{\text{acc.}}}{U_{\text{extr.}}} = 9.5$.

three beamlets, obtained with tomography (in orange) is compared with the equivalent STRIKE reading (in blue). As the beam energy (and thus the extraction voltage) is increased, the emissivity of the reconstructed beamlet increases as well. This is the same measured by the electrical current measurements of the BCM (on the left) and STRIKE (on the right), thus confirming that the emissivity is a good estimate of the beamlet current density. A similar result is obtained in Fig.4.13 for shot n. 8639 at the nominal pressure of 30 mPa. These data refer to 4×100 kW of radio frequency power, hydrogen operation without caesium evaporation; this explains the different beamlet current density obtained. During this shot the extraction voltage was kept constant and only the acceleration voltage is varied to study the effect on the beam current of the modification of only the beam energy. On the left, the beamlet (8, 9 and 10) current density estimate from tomography is shown in blue, while the emissivity value is shown in orange. On the right, the average beam density for the three beamlets is plotted,
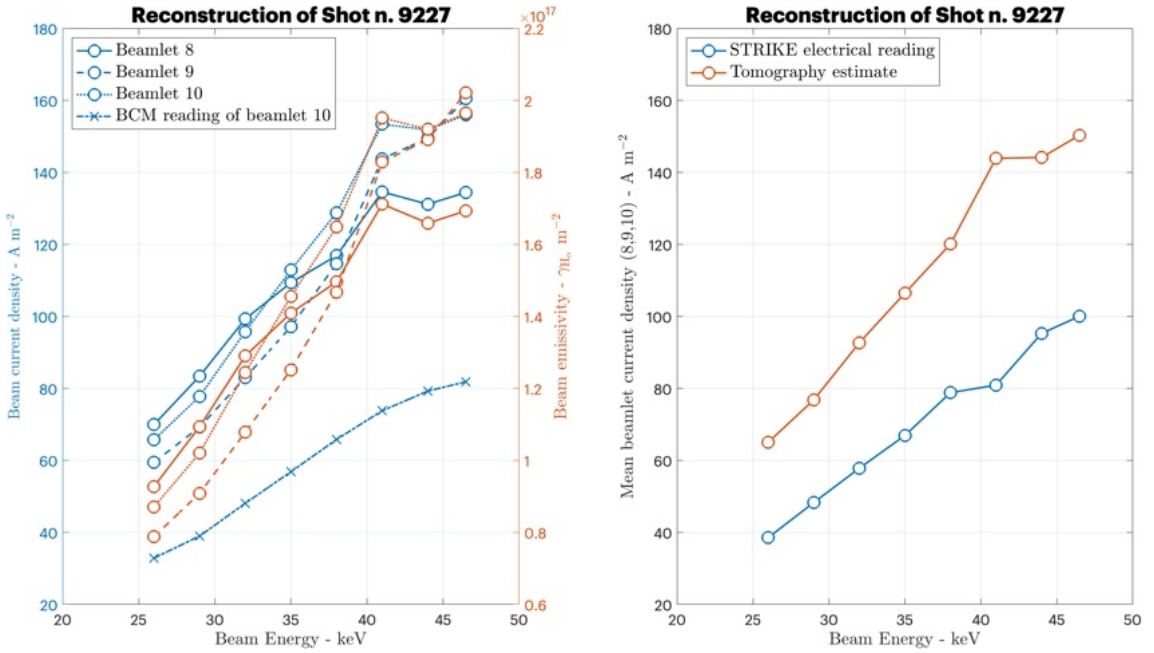
Figure 4.12: On the left, the estimate of emissivity (orange) and current density (blue) of beamlets 8, 9 and 10 during shot n. 9227 (in this pulse, the extraction and acceleration voltage are increased together, by keeping constant their ratio $R = \frac{U_{\text{acc.}}}{U_{\text{extr.}}} = 9.5$). On the right the averaged value of the current density of the 3 beamlets from tomography (orange) and from the STRIKE calorimeter (blue). For beamlet 10, the BCM current readings are shown with $\times$ markers. As the beam energy is increased, the beam emissivity and the beam current, obtained with tomography, increase as well, as shown on the left. On the same graph, the BCM current readings of beamlet 10 match the trend of its reconstructed current density. On the right, the averaged current values of the three beamlets follow the same trend of the equivalent STRIKE electrical readings and are in the same order of magnitude.

in blue as measured by STRIKE, in orange as reconstructed from tomography. The right panel shows how the emissivity decreases with increasing acceleration energy at constant extraction voltage (in orange). The computation of σ_{eff} compensates for this effects resulting in a constant beam current estimate across the energy range. On the right, the average of the reconstructed beamlet current density trend (of beamlets 8, 9 and 10) is matched by the electrical measurements of STRIKE.

It can be observed that the tomographic reconstruction of the beam current is of the same order of magnitude of the experimental readings from STRIKE and the BCM (in the case of beamlet 10 in Fig.4.12). This is a promising result and proves the possibility of employing visible tomography as a beam current diagnostic, with the advantage of not interfering with the beam itself. The plots show that the tomographic current estimate is systematically higher than the current readings, by 159% in the case of shot n. 9227 and by 227% in the case of shot n. 8639. This may be due to the light background recorded by the cameras, which causes an offset in the estimate of the beam current. The aforementioned further assessment of the dynamic of secondary electrons may help to explain the background emission. It must be also stressed that visible cameras collect the signal from all wavelengths, thus the installation of interferential H_α filters could help to further reduce the background and improve the beam current density estimate.
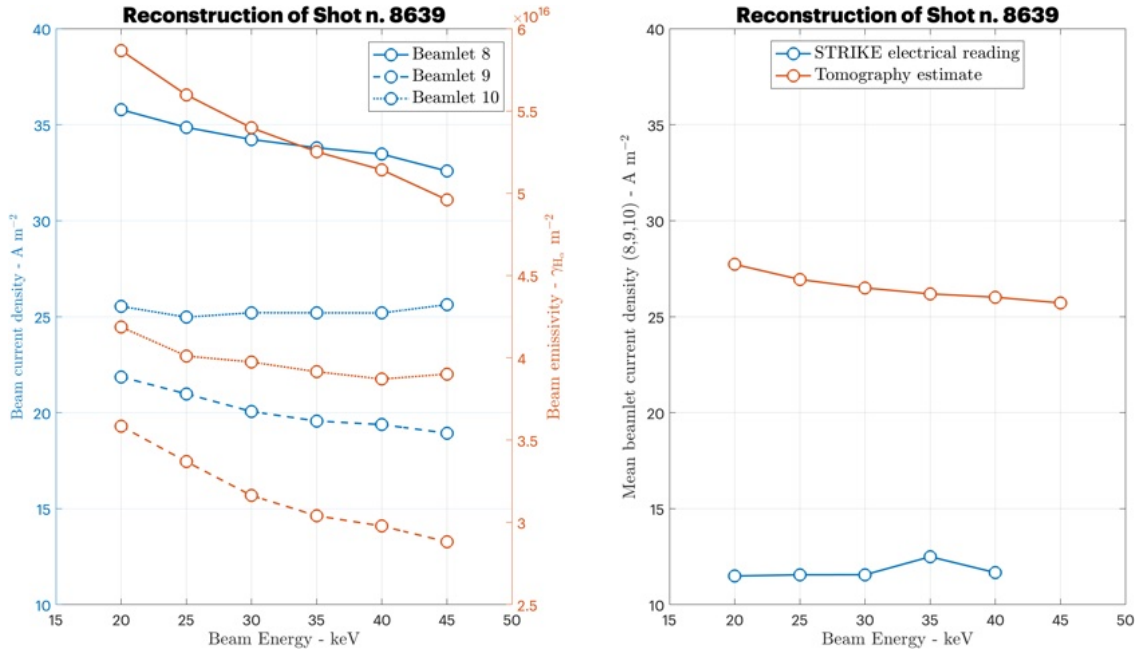
Figure 4.13: On the left, the estimate of emissivity (orange) and current density (blue) of beamlets 8, 9 and 10. On the right the averaged value of the current density of the 3 beamlets from tomography (orange) and from the STRIKE calorimeter (blue). On the right, the reconstructed emissivity decreases with increasing beam energy at constant extraction voltage, while the beam current density estimate remains constant. On the left, the reconstructed average of the beam current density if the 3 beamlets is matched by the STRIKE electrical readings.

Moreover, the density of secondary electrons is not expected to remain constant along the beam (as assumed in this model) and they might diffuse outwards, resulting in a lower beam current density.

One way to quantify the error associated to the reconstructed emissivity is computing the RMS between the experimental and the reconstructed integrals, denoted with I and $I_{\text{rec.}}$.

$$\text{RMS}_\epsilon = \text{rms}(I - I_{\text{rec.}})$$

This must be distinguished from the $\text{RMS}_{\text{rec.}}$ parameter, which quantifies the accuracy of the reconstruction of simulated data: RMS_ϵ is a measure of the error on the reconstructed emissivity from experimental data. However, this is still more an estimate of the quality of the reconstruction algorithm than of the real error associated to the reconstructed emissivity itself. In fact, it must be taken into account that many source of errors must be assessed, in particular:

- the error on the parameters of the LOSs, m and q: for a proper assessment of the uncertainties derived from the experimental setup of tomography, the exact location of the cameras must be verified with precise position ad orientation measurements with errors. Moreover, errors on objective magnification must be taken into account when evaluating the LOSs parameters;

- errors derived by the calibration of the camera: the filter transmission factor requires a quantification of its error, together with an assessment of losses inside the optic fibers of the experimental setup and an estimate on the error on the camera alignment with the parallel light. Better equipment should be used for improved stability of the experimental hardware (e.g. clamps, properly sized lenses). Thus, an estimate of the error on μ_c must be obtained with further work, also by using a simplified and more precise calibration apparatus (for example, by using a calibrated H_α lamp instead of filters);

- errors from the model, in particular errors on the cross-sections used. As discussed, cross sections are not always mapped in the range of energy required and polynomial interpolations are used. This introduces a level of assumption in the evaluation of the effective cross-section and the beam populations outside the energy range of the data. Moreover, not all cross-sections are available with associated errors, therefore a systematic experimental quantification of the cross-sections required at SPIDER's and MITICA's energy range is necessary to improve the reliability of this model;

- background gas measurement: the reliability of readings from pressure gauges inside the vessel can be an additional source of uncertainity.

In light of all this considerations, further work is necessary to refine the current estimate from tomography, first by assessing and reducing the errors introduced by data used (i.e. light integrals and errors on the camera calibration, cross-sections, pressure readings) and by refining the assumptions used in this work, for instance, employing more precise atomic models. For all the aforementioned reasons, an error on the tomographic beam current estimation is not provided.

5. Conclusions and future perspectives

In this work, improvements on the SPIDER beam tomographic diagnostic are developed, with the aim of obtaining more reliable and quantitative results, following two complementary paths. The first is the improvement of the inversion algorithm and its testing of its performance both on synthetic and experimental data. The second part involves the development of a spectroscopic model of the beam to interpret the beam light emission processes together with the absolute calibration of the cameras in order to obtain, for the first time, a two-dimensional beam current density estimate from the tomographic diagnostic across the beam section. SPIDER features multiple diagnostic for electrical and calorimetric measurements of the overall beam or of single beamlets' current density, as the STRIKE calorimeter or the Beam Current Monitor (BCM). However, these diagnostics are invasive and interfere with the beam by stopping it altogether (like STRIKE calorimeter) or they are limited to the measurements of few beamlets (BCM), both not compatible with the future ITER operation. The possibility of estimating the beam current from tomographic reconstruction would represent a substantial achievement for ITER NBI operation and MITICA.

SPIDER is the negative ion source prototype of the ITER Neutral Beam Injection, designed for the study and optimisation of the negative hydrogen ion beam before its implementation on MITICA, the full scale ITER NBI prototype. SPIDER hosts a large number of diagnostics, allowing to assess key beam parameters - as beam current density, beam uniformity and divergence - which must meet the strict requirements of ITER NBI. In particular, SPIDER aims at delivering stable current densities of 285 A m^{-2} using D$^-$ for one hour and 330 A m^{-2} in H$^-$ for 1000 s.

The focus of this thesis is on the visible camera tomography of SPIDER, consisting in a set of cameras pointing towards the negative ion beam from different directions. The light, produced by the interaction of the beam with the neutral background gas, is collected by the cameras and used as input for the tomographic reconstruction algorithm (SART), a representation of the two-dimensional light emissivity pattern of the beam across its section. The signal collected by the cameras is an integrated measure of the emissivity along each Line-Of-Sight, a two-dimensional region designed by each camera pixel.

The first part of this work consists in the implementation of two-dimensional Lines-

67

Of-Sight in the tomographic algorithm in order to achieve reliability and accuracy in the reconstruction. Prior to this work, in the reconstruction algorithm, all LOSs were assumed to be one-dimensional lines, introducing an underestimation error in the reconstruction. In the framework of the SART algorithm and the tomographic pixel method, this requires a new computation algorithm of the **a** matrix elements for the evaluation of the intersection area between the pixels and the 2D LOSs. These areas form the **a** matrix that is inverted by the SART algorithm. The development of this algorithm has been carried out with computational efficiency and flexibility in mind. The algorithm developed exploits the `Polyshape MATLAB` framework and offers the possibility of further refinement and adaptations to other scenarios: different sizes and shapes for the tomographic pixels are supported, irregular and regular, up to circular, allowing this algorithm to be applied also to other beam geometries or to tokamak plasmas. As the number of matrix elements can be very large, the tomographic pixel transform algorithm has been developed in order to employ computational power only on non-zero elements, allowing for a great reduction of time required for the evaluation of **a**. Tomographic inversion of experimental signal obtained using the new 2D LOS geometry has been compared with the result of the previous algorithm. The shape of the two emissivity profiles are in agreement, confirming the conformity of the new algorithm.

Since, up to now, SPIDER operated only with a limited amount of beamlets, the reconstruction accuracy of the new algorithm is tested using synthetic signals. The full beam is simulated assuming each beamlet emissivity to have a two-dimensional Gaussian profile and the camera signals are obtained by integrating the beam emissivity inside each LOS region using the analytical solution of the integral. To test the accuracy, the $\text{RMS}_{\text{rec.}}$ is defined, which quantifies the error on the reconstruction. In particular, I tested the effects on the reconstruction error of the spatial resolution (the number of tomographic pixels), the amount of background light, the amount of noise on the signals, the width of the beamlets and the homogeneity of the beam. Results show that the reconstruction error remains below or around the required 10% up to 5-beamlet-per-pixel resolution, increasing up to 65% at 1-beamlet-per-pixel resolution. This shows that the tomographic diagnostic presents a resolution boundary determined by the number of Fields-Of-View available, which could be only overcome by hardware modifications in order to accomodate more cameras. No dependence on the beamlet width or homogeneity is observed, proving the independence of the tomographic diagnostic performance on the beam features in the considered scenarios. The presence of a diffused background light is shown to be one of the largest sources of inaccuracy in the reconstruction, as the increase in background luminosity intensity causes a worsening of the inversion. This shows the necessity to limit as much as possible the presence of stray light inside the vessel - in the form of reflections and source light. The noise scan shows a weak increase in inaccuracy as the noise increases, proving the stability of the reconstruction algorithm. This will be of particular importance when tomography will be implemented on MITICA, as the ITER environment will suffer high neutron fluxes, which can cause larger electronic noise respect to the one observed in SPIDER.

The second part of this work consists in the evaluation of the beamlets current density from the 2D map of the inverted emissivity. This requires a spectroscopic model that links the H_α emissivity with the beam current and the absolute calibration of the cameras. The model is developed along the propagation axis of the beam in order to investigate the processes involved in the H_α light emission from neutral excited hydrogen. The population of four atomic species - negative hydrogen ions of the beam, neutral hydrogen, positive hydrogen ions and secondary electrons - is evaluated along the beam axis, starting from a pure negative ion beam exiting the Grounded Grid. The solution of the differential system, including the four species and the cross-sections of the main processes which they undergo along their path, shows an exponential decay of the negative ion population after the GG, while a slow rise in neutral hydrogen and positive ions and a quick increase in secondary electrons are observed. Once the populations of the beam are obtained, the beam emissivity is computed via the definition of an effective cross-section, which quantifies the probability of the beam species to become neutral excited hydrogen and emit H_α photons.

Knowing the relation between beam current and H_α light emission allows to use the reconstructed emissivity to estimate the beam current density. To this purpose, the absolute calibration of the cameras is necessary in order to convert the digital signal into number of photons collected. An experimental setup is prepared using a calibrated light source and a H_α interferential filter - as it represents the dominant wavelength present in the experiment - in order to obtain an equivalent calibrated H_α source. First, the filter transmission factor is measured using a spectrometer. Once the flux of H_α photons after the filter is obtained, one of SPIDER's cameras is placed after the filter and the calibration constant is obtained as the ratio between the counts of the image, the exposure time and the power flux coming from the H_α source.

Obtaining the calibration constant allows to convert the camera counts to real emissivity integral, where now the emissivity can be characterised as a radiant energy surface density. Knowing the experimental parameters of the reconstructed beam, such as background pressure and beam energy, allows to retrieve from the model the correct values of the effective cross-section and the beam current density can be estimated. Results shows that the beam current density, estimated using tomography, is of the same order of magnitude of the electrical measurements from the other available diagnostics. This is a promising results, showing the possibility of employing visible tomography as a current diagnostics on ITER NBI. The generality of this approach allows the application of current estimation from tomography not only to beam sources, but also to fusion plasmas inside the reaction chamber. Tomographic reconstructions produce a systematic over-estimation of the current density (159% and 227% in the assessed shots n. 9227 and n. 8639), most probably due to the presence of the light background which alters the effective emission integral of each beamlet. This, however, represents a promising achievement, considering the approximations introduced as a first attempt. Further refining and improvement of this result can be achieved in many ways. The characterisation of the behaviour of secondary electrons can be improved, as they could partecipate

69

in the background emission from the beam plasma, either via Particle-In-Cell modelling or by developing a full-fledged differential model accounting for all excited species and their diffusion in the cross-sectional coordinate along the beam, not only along its propagation direction. This would also represent a more precise approach compared to the use of the effective cross-section. The assessment of the mobility of secondary electrons would also offer insight on the beam current density distribution, since, in this model, all particles are assumed to proceed in the cylindrical volume of the beamlet. The signal collected by the visible cameras can be improved by removing part of the background light with interferential filters. It would be also possible to develop background-removing algorithms from the light integrals, also with the employment of artificial intelligence, to correct the beam current estimate. Moreover, a more precise calibration of the cameras can be carried out by reducing the parts involved in the process, i.e. by removing the filter and using a H_α calibrated lamp. This improvement on the reconstructed beam current density needs to be paired with an estimate of the error introduced. In this work, three areas of further investigation for the error computation are suggested: quantification of the error on the LOSs parameters derived by camera positioning, orientation and lens magnification; refinement of modelling, by retrieving better cross-sectional data with associated errors, obtaining more precise pressure readings on the SPIDER vacuum vessel and developing a more detailed model; camera calibration, by carefully assessing the errors introduced in the calibration experimental apparatus and repeating the calibration using fewer and specifically selected components (H_α calibrated source, better fixing tools for more reliable alignment).

The increased performance and reconstruction reliability of the tomographic diagnostic on SPIDER, via the introduction of two-dimensional Lines-Of-Sight, required to first test its performance on the simulated full beam of SPIDER, expected to operate in the upcoming years, followed by obtaining more precise emissivity reconstructions of the existing experimental data. The development of an atomic model of the beam beam light and composition and the calibration of the cameras has allowed to obtain, for the first time, an indirect, non-invasive estimate of the beam current. This opens the possibility to simultaneously estimate the beam uniformity and current density of the entire beam of MITICA, with elevated spatial and time (also real-time) resolution.

Bibliography

[1] S. Geng. "An Overview of the ITER Project". In: *Journal of Physics: Conference Series* 2386.1 (Dec. 2022), p. 012012. DOI: 10.1088/1742-6596/2386/1/012012. URL: https://doi.org/10.1088/1742-6596/2386/1/012012.

[2] C.L. Smith and S Cowley. "The path to fusion power". In: *Philosophical Transactions of the Royal Society A: Mathematical, Physical and Engineering Sciences* 368.1914 (Mar. 2010), pp. 1091–1108. DOI: 10.1098/rsta.2009.0216. URL: https://doi.org/10.1098/rsta.2009.0216.

[3] T. Kammash. "FUSION POWER AND ITS PROSPECTS". In: *Alternative Energy Sources*. Elsevier, 1981, pp. 607–685. DOI: 10.1016/b978-0-12-467102-7.50008-8. URL: https://doi.org/10.1016/b978-0-12-467102-7.50008-8.

[4] K.S. Krane. *Introductory nuclear physics*. John Wiley & Sons, 1991.

[5] Suliga M., S Shalgar, and Fuller G.M. "A closer look at the pp-chain reaction in the Sun: constraining the coupling of light mediators to protons". In: *Journal of Cosmology and Astroparticle Physics* 2021.07 (July 2021), p. 042. DOI: 10.1088/1475-7516/2021/07/042. URL: https://doi.org/10.1088/1475-7516/2021/07/042.

[6] S.M. Gonzalez de Vicente et al. "Overview on the management of radioactive waste from fusion facilities: ITER, demonstration machines and power plants". In: *Nuclear Fusion* 62.8 (May 2022), p. 085001. DOI: 10.1088/1741-4326/ac62f7. URL: https://doi.org/10.1088/1741-4326/ac62f7.

[7] L.W. Packer et al. "Activation of ITER materials in JET: nuclear characterisation experiments for the long-term irradiation station". In: *Nuclear Fusion* 58.9 (July 2018), p. 096013. DOI: 10.1088/1741-4326/aacca0. URL: https://doi.org/10.1088/1741-4326/aacca0.

[8] *Fusion For Energy - Bringing the power of the Sun to Earth*. URL: https://fusionforenergy.europa.eu.

[9] *The ITER Organization official website*. URL: https://www.iter.org.

[10] E.E. Yushmanov. "The power gain factor Q of an ideal magneto-electrostatic fusion reactor". In: *Nuclear Fusion* 20.1 (Jan. 1980), pp. 3–8. DOI: 10.1088/0029-5515/20/1/001. URL: https://doi.org/10.1088/0029-5515/20/1/001.

[11] R. Aymar, P. Barabaschi, and Y Shimomura. "The ITER design". In: *Plasma Physics and Controlled Fusion* 44.5 (Apr. 2002), pp. 519–565. DOI: 10.1088/0741-3335/44/5/304. URL: https://doi.org/10.1088/0741-3335/44/5/304.

[12] H. Zohm. "On the size of tokamak fusion power plants". In: *Philosophical Transactions of the Royal Society A: Mathematical, Physical and Engineering Sciences* 377.2141 (Feb. 2019), p. 20170437. DOI: 10.1098/rsta.2017.0437. URL: https://doi.org/10.1098/rsta.2017.0437.

[13] P.U. Lamalle et al. "Status of the ITER ICRF system design—'Externally Matched' approach". In: *AIP Conference Proceedings*. AIP, 2007. DOI: 10.1063/1.2800466. URL: https://doi.org/10.1063/1.2800466.

[14] M.A. Henderson et al. "EU developments of the ITER ECRH system". In: *Fusion Engineering and Design* 82.5-14 (Oct. 2007), pp. 454–462. DOI: 10.1016/j.fusengdes.2007.01.029. URL: https://doi.org/10.1016/j.fusengdes.2007.01.029.

[15] R.S. Hemsworth et al. "Overview of the design of the ITER heating neutral beam injectors". In: *New Journal of Physics* 19.2 (2017), p. 025005. DOI: 10.1088/1367-2630/19/2/025005. URL: https://dx.doi.org/10.1088/1367-2630/19/2/025005.

[16] R. Koch. "Fast Particle Heating". In: *Fusion Science and Technology* 57 (Feb. 2010). DOI: 10.13182/FST10-A9409.

[17] D. Marcuzzi et al. "Detail design of the beam source for the SPIDER experiment". In: *Fusion Engineering and Design* 85.10 (2010). Proceedings of the Ninth International Symposium on Fusion Nuclear Technology, pp. 1792–1797. ISSN: 0920-3796. DOI: https://doi.org/10.1016/j.fusengdes.2010.05.039. URL: https://www.sciencedirect.com/science/article/pii/S0920379610002516.

[18] V. Toigo et al. "The PRIMA Test Facility: SPIDER and MITICA test-beds for ITER neutral beam injectors". In: *New Journal of Physics* 19.8 (Aug. 2017), p. 085004. DOI: 10.1088/1367-2630/aa78e8. URL: https://doi.org/10.1088/1367-2630/aa78e8.

[19] P. Agostinetti et al. "Detailed design optimization of the MITICA negative ion accelerator in view of the ITER NBI". In: *Nuclear Fusion* 56.1 (Dec. 2015), p. 016015. DOI: 10.1088/0029-5515/56/1/016015. URL: https://doi.org/10.1088/0029-5515/56/1/016015.

[20] A. Maistrello et al. "Improvements in the SPIDER RF system". In: *Fusion Engineering and Design* 167 (June 2021), p. 112337. DOI: 10.1016/j.fusengdes.2021.112337. URL: https://doi.org/10.1016/j.fusengdes.2021.112337.

[21] P. Agostinetti et al. "Physics and engineering design of the accelerator and electron dump for SPIDER". In: *Nuclear Fusion* 51.6 (Apr. 2011), p. 063004. DOI: 10.1088/0029-5515/51/6/063004. URL: https://doi.org/10.1088/0029-5515/51/6/063004.

[22] P.W. van Amersfoort et al. "Formation of negative hydrogen ions on a cesiated W(110) surface: the influence of hydrogen implantation". In: *Journal of Applied Physics* 58.9 (Nov. 1985), pp. 3566–3572. DOI: 10.1063/1.335732. URL: https://doi.org/10.1063/1.335732.

[23] N. et al. Marconato. "An optimized and flexible configuration for the magnetic filter in the SPIDER experiment". In: *Fusion Engineering and Design* 166 (2021), p. 112281. DOI: 10.1016/j.fusengdes.2021.112281.

[24] J.P. Boeuf, B. Chaudhury, and L. Garrigues. "Physics of a magnetic filter for negative ion sources. I. Collisional transport across the filter in an ideal, 1D filter".

In: *Physics of Plasmas* 19.11 (Nov. 2012). DOI: 10.1063/1.4768676. URL: https://doi.org/10.1063/1.4768676.

[25] B. et al. Zaniol. "First measurements of optical emission spectroscopy on SPIDER negative ion source". In: *Review of Scientific Instruments* 91 (2020), p. 013103. DOI: 10.1063/1.5128900.

[26] M. Spolaore et al. "Design of a system of electrostatic probes for the RF negative ion source of the SPIDER experiment". In: *Journal of Physics D: Applied Physics* 43.12 (Mar. 2010), p. 124018. DOI: 10.1088/0022-3727/43/12/124018. URL: https://doi.org/10.1088/0022-3727/43/12/124018.

[27] M. Barbisan et al. "First results from beam emission spectroscopy in SPIDER negative ion source". In: *Plasma Physics and Controlled Fusion* 63.12 (Oct. 2021), p. 125009. DOI: 10.1088/1361-6587/ac2eb2. URL: https://doi.org/10.1088/1361-6587/ac2eb2.

[28] A. Rizzolo et al. "Final design of the diagnostic calorimeter for the negative ion source SPIDER". In: *Fusion Engineering and Design* 123 (2017). Proceedings of the 29th Symposium on Fusion Technology (SOFT-29) Prague, Czech Republic, September 5-9, 2016, pp. 768–772. ISSN: 0920-3796. DOI: https://doi.org/10.1016/j.fusengdes.2017.05.003. URL: https://www.sciencedirect.com/science/article/pii/S0920379617305380.

[29] M. Pavei et al. "SPIDER plasma grid masking for reducing gas conductance and pressure in the vacuum vessel". In: *Fusion Engineering and Design* 161 (Dec. 2020), p. 112036. DOI: 10.1016/j.fusengdes.2020.112036. URL: https://doi.org/10.1016/j.fusengdes.2020.112036.

[30] E. Sartori et al. "Influence of plasma grid-masking on the results of early SPIDER operation". In: *Fusion Engineering and Design* 194 (2023), p. 113730. ISSN: 0920-3796. DOI: https://doi.org/10.1016/j.fusengdes.2023.113730. URL: https://www.sciencedirect.com/science/article/pii/S0920379623003137.

[31] M. Ugoletti et al. "First results of SPIDER beam characterization through the visible tomography". In: *Fusion Engineering and Design* 169 (2021), p. 112667. ISSN: 0920-3796. DOI: https://doi.org/10.1016/j.fusengdes.2021.112667. URL: https://www.sciencedirect.com/science/article/pii/S0920379621004439.

[32] M. Ugoletti et al. "SPIDER Beam Homogeneity Characterization Through Visible Cameras". In: *IEEE Transactions on Plasma Science* 50.11 (2022), pp. 3913–3921. DOI: 10.1109/TPS.2022.3218129.

[33] E. Sartori et al. "First operations with caesium of the negative ion source SPIDER". In: *Nuclear Fusion* 62.8 (June 2022), p. 086022. DOI: 10.1088/1741-4326/ac715e. URL: https://doi.org/10.1088/1741-4326/ac715e.

[34] G. Serianni et al. "SPIDER, the Negative Ion Source Prototype for ITER: Overview of Operations and Cesium Injection". In: *IEEE Transactions on Plasma Science* 51.3 (Mar. 2023), pp. 927–935. DOI: 10.1109/tps.2022.3226239. URL: https://doi.org/10.1109/tps.2022.3226239.

[35]   S. Hughes. "CT Scanning in Archaeology". In: *Computed Tomography - Special Applications*. InTech, Nov. 2011. DOI: 10.5772/22741. URL: https://doi.org/10.5772/22741.

[36]   H Qiu. "The Principle and State-of-art Applications for CT Detector". In: *Journal of Physics: Conference Series* 2386.1 (2022), p. 012060. DOI: 10.1088/1742-6596/2386/1/012060. URL: https://dx.doi.org/10.1088/1742-6596/2386/1/012060.

[37]   J. Radon. "On the determination of functions from their integral values along certain manifolds". In: *IEEE Transactions on Medical Imaging* 5.4 (Dec. 1986), pp. 170–176. DOI: 10.1109/tmi.1986.4307775. URL: https://doi.org/10.1109/tmi.1986.4307775.

[38]   D. Bell and F. Maligs. *Filtered back projection*. June 2016. DOI: 10.53347/rid-45756. URL: https://doi.org/10.53347/rid-45756.

[39]   S. Tong, A.M. Alessio, and Paul E Kinahan. "Image reconstruction for PET/CT scanners: past achievements and future challenges". In: *Imaging in Medicine* 2.5 (Oct. 2010), pp. 529–545. DOI: 10.2217/iim.10.49. URL: https://doi.org/10.2217/iim.10.49.

[40]   N. Fonnesu et al. "Tomographic reconstruction of the beam emissivity profile in the negative ion source NIO1". In: *Nuclear Fusion* 56.12 (Sept. 2016), p. 126018. DOI: 10.1088/0029-5515/56/12/126018. URL: https://doi.org/10.1088/0029-5515/56/12/126018.

[41]   M. Ugoletti. "Beam physics via tomography diagnostics". PhD thesis. Università degli studi di Padova, 2022.

[42]   *Product page*. URL: https://www.baslerweb.com/en/products/cameras/area-scan-cameras/ace/aca1920-40gm.

[43]   *Product page*. URL: https://visionlink.it/product/blackfly-s-28-mp-color-gige-vision-sony-imx429/.

[44]   M. Agostini et al. "Tomographic diagnostic of the hydrogen beam from a negative ion source". In: *Phys. Rev. ST Accel. Beams* 14 (10 Aug. 2011), p. 102801. DOI: 10.1103/PhysRevSTAB.14.102801. URL: https://link.aps.org/doi/10.1103/PhysRevSTAB.14.102801.

[45]   *The Polyshape object definition in MATLAB*. URL: https://it.mathworks.com/help/matlab/ref/polyshape.html.

[46]   Y.L. Tong. *The Bivariate Normal Distribution*. New York, NY: Springer New York, 1990, pp. 6–22. ISBN: 978-1-4613-9655-0. DOI: 10.1007/978-1-4613-9655-0_2. URL: https://doi.org/10.1007/978-1-4613-9655-0_2.

[47]   D. Mussini. "Modelling of the propagation of a large negative hydrogen beam". MA thesis. Università degli studi di Padova, 2022.

[48]   *ALADDIN - Numerical database maintained by IAEA Nuclear Data Section A+M Data Unit*. URL: https://www-amdis.iaea.org/ALADDIN/.

[49]   C.F. Barnett et al. *Atomic data for fusion. Volume 1: Collisions of H, H2, He and Li atoms and ions with atoms and molecules*. July 1990, p. 13238.

[50]   J. Geddes, J. Hill, and H B Gilbody. "Formation of excited hydrogen atoms in electron detachment collisions by 3-25 keV H- ions". In: *Journal of Physics B: Atomic and Molecular Physics* 14.24 (1981), p. 4837. DOI: 10.1088/0022-3700/14/24/018. URL: https://dx.doi.org/10.1088/0022-3700/14/24/018.

[51]   Janev, R.K. and Langer, W.D. and Douglass E. Post, Kenneth Evans. *Elementary Processes in Hydrogen-Helium Plasmas*. 1987, 326. DOI: https://doi.org/10.1007/978-3-642-71935-6.

[52]   A. Shepherd et al. "Initial Results From the SPIDER Beamlet Current Diagnostic". In: *IEEE Transactions on Plasma Science* 50.11 (Nov. 2022), pp. 3906–3912. DOI: 10.1109/tps.2022.3176757. URL: https://doi.org/10.1109/tps.2022.3176757.

BIBLIOGRAPHY

Ringraziamenti